

**On Protein Recruitment Dynamics in Clathrin-Mediated Endocytosis  
and its Relation to Membrane Tension**

**Dissertation**

Presented in Partial Fulfillment of the Requirements for the Degree Doctor of Philosophy  
in the Graduate School of Ohio State University

By

Scott Huber, M.S., B.S.

Graduate Program in Physics

The Ohio State University

2019

Dissertation Committee:

Dr. Comert Kural, Advisor

Dr. Michael Poirier

Dr. Michael Lisa

Dr. Ralf Bundschuh

Copyrighted by

Scott Huber

2019

## Abstract

Clathrin-mediated endocytosis (CME) is a process in which plasma membrane area is transferred from the surface of the cell to the cell interior. Because cell volume increases and cell shape stays roughly constant in this process, the reduction in surface area must be accompanied by work done against the membrane's elasticity. This work is directly dependent on the tension of the cell membrane. From this, we hypothesize that CME dynamics will be totally or partially inhibited upon an increase in membrane tension. We prove this hypothesis *in vitro* and *in vivo*, utilizing newly developed methods for the quantification of CME dynamics. We then test the converse of this result—that impaired CME dynamics imply elevated membrane tension—to assess CME as an indirect reporter of spatial and temporal heterogeneities in membrane tension. Additionally, we assess the role of several CME-associated proteins in counteracting tension.

## **Vita**

May 2009.....Danville High School, Danville, IL  
May 2012.....B.S., Physics, Math Minor, University of  
Illinois, Urbana, IL

## **Publications**

Ferguson, J.P., Willy, N.M., Heidotting, S.P., Huber, S.D., Webber, M.J., and Kural, C. (2016). Deciphering dynamics of clathrin-mediated endocytosis in a living organism. *J. Cell Biol.* *214*, 347–358.

Willy, N.M., Ferguson, J.P., Huber, S.D., Heidotting, S.P., Aygün, E., Wurm, S.A., Johnston-Halperin, E., Poirier, M.G., and Kural, C. (2017). Membrane mechanics govern spatiotemporal heterogeneity of endocytic clathrin coat dynamics. *Mol. Biol. Cell* *28*, 3480–3488.

Ferguson, J.P.\*, Huber, S.D.\*, Willy, N.M., Aygün, E., Goker, S., Atabey, T., and Kural, C. (2017). Mechanoregulation of clathrin-mediated endocytosis. *J. Cell Sci.* *130*, 3631–3636.

## **Fields of Study**

Major Field: Physics

## Table of Contents

Abstract .....	iii
Vita.....	iv
Table of Contents .....	v
List of Figures .....	x
Chapter 1 Introduction .....	1
1.1 The Plasma Membrane .....	1
1.2 Clathrin and its adaptors .....	3
1.3 Fluorescence Microscopy .....	4
1.4 The Life of the Average Clathrin-Coated Pit.....	7
1.5 Measuring CME dynamics with growth rate histograms .....	8
1.6 Hierarchical Clustering and Lifetime-Normalized Trace Averaging .....	11
1.7 Thesis Overview .....	13
Chapter 2 Measuring Membrane Tension with Tethers .....	15

2.1 Abstract .....	15
2.2 Introduction .....	15
2.2.1 Tether extrusion .....	16
2.2.2 Magnetic Tweezers .....	18
2.2.3 Optical Tweezers .....	19
2.3 Results .....	21
2.3.1 Calibration .....	21
2.3.2 Measurement of reduction of tension during spreading .....	23
2.3.3 Measurement of tension as a function of adhered surface area .....	24
2.3.4 Measurement of the effect of cholesterol depletion .....	26
2.3.5 Measurement of local membrane tension in lamellapodia .....	27
2.4 Discussion .....	29
2.5 Methods .....	30
2.5.1 Optical Trap Specifications .....	30
2.5.2 Derivation of the relationship between tether force and membrane tension ...	31
2.5.3 Motivation for the presence of a restoring force of beads in optical tweezers	34
2.5.4 Flow Calibration of Optical Trap .....	36

2.5.5 Verification of the consistency of tension measurements.....	37
2.5.6 Cell Culture and Reagents .....	38
Chapter 3 Clathrin-mediated endocytosis subject to elevated membrane tension.....	39
3.1 Abstract .....	39
3.2 Introduction.....	40
3.3 Results.....	41
3.4 Discussion .....	52
3.5 Materials and Methods.....	54
3.5.1 Cell culture, reagents and fluorescence imaging .....	54
3.5.2 Squeezing, micropipette aspiration and osmotic shock .....	55
3.5.3 Single-particle tracking.....	57
Chapter 4 Using clathrin coat dynamics to assess membrane tension differences .....	59
4.1 Abstract .....	59
4.2 Introduction.....	60
4.3 Results.....	61
4.3.1 Clathrin coat dynamics in spreading and migrating cells .....	63
4.3.2 Spatiotemporal variations in clathrin dynamics of Drosophila embryos.....	71

4.4 Discussion .....	73
4.5 Materials and Methods.....	75
4.5.1 Cell culture and fluorescence microscopy .....	75
4.5.2 Fly strains and in vivo imaging.....	76
4.5.3 Two-dimensional tracking of clathrin-coated structures .....	77
4.5.4 Three-dimensional tracking of clathrin-coated structures .....	77
4.5.5 Growth rate distributions .....	78
4.5.6 Lifetime maps and dipole vectors .....	79
4.5.7 Tether force measurements .....	80
Chapter 5 <i>In Vitro</i> Characterization of CALM recruitment to clathrin coated structures	81
5.1 Abstract .....	81
5.2 Introduction.....	82
5.3 Results.....	84
5.3.1 Characterization of the numbers of proteins recruited to clathrin-coated pits.	84
5.3.2 Clathrin coated pit dynamics in CALM siRNA cells .....	85
5.3.3 Clathrin coated pit dynamics in CALM siRNA expressing cells subject to elevated membrane tension.....	90



5.3.4 Super-resolved localization of CALM in large, clathrin-coated structures using TIRF-SIM .....	93
5.4 Discussion .....	97
5.5 Materials and Methods.....	100
5.5.1 Cell culture.....	100
5.5.2 Fluorescence Imaging .....	101
5.5.3 Image Detection and Tracking.....	102
5.5.4 Single GFP Intensity Calibration .....	102
5.5.5 Object Dissolution Verification .....	102
5.5.6 Autocorrelation Analysis .....	103
Chapter 6 Conclusions and Future Work.....	104
Bibliography .....	110

## List of Figures

Figure 1.1: Types of Endocytosis .....	2
Figure 1.2: Steps of Endocytosis .....	2
Figure 1.3: Tether Extrusion .....	3
Figure 1.4: Clathrin .....	4
Figure 1.5: Example Flourescence Image.....	6
Figure 1.6: Clathrin-coated pit lifecycle .....	7
Figure 1.7: Lifetime vs Growth rate standard deviation .....	9
Figure 1.8: Visualization of the hierarchical clustering of CME traces .....	12
Figure 1.9: Hierarchical clustering with lifetime-normalized traces .....	13
Figure 2.1: Tether extrusion cartoon.....	17
Figure 2.2: Magnetic tweezers .....	19
Figure 2.3: Optical tweezers .....	20
Figure 2.4: Verification of QPD-based position detection .....	22
Figure 2.5: Comparison of average tether force in spread and unspread cells .....	24
Figure 2.6: Adhered area vs. tether force .....	25

Figure 2.7: Effect of Methyl- $\beta$ -Cyclodextrin .....	27
Figure 2.8: Tension at lamellapodial ridges.....	28
Figure 2.9: Simplified Tether Geometry.....	32
Figure 2.10: Ray tracing of a bead in an optical trap.....	35
Figure 2.11: Flow calibration of the optical tweezers.....	37
Figure 2.12: Repeated tether measurements from the same cell .....	38
Figure 3.1: Aspiration of the plasma membrane slows down clathrin coat dynamics. ....	42
Figure 3.2: Cell squeezing induces fast and reversible alterations in clathrin coat dynamics. ....	44
Figure 3.3: Hypotonic swelling inhibits clathrin coat dynamics temporarily.....	45
Figure 3.4: Actin dynamics mediate the inward movement of clathrin coats prior to disassembly. ....	48
Figure 3.5: Squeezing Growth Rates .....	49
Figure 3.6: Post-Squeeze dynamics .....	50
Figure 3.7: Squeezing and area change.....	51
Figure 4.1: Monitoring mechanoregulation of clathrin coat dynamics in real time. ....	62
Figure 4.2: Clathrin coat dynamics reflect changing membrane tension throughout cell spreading .....	64

Figure 4.3: Heterogeneous clathrin dynamics maps the tension gradient in protruding cells. ....	67
Figure 4.4: Heterogeneous CME during in vitro and in vivo cell migration. ....	70
Figure 4.5: Spatiotemporal variations in clathrin dynamics can be detected within tissues of Drosophila embryo. ....	73
Figure 5. 1: Calibrated Intensity Results.....	85
Figure 5.2: Effects of 60% CALM reduction .....	87
Figure 5. 3: Comparing Trace Clusters between Control and siRNA Conditions.....	89
Figure 5. 4: Internalization Rates under Osmotic Shock .....	91
Figure 5. 5: CALM Present at Scission under Hypotonic Shock in Control Cells .....	92
Figure 5. 6: CALM Present at Scission under Hypotonic Shock in CALM siRNA Cells	93
Figure 5.7: Autocorrelation Analysis of TIRF-SIM Images.....	95
Figure 5.8: Example of Plaque Internalization Event .....	99
Figure 5.9: Example of the Internalization of One of Two Nearby Pits .....	100
Figure 6. 1: Fluorescence image of the actin cytoskeleton .....	107

## **Chapter 1 Introduction**

### **1.1 The Plasma Membrane**

The plasma membrane plays a uniquely important role in cell biology: It defines the boundary of the cell. The plasma membrane is a bilayer of lipids arranged in a way such that it is impermeable to large or electrically charged molecules, but permeable to other molecules, like water. Therefore, anything large or electrically charged is partitioned either into the cytoplasm or the space outside the cell. For large, necessary proteins to cross the plasma membrane into the cell, the plasma membrane must be circumvented by a process called endocytosis (Conner and Schmid, 2003).

There are several distinct forms of endocytosis (Fig. 1.1). Each of these uses the same basic idea: The cargo must be surrounded by an envelope of plasma membrane, at which point the envelope can close around the cargo, forming a vesicle (Fig. 1.2). The vesicle is then effectively inside the cell without a hole ever being made in the membrane.

**Figure 1.1: Types of Endocytosis**

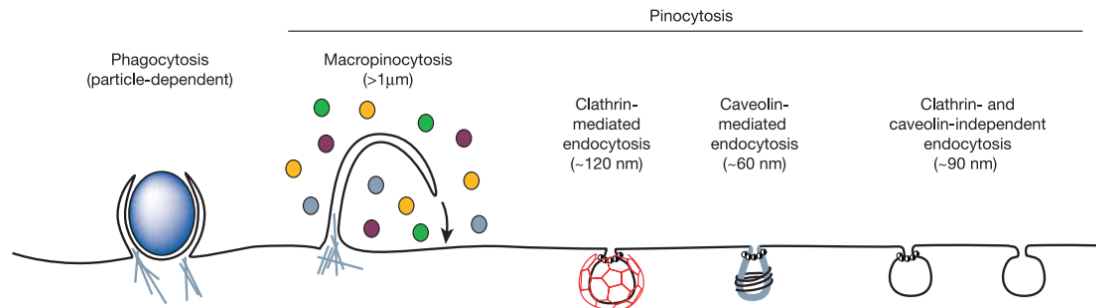


Figure from Conner et al., 2003

**Figure 1.2: Steps of Endocytosis**

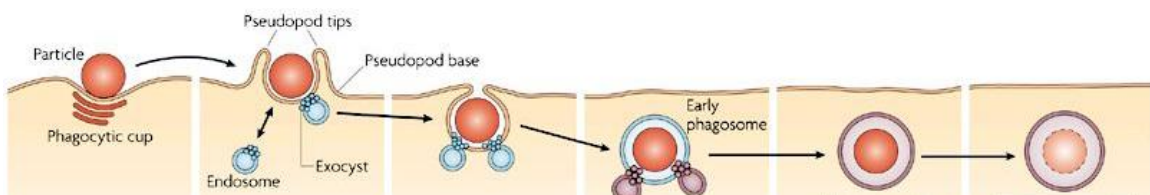


Figure from Stewart and Ezekowitz, 2008

Working against these processes is the fact that the plasma membrane is resistant to being curved or stretched. The membrane's resistance to stretch is related to a property called membrane tension (Diz-Muñoz et al., 2013). Traditionally, to measure this quantity the cell must be probed, quite literally, by applying an implement to the cell surface and extruding a tube of membrane called a “tether” (Fig. 1.3). This technique will be the subject of Chapter 2. Because of the physical limitations of this measurement

technique, scientists only have a rough experimental understanding of how cell tension varies over space and time.

**Figure 1.3: Tether Extrusion**

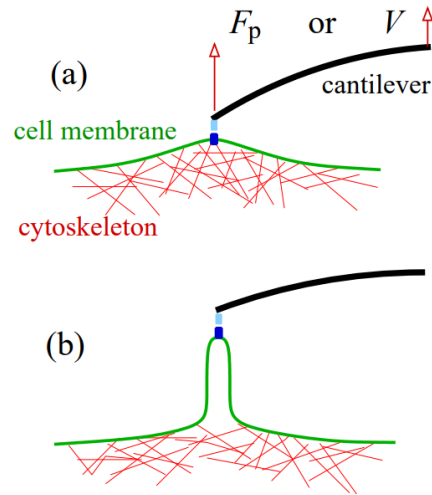


Figure from Nowak and Chou, 2010

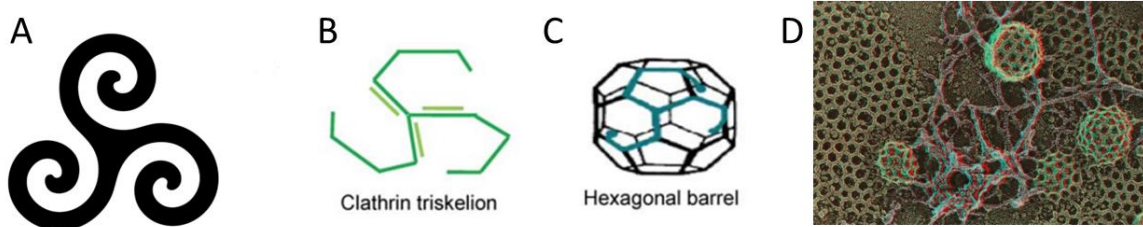
## 1.2 Clathrin and its adaptors

The method of endocytosis of interest in this work is clathrin-mediated endocytosis (CME). In this process, the energy needed to curve the membrane into a vesicle is partially supplied by the bonds of a molecule called clathrin.

Clathrin is a triskelion-shaped molecule (Fig. 1.4 A, B) that spontaneously self-assembles into round, closed cages if it is present at sufficient concentration and appropriate pH (Fig. 1.4 C) (Crowther et al., 1975). These cages are abundant in mammalian cells—so much so that they appear in almost any electron micrograph of the

cytoplasmic side of the cell membrane (Fig. 1.4 D). However, clathrin does not bind to the plasma membrane, so it cannot create vesicles without so-called “adaptor” proteins.

**Figure 1.4: Clathrin**



A) Historical triskelion motif B) Molecular shape of clathrin C) 3D Shape of a clathrin cage D) EM image of the cell membrane showing clathrin-coated structures

A from <https://www.tattoo.com/blog/upg/3377193/>. B, C from Gadkari and Srinivasan, 2012. D from Heuser, 2014

Aside from clathrin, AP2 and CALM are the most abundant proteins in clathrin-coated structures (Borner et al., 2012). These proteins can bind clathrin and the membrane simultaneously, thus linking clathrin to the membrane. As such, they are called adaptor proteins. AP2 will be of particular interest in this work because it, unlike clathrin, only localizes to CME-associated structures, which makes it a more specific marker of CME. CALM is a less-studied adaptor that additionally functions in curvature generation and sensation, which will be the subject of Chapter 5.

### 1.3 Fluorescence Microscopy

First used by Oscar Heimstädt in 1911 (Heimstädt, 1911), fluorescence microscopy is an imaging technique wherein fluorescent objects can be visualized by the collection of their

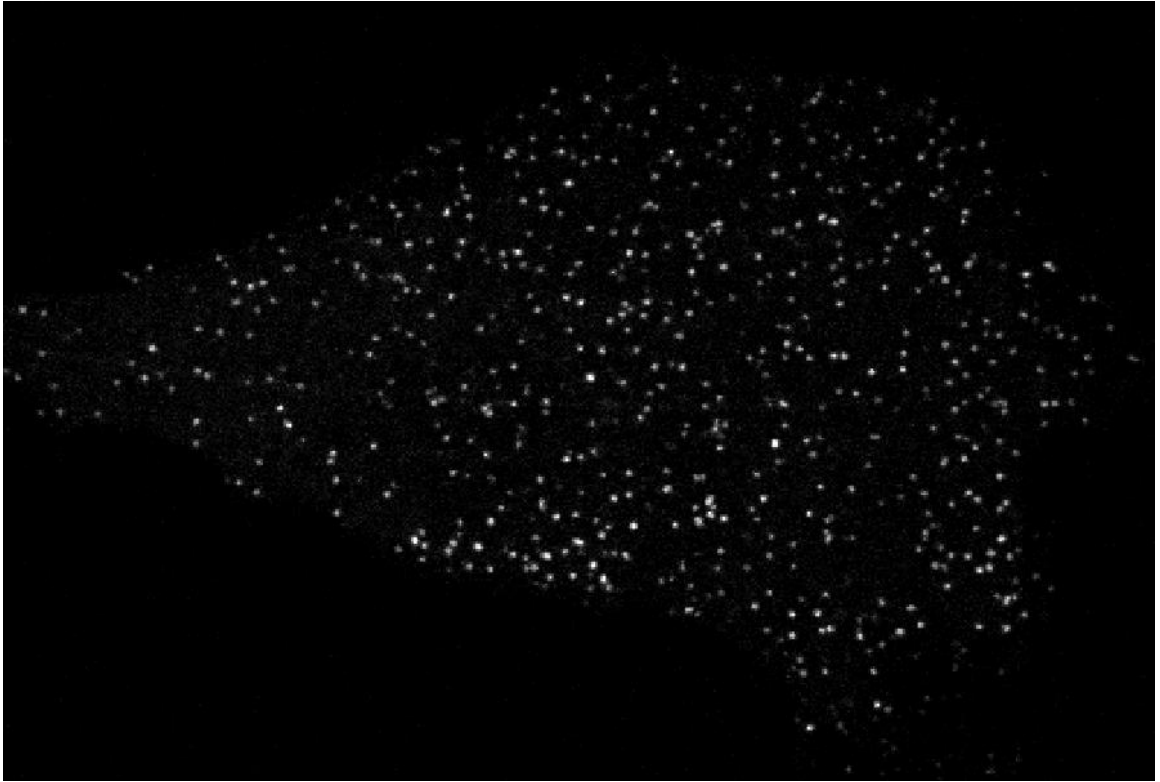


longer-wavelength emission light, when subject to a shorter-wavelength source.

Fluorescence microscopy is important in our work because it allows us to track the cellular location and relative numbers of different specific proteins in live cells.

Because proteins are very small, light microscopes cannot resolve them directly. To get around this problem, we transfect our cells with DNA that allows them to make a version of a CME protein (generally AP2) attached to a fluorescent tag. This way, when we shine a laser with a wavelength in the fluorescent tag's excitation spectrum at a cell, it will emit light in its emission spectrum only in the subcellular locations where our protein is located. For the specific case of AP2-eGFP, fluorescent imaging reveals discrete puncta on the cell membrane corresponding to CME-related structures (Fig. 1.5).

**Figure 1.5: Example Flourescence Image**



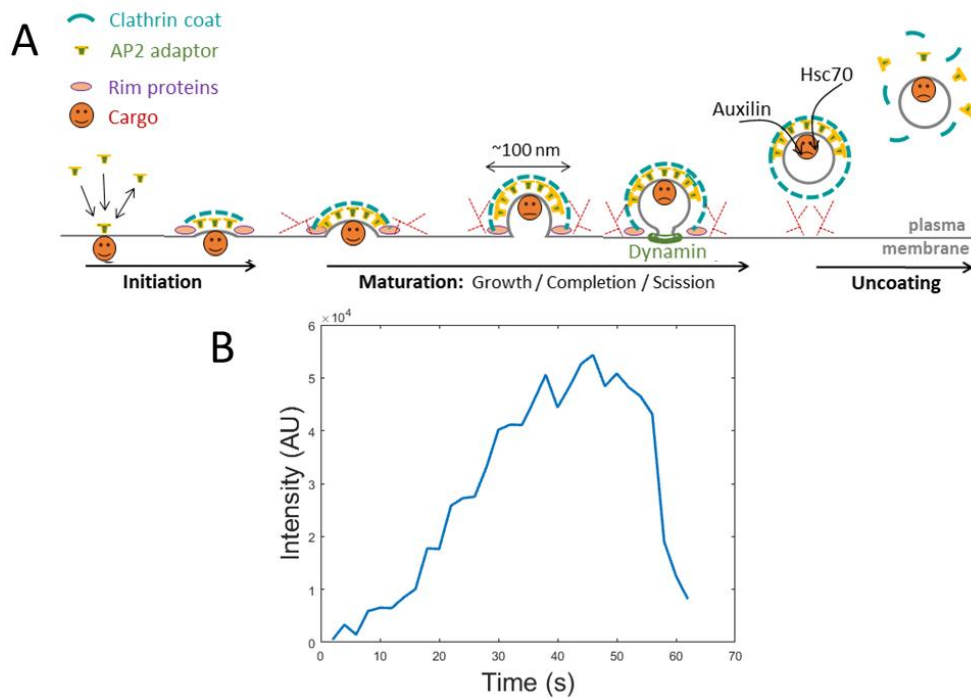
Example image illustrating clathrin puncta (marked with AP2-eGFP) marking clathrin-coated pits on the basal membrane

The single image in Figure 1.5 contains limited information. From it, we can only calculate the locations of the various clathrin-coated structures (CCSs) and their intensities. If we wish to study dynamic quantities such as the lifecycle of a CCS, we must track these puncta over time. To this end, we use previously developed software that uses advanced, optimized algorithms to track clathrin-coated structures on the plasma membrane (Aguet et al., 2013).

## 1.4 The Life of the Average Clathrin-Coated Pit

The round, clathrin-coated structure that forms on the membrane for the uptake of cargo is termed a “clathrin-coated pit”. Its lifecycle is illustrated in Figure 1.6 A. In words, the pit slowly and linearly accumulates clathrin and AP2 over roughly 40 seconds, then reaches a plateau in which dynamin and other proteins must be recruited to perform scission on the neck of the pit. A typical intensity profile corresponding to the clathrin content of a clathrin-coated pit over time is shown in Figure 1.6 B. Once scission is complete, the newly formed vesicle quickly diffuses away and un-coats, causing a steep decrease in intensity.

**Figure 1.6: Clathrin-coated pit lifecycle**



## **1.5 Measuring CME dynamics with growth rate histograms**

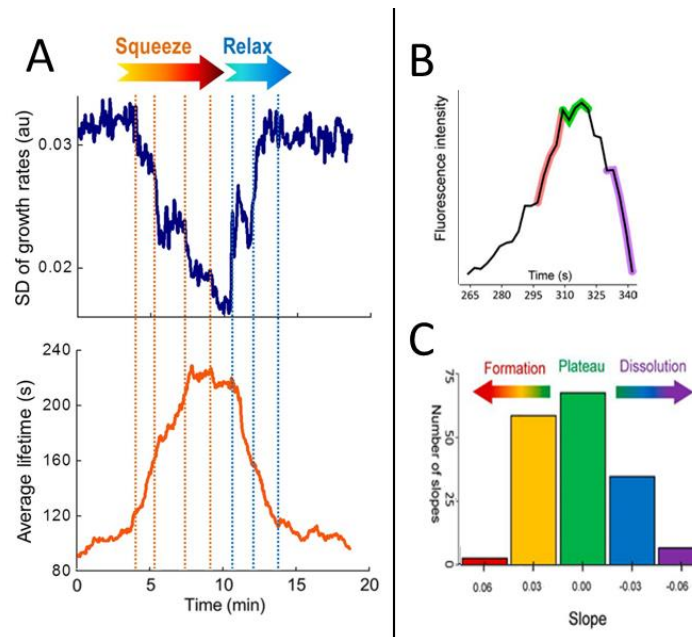
The most common method for quantifying CME dynamics is simply measuring the average time it takes pits to appear, gather clathrin, then leave the membrane. This number is referred to as the pit's lifetime. The lifetime of pits is a useful quantity because it changes in response to cell changes, such as an increase in membrane tension (Boulant et al., 2011). However, lifetime analysis has significant problems.

One simple problem is that the calculation of lifetimes requires entire CME events to be captured from start to finish. Because long movies result in a loss of fluorescence signal, typical fluorescence movies are limited to 5 to 10 minutes of length. Typical clathrin-coated pits have lifetimes of around one minute, while pits in adverse conditions, such as the experimental treatments discussed in chapters 3 and 4, can have lifetimes of several minutes. Combining these two facts, it is clear that many pits present in our movies will either start before the beginning of the movie or finish after the end of the movie. We cannot measure the lifetime of these pits, so any information we gather about them cannot be used in a lifetime analysis. Furthermore, longer lived pits are more likely to have this problem, so average lifetimes are biased toward shorter lifetimes—especially when calculating average lifetimes of pits around the ends of a movie.

Another problem is that, for each pit, this quantity does not give information about a specific point in time: A pit with lifetime 60 seconds does not tell us anything

about the state of the cell at any specific time during those 60 seconds; it only gives us averaged information about the entire 60 second period. As an example of where this could be a problem, consider the average lifetime plot in the bottom plot of Figure 1.7 A. An instantaneous change in cell state shows a delayed response in lifetime because pits that are nearly complete at the time of the change still have roughly normal lifetimes, and they must disappear before the average lifetime completely shifts to its final value.

**Figure 1.7: Lifetime vs Growth rate standard deviation**



A) Figure adapted from Ferguson et al., 2017. Vertical dotted lines represent nearly instantaneous squeezing and relaxing of the cell. Top plot: Growth rate-based quantification of pit dynamics. Bottom plot: Lifetime-based quantification of pit dynamics. Note the sharper response of the growth rate standard deviation upon changes, and the artificial reduction in lifetime near the ends of the movie. B) Figure adapted from Ferguson et al., 2016. Illustration of growth rate groups in the context of a single trace. Colors correspond to histogram bins in C. C) Figure adapted from Ferguson et al., 2016. Example growth rate distribution.

To get around these problems, we developed an alternative analysis based on “growth rates” of pits (Ferguson et al., 2016). In this analysis, instead of looking at lifetimes of entire pits, we calculate intensity slopes of each extant pit in each frame. As was referred to above, each pit undergoes a clathrin accumulation phase, a plateau phase, and a dissolution phase. When we bin all growth rates into a histogram, we see a roughly Gaussian distribution, with many events near 0 corresponding to the plateau phase, and fewer events in the extremely fast accumulation or dissolution tails (Fig. 1.7 B, C).

In this visualization, shorter lifetime events will contribute mostly to the tails of the distribution, while longer lifetime events will contribute more to the center. As such, the standard deviation of the growth rate distribution is a useful measure of the speed of clathrin dynamics. This measure has a significant advantage over average lifetime in that it only relies on a small time-window of data around each time-point (the time required for computing slope—generally 12 seconds). Therefore, it is not biased near the ends of the movie, and is much less delayed in detecting sudden dynamic changes when compared to lifetime analysis (Fig. 1.7 A). Additionally, it is less dependent on perfect tracking of events, which can be a major problem in low signal-to-noise experiments.

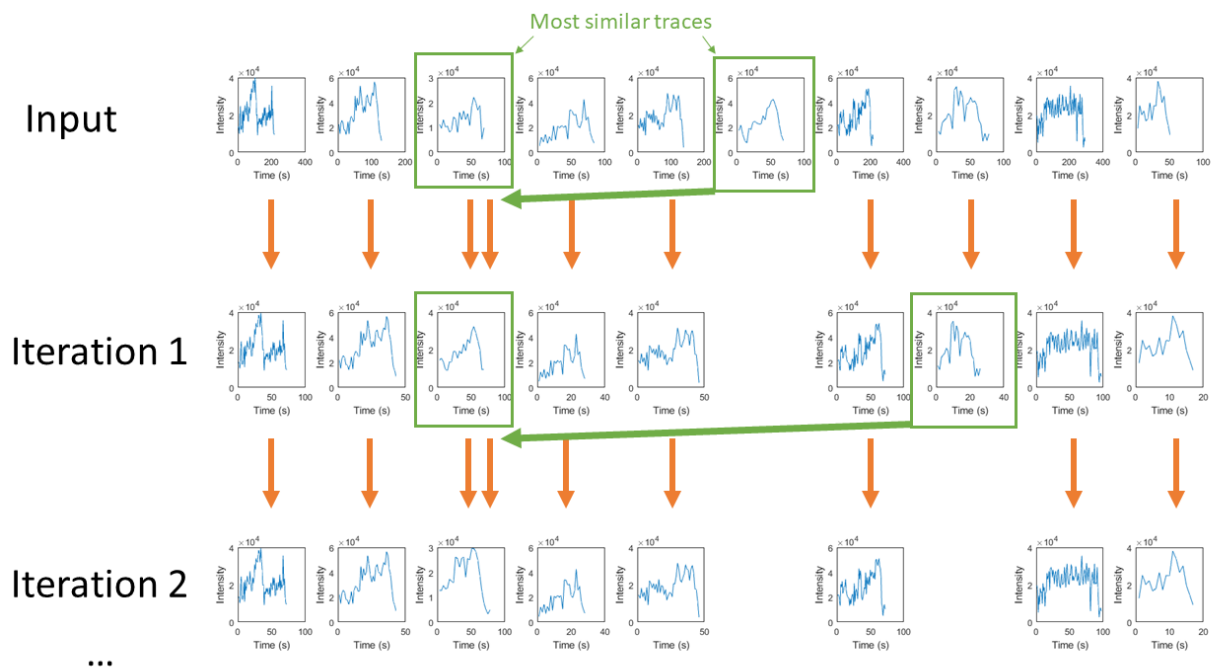
We introduced this analysis technique in a work in 2016 (Ferguson et al., 2016), and further applications of it will be introduced in Chapters 3 and 4.

## **1.6 Hierarchical Clustering and Lifetime-Normalized Trace Averaging**

Growth rate analysis is good at quantifying CME dynamics as a single number that varies in time, but the shape of clathrin traces can vary independently of this measure. The formation, plateau, and dissolution phases all depend on different parameters in different ways (Kirchhausen, 2009). To probe shape changes in clathrin traces, we used a hierarchical clustering algorithm.

Hierarchical clustering algorithms group objects into “clusters” based on the similarity between individual objects. Briefly, a collection of objects are input, and the most similar two objects (based on some metric) are grouped together and replaced by an averaged object (Fig. 1.8). This process is repeated until a desired number of clusters is reached. In our work, we input clathrin traces and use mean squared difference with a penalty term for traces of different length as the similarity metric. The clusters with the most traces are then the most representative trace shapes in our data (Fig. 1.8).

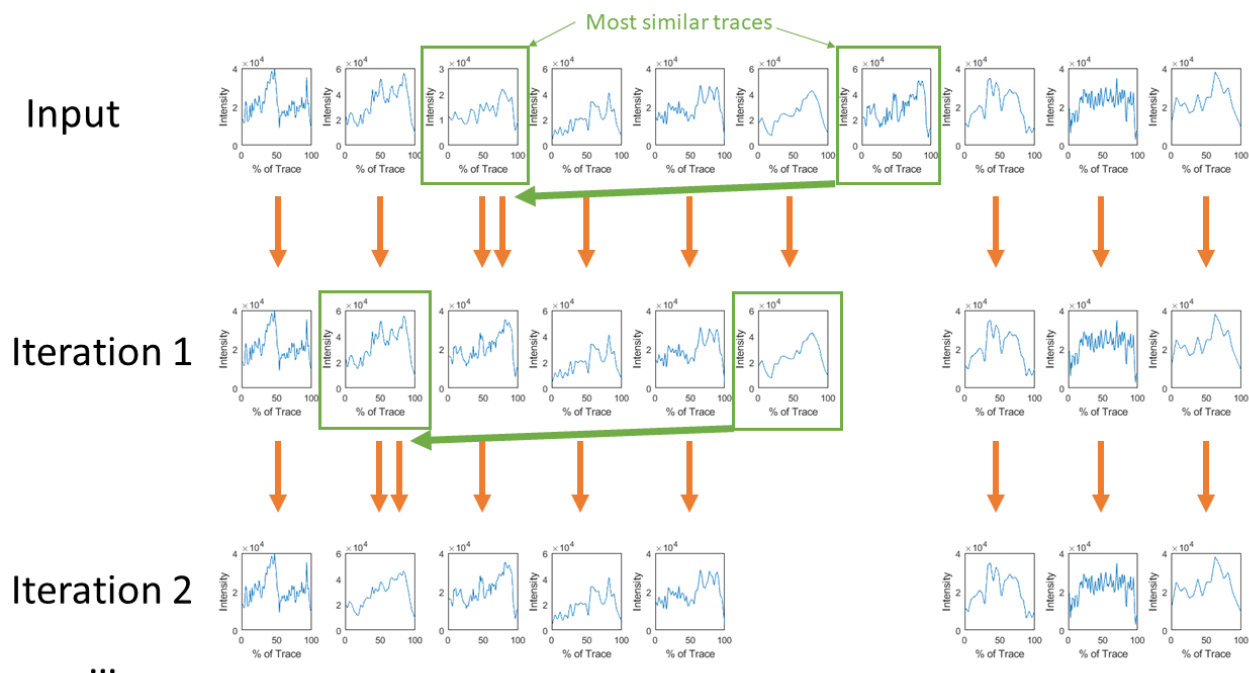
Figure 1.8: Visualization of the hierarchical clustering of CME traces



Because of the penalty term in our similarity metric, traces tend to be clustered into groups of roughly equal lifetime. To isolate the shape independently of lifetime, we apply hierarchical clustering to what we call “lifetime-normalized traces”, that is, traces interpolated to have a set number of time-points regardless of lifetime (Fig. 1.9).



**Figure 1.9: Hierarchical clustering with lifetime-normalized traces**



We first applied hierarchical clustering to CME traces in a work in 2016 (Ferguson et al., 2016), and it will be used again in Chapter 5.

## 1.7 Thesis Overview

This thesis will cover the extent of my study of clathrin mediated endocytosis and how membrane tension has far-reaching effects on the machinery thereof. Chapter 2 contains a description of current force spectroscopy techniques for measuring membrane tension, and results from our implementation of these techniques. Chapter 3 will describe how

artificially elevated membrane tension affects CME. Chapter 4 will explore the link between CME and membrane tension in a more physiological context. Chapter 5 will explore the relationship between the clathrin adaptor CALM and the cell's response to membrane tension. Lastly, chapter 6 will describe where future work could continue this study.

## **Chapter 2 Measuring Membrane Tension with Tethers**

### **2.1 Abstract**

Membrane tension is an important parameter in cellular mechano-signaling. It influences many cellular processes, such as vesicle trafficking and cell migration. The most common method for the measurement of membrane tension is the extrusion of membrane tethers using force spectroscopy techniques. We have assessed the dependence of membrane tension on several experimental treatments using both magnetic and optical tweezers. We found a decrease in tension during cellular spreading, but found no significant effect of cholesterol depletion on tension, and did not observe local differences in membrane tension in lamellapodial structures.

### **2.2 Introduction**

In addition to chemical signals, cells respond to physical signals from their environment. When stretched, the cell membrane responds like a spring by resisting increases in area with a force proportional to the amount its area has been increased (Phillips et al., 2013). In most cells, the stretch is additionally resisted by the underlying cytoskeleton. The sum

of these two resistances to stretch defines a value called membrane tension, typically measured in units of pN/ $\mu$ m, which is perhaps the simplest example of a mechanical property that responds to the extracellular environment.

Membrane tension affects several cellular processes. Mechanosensitive ion channels are more likely to be opened under high tension (Sukharev, 1999). Membrane tension has also been shown to affect cell migration and spreading by impeding the actin force that pushes the cell edge forward (Diz-Munoz et al., 2013; Raucher and Sheetz, 2000). Furthermore, tension affects both endocytosis and exocytosis rates in a feedback loop that allows the cell to add or subtract membrane from its surface, thus regulating its own tension (Apodaca, 2002; Boulant et al., 2011 ; Irajizad et al., 2017).

Previously, tether experiments have shown that membrane tension is elevated due to swelling caused by hypo-osmotic shock (Raucher and Sheetz, 2000). Tension has also been observed to change during cell spreading (Gauthier et al., 2009). Additionally, it has been shown that membrane tension can vary between different edges of migrating cells (Lieber et al., 2015). We seek to add to these results by testing the effect of other treatments on membrane tension

### **2.2.1 Tether extrusion**

The state-of-the-art method for the direct measurement of cellular membrane tension is the extrusion of membrane tethers. This method involves three steps (Fig. 2.1): 1) The

attachment of a small implement--usually a micron-sized bead—to the surface of the cell through brief contact. 2) Force application to the implement in the direction away from the cell membrane to extend a tube of membrane between the cell and the implement, commonly referred to as a “tether”. 3) Measurement of the force required to hold the tether in place.

**Figure 2.1: Tether extrusion cartoon**

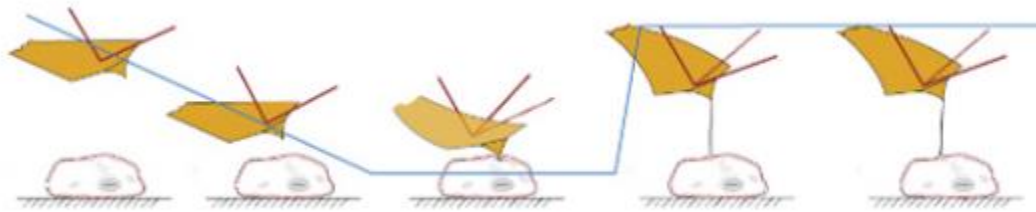


Figure from Diz-Munoz et al., 2010

The calculation of the membrane tension from this measurement relies on the theoretical conversion between tether force ( $F$ ) to membrane tension ( $T$ ):

$T = F^2 / (8\pi^2 K_b)$ , which can be derived from the Helfrich free energy of a lipid bilayer (Helfrich, 1973) (derived in methods). The constant ( $K_b$ ) in this equation is the bending modulus of the membrane, which can be calculated from tether pulling experiments where the radius of the tether can be measured. We use the value  $0.27 \text{ pN } \mu\text{m}$  taken from Hochmuth et al. (Hochmuth et al., 1996) measured on epithelial cells similar to the cells we used. Due to the monotonic relationship between tether force and area, and the

uncertainty of the exact value for  $K_b$  for individual cells, we generally compare tether forces instead of tensions, as is common practice (Diz-Munoz et al., 2013).

### **2.2.2 Magnetic Tweezers**

Perhaps the experimentally simplest way of extruding membrane tethers is the magnetic tweezer. First applied in 1950 by Crick and Hughes (Crick and Hughes, 1950), these simply use an applied magnetic field gradient to apply forces or torques to microscopic magnetic beads. Our setup, assembled by Alex Mooney, is illustrated in (Fig. 2.2).

Briefly, two neodymium iron cobalt magnets are suspended above a flow-cell such that a force is applied to the beads in the direction perpendicular to the coverslip. The magnets are controlled by a stepper motor, which can raise and lower the magnets, thus decreasing or increasing the applied force. The force exerted on 3  $\mu\text{m}$  superparametric dynabeads for each magnet height was previously measured using Brownian fluctuations of beads attached to DNA tethers (Simon, 2012). The surface of the flow cell was imaged with a CCD camera so that the effect of the magnet could be observed, and the position of the beads was monitored in real time using a custom-built LabView program.

**Figure 2.2: Magnetic tweezers**

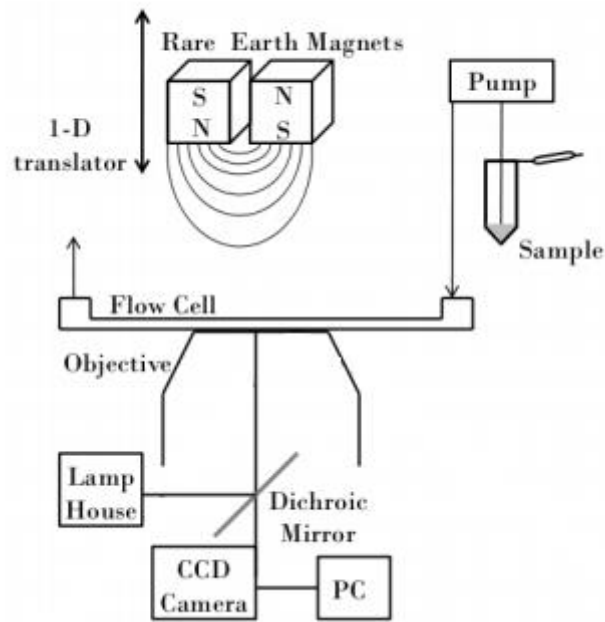
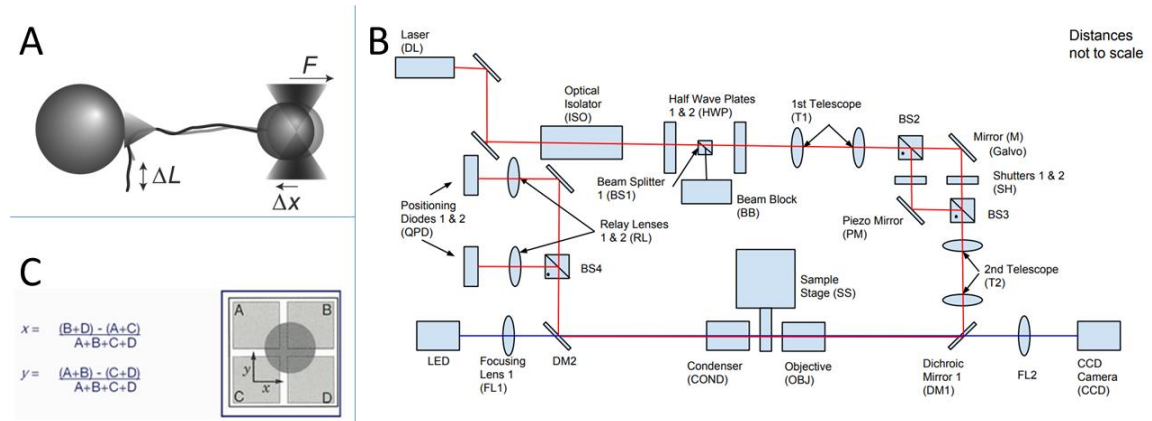


Figure from Simon, 2012

### 2.2.3 Optical Tweezers

Optical tweezers, first described by Arthur Ashkin in 1970 (Ashkin, 1970), use a Gaussian laser beam to trap small objects in place (Fig. 2.3 A). This Gaussian beam creates a restoring force (mathematically motivated in methods) that holds a trapped object at the narrowest part of the beam. Our implementation of this equipment, assembled by Ariel Wurm based on Bustamante et al. (Bustamante et al., 2014), is shown in Figure 2.3 B.

**Figure 2.3: Optical tweezers**



A) from Bustamante et al., 2014. B) provided by Ariel Robbins. C) from aptechnologies.co.uk

Essential for the measurement of force in an optical tweezer setup is the ability to localize the position of trapped particle with nanometer accuracy. For this purpose, we used a quadrant photodiode (QPD). This component is a photodiode split into four quadrants (Fig. 2.3 C), so that the light incident on each quadrant can be measured as a separate voltage signal. The QPD is placed at the back focal plane of a condenser in the laser path so that when the laser is undeflected, each quadrant measures the same voltage. A bead in the center of the trap scatters light equally in each direction, so it will not change the difference in the four voltages. However, if the bead is displaced from the center of the trap, it will increase the voltage of the quadrant in the direction it is displaced towards (Neuman and Block, 2004). In this way, the displacement of the bead can be measured from the four QPD voltages. The sample was simultaneously imaged with a CCD camera so that cells could be located.

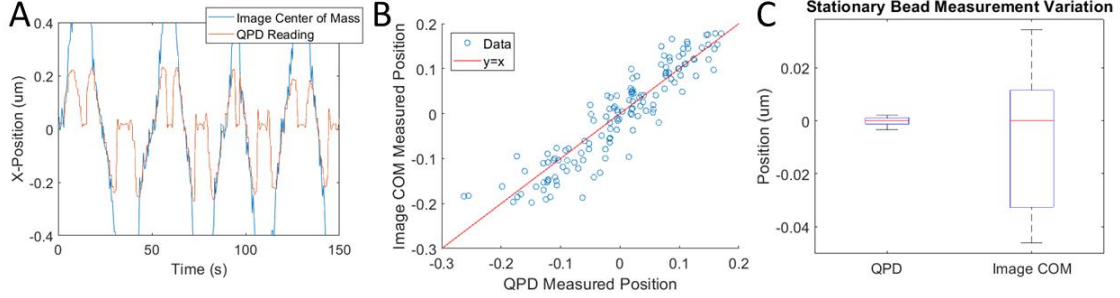


## **2.3 Results**

### **2.3.1 Calibration**

To assess the precision and range of the QPD measurement of bead position, we allowed beads to settle until they were firmly attached to the bottom of the flow-cell and used the piezo-controlled stage to scan a fixed bead through the area near the trap center. We then independently calculated the position during the scan with the QPD and with a center-of-intensity algorithm applied to the simultaneous microscope images. We found that the QPD measurement corresponded well with the image calculation as long as the bead was within  $.2\text{ }\mu\text{m}$  of the trap center (Fig. 2.4 A and B), which roughly corresponds to 20 pN of force with our working power level; because of this, we will consider 20 pN to be the maximum measurable force in future analyses. Furthermore, we found that the variation in position between subsequent measurements of the same position was much less using the QPD compared to that of the image analysis calculation (Fig. 2.4 C), demonstrating the more precise localization of the QPD.

**Figure 2.4: Verification of QPD-based position detection**



(A) Timecourse of the x-position of a bead during a position-scan across the center of the optical trap, as measured by the QPD and the center of the bead in the microscope images (B) Scatterplot of the data in A within .2 μm of the trap center as compared to the line  $y=x$  (C) Comparison of the variation in subsequent measurements of the same bead position by the QPD and the image analysis algorithm

To convert the distance from the center of the trap to a force, the trap stiffness must be measured. Since the stiffness depends on bead properties and our beads are not identical, we measured this stiffness for each bead we used. To do so, we acquired high-frequency QPD data for each new bead before attaching the bead to a cell. We then fit the x and y power spectrum of the resulting motion to the Lorentzian corresponding to the theoretical Brownian motion of a particle in a harmonic potential (Eq. 2.1) (Berg-Sorenson and Flyvbjerg, 2004).

$$P_k = \frac{D}{2\pi} * \frac{1}{f_c^2 + f_k^2} \quad (2.1)$$

Where  $D$  and  $f_c$  are the constants to be fit and  $f_k$  is the independent frequency variable. We then calculated both the spring constant of the trap and the conversion constant between QPD voltage and distance by comparing the fitted parameters to their theoretical values (Eqs. 2.2, 2.3) (Berg-Sorenson and Flyvbjerg, 2004).

$$\kappa = 2\pi\gamma_0 f_c \quad (2.2)$$

$$C = \sqrt{\frac{k_b T}{\gamma_0 D}} \quad (2.3)$$

Where  $\kappa$  is the spring constant of the trap,  $C$  is the conversion constant between the QPD reading in Volts and distance in meters,  $k_b$  is the Boltzmann constant, and  $\gamma_0$  is the drag coefficient of the beads in medium. We calculated  $\gamma_0$  from Stokes Law:

$$\gamma_0 = 6\pi\rho\nu R \quad (2.4)$$

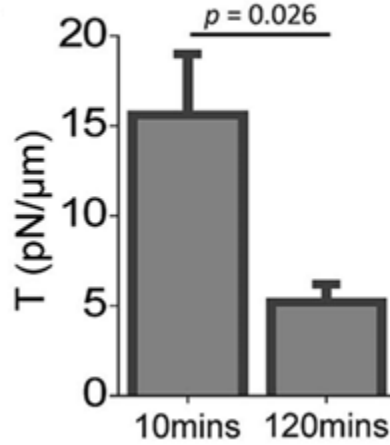
Where  $\rho$  is the density of the medium ( $1 \text{ g/cm}^3$ ),  $\nu$  is the Kinematic viscosity of the medium ( $10^{-3} \text{ Pa}\cdot\text{s}$ ) and  $R$  is the radius of our beads ( $.5 \text{ }\mu\text{m}$ ).

### 2.3.2 Measurement of reduction of tension during spreading

We first wanted to verify whether there is a change in membrane tension during cell spreading as was shown earlier (Gauthier et al., 2009). To do so, we used magnetic tweezers to extrude tethers from unspread BSC1 cells that had been plated for less than

40 minutes, and spread BSC1 cells that had been plated for 90 minutes or more. We found that the spread cells had significantly lower membrane tension on average (Fig. 2.5 B). In a separate experiment, we used optical tweezers to extrude tethers from unspread BSC1 cells that had been plated for 10 minutes, and compared their tension to spread BSC1 cells that had been plated for 120 minutes, which showed the same trend (Fig. 2.5 A)(Willy et al., 2017).

**Figure 2.5: Comparison of average tether force in spread and unspread cells**



From Willy et al., 2017. Optical tweezer quantification of the difference in tension between cells plated for 10 minutes and cells plated for 120 minutes.

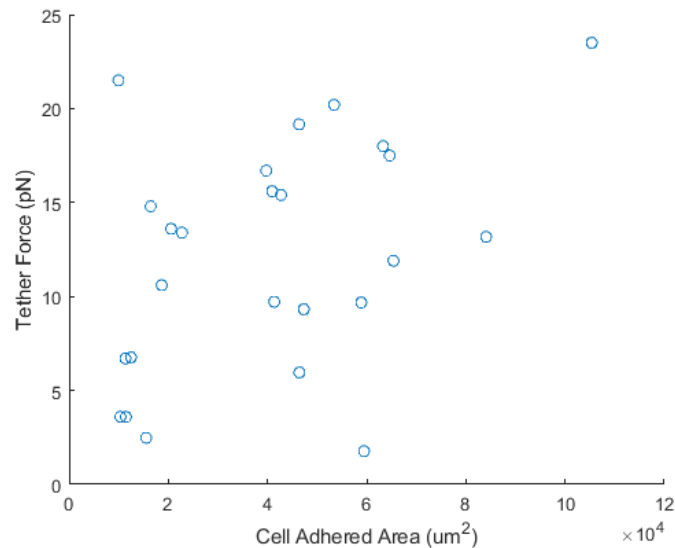
### **2.3.3 Measurement of tension as a function of adhered surface area**

Given that spread cells have lower tension than unspread cells, we hypothesized the amount of cell area adhered to the glass in spreading BSC1 cells would correlate with

membrane tension. If true, this would allow us to use regression to estimate membrane tension in spreading cells using only adhered area, which can be measured with essentially any microscopy technique.

To test this, we used optical tweezers to measure tether forces from 25 cells in various stages of spreading (Fig. 2.6). In the end, tether force did not significantly correlate with adhered area (Pearson  $R=0.41$ ), contradicting our hypothesis. Due to heterogeneity in cell size, cells with larger adhered areas are not necessarily further in the process of spreading, which may be the cause of this negative result. It also may be the case that the tension reduction we measured during spreading may only happen after spreading is finished, so that cells that are still undergoing spreading may still have elevated membrane tension.

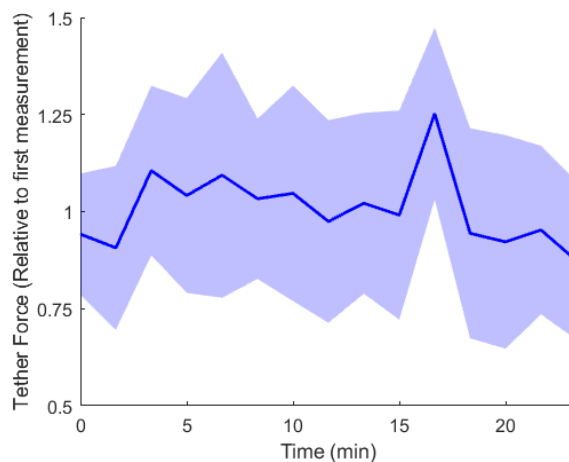
**Figure 2.6: Adhered area vs. tether force**



### **2.3.4 Measurement of the effect of cholesterol depletion**

Methyl- $\beta$ -Cyclodextrin ( $M\beta CD$ ) is an oligomer that is commonly used to remove cholesterol from the cell membrane (Zidovetzki and Levitan, 2007). It has been previously shown that removal of cholesterol with  $M\beta CD$  inhibits clathrin-mediated endocytosis within approximately 15 minutes (Rodal et al., 1999). As such, we hypothesized that this effect was caused by an increase in membrane tension. To test this, we extruded tethers from BSC1 cells shortly after addition of 4 mM  $M\beta CD$ , and monitored tether force thereafter. We did not see a consistent rise in tether force in the 20 minutes immediately after addition of  $M\beta CD$  (Fig. 2.7). This perhaps implies that the inhibition of CME by  $M\beta CD$  is due to some factor other than an increase in membrane tension. It has been shown that cholesterol depletion increases membrane “stiffness” (Byfield et al., 2004), a parameter independent from membrane tension that also opposes the outer membrane area loss involved in endocytosis; perhaps that is the mechanism involved in  $M\beta CD$ ’s effect on CME.

**Figure 2.7: Effect of Methyl- $\beta$ -Cyclodextrin**



Solid line corresponds to mean force of all tether measurements in each time window ( $N_{cells}=6$ ). Shaded region corresponds to the standard deviation. All data was normalized by the first measurement of each cell to assess the change in value.

### 2.3.5 Measurement of local membrane tension in lamellapodia

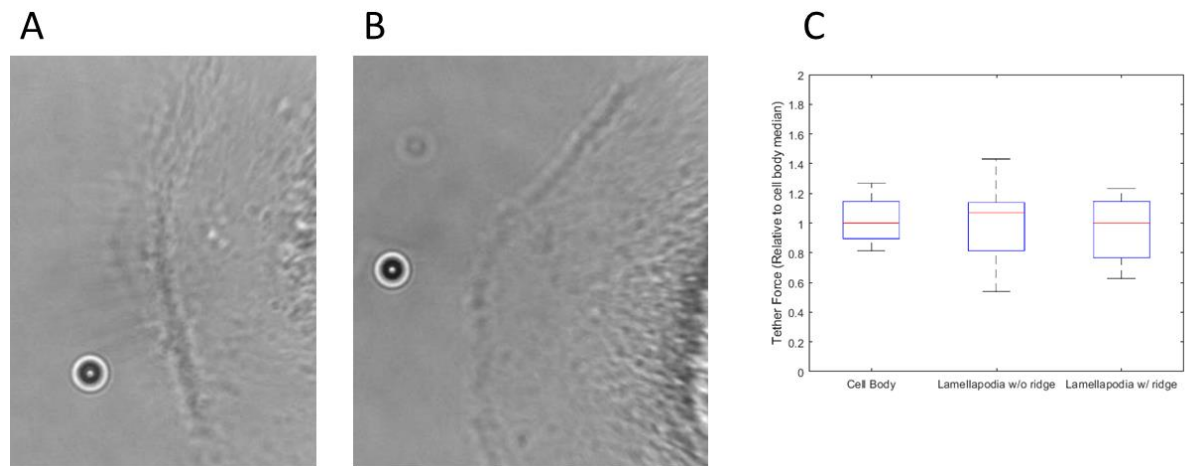
Because of a previous result showing tension variation between the front and back sides of migrating cells (Lieber et al., 2015), and our observation that endocytosis events are rare around the “ridges” that sometimes appear at the edge of the lamellapodia of migrating cells (Fig. 2.8 A), we hypothesized that membrane tension around lamellapodial ridges was higher than that of lamellapodia without ridges (Fig. 2.8 B).

Therefore, we took tether measurements from sites near lamellapodial ridges in astrocytes and compared the results to that of measurements taken from sites on lamellapodia without ridges and sites away from lamellapodia on the cell body (Fig. 2.8 C). We found

no consistent difference between the three groups, implying that either the endocytic difference we observed is not due to a difference in membrane tension, or that the precision of our measurements was not sufficient to detect the spatial variation in tension.

The nature of tether measurements dictate that measurements can only be made of the dorsal surface of the cell, while fluorescence microscopy is more commonly done on the ventral surface. It is possible that the membrane tension is elevated on the ventral surface of lamellapodia with ridges, resulting in slowed CME, while the tension remains normal on the dorsal surface.

**Figure 2.8: Tension at lamellapodial ridges**



A) Example tether pulled from a lamellapodium with a ridge B) Example tether pulled from a lamellapodium without a ridge C) Comparison of relative tether force of tether pulled from the cell body, lamellapodium without ridges, and lamellapodium with ridges



## 2.4 Discussion

We have confirmed the finding that membrane tension decreases during cell spreading. This finding may seem counterintuitive: One may presume that the rounded up state of the cell pre-spreading would have the lowest tension. It has previously been hypothesized that this effect happens because spreading is accompanied by an addition of membrane area from exocytic vesicles (Gauthier et al., 2009). It has also been hypothesized that elevated membrane tension acts as a signal to coordinate spreading in different regions of the cell (Gauthier et al., 2011). We have seen indirect evidence for this phenomenon in independent experiments: In cells with fluorescently tagged endocytosis proteins, we observed distinctly slowed endocytosis dynamics in spreading cells when compared to already-spread cells, corroborating the idea of that membrane tension decreases during spreading (Willy et al., 2017).

Aside from the above result that tension decreases during spreading, our other experimental treatments caused no significant change to average membrane tension. This may be due to a number of factors. First, cell tension is a notoriously variable parameter between individual cells (Gauthier et al., 2009). Second, as was shown by Lieber et al. and separately by Shi et al. (Lieber et al., 2015; Shi et al., 2018), membrane tension can vary even between different parts of a single cell, which is problematic because tether measurements are limited to measuring the tension at single points in the membrane. Neither of the above problems are necessarily impossible to overcome with a large-

enough sample size. Unfortunately, the third problem with our setup is that it has a very limited throughput: The manual manipulation of tethers combined with optics calibration make experimental setup time-consuming, while the environment of an optics table is not conducive to cellular homeostasis over long experimental acquisitions.

Combined, these problems with tether measurements vastly limit the scope of tether-based experiments. Future advancement of membrane tension knowledge will likely require alternative methods. Using clathrin dynamics as an indirect reporter of membrane tension, we have been able to observe relative tension differences over time in spreading cells, and over space in migrating cells (Willy et al., 2017). Other promising approaches involve the FRET-based measurement of mechanosensitive channels (Wang et al., 2014), and recently developed fluorescent tension probes (Colom et al., 2018)

## **2.5 Methods**

### **2.5.1 Optical Trap Specifications**

The optical trap design was based on that of Bustamante et al. (Bustamante et al., 2014) with only one of the two traps used. Position detection was done by use of Quadrant Photodiode. LASER power of the trap was set to 300 mW.

The beads used were 1 micron diameter polystyrene beads (Spherotech) coated with fibronectin (Sigma-Aldrich) as in Lee et al. (Lee et al., 2008) with centrifugation used in place of magnetic particle separation.

To extrude a tether, we trapped a bead with the optical tweezers, put it in contact with a cell for approximately 10 seconds, then slowly extended the tether by moving the stage parallel to the glass in .2 micron steps. Once the tether reached a length of approximately 10 microns, we held the bead in place for 2 minutes to let the tether force fall to its steady-state value. After this, the bead was moved quickly towards the cell until further movement did not change the force on the bead to find the zero-force bead position.

### 2.5.2 Derivation of the relationship between tether force and membrane tension

Here we will derive the equation  $\tau = F^2/(8\pi^2 K_b)$  assuming Hooke-like resistance to stretch (Eq. 2.5) and resistance to bending given by the Helfrich-Canham-Evens free energy (Eq. 2.6). In these equations,  $K_a$  and  $K_b$  are constants associated with the stretching and bending of the membrane, respectively,  $\Delta a$  is the area increase compared to an unstretched reference area  $a_0$ , and  $\kappa_1$  and  $\kappa_2$  are the principle curvatures at a given point. This derivation will follow that of Phillips et al. in Physical Biology of the Cell (Phillips et al., 2013).

$$E_{\text{stretch}} = \frac{K_a}{2} \int \left( \frac{\Delta a}{a_0} \right)^2 da \quad (2.5)$$

$$E_{\text{bend}} = \frac{K_b}{2} \int (\kappa_1(x, y) + \kappa_2(x, y))^2 da \quad (2.6)$$

First, we need to define the geometry of our tether pulling problem. We will consider a spherical cell body of radius  $R$  with a cylindrical tether of radius  $r$  and length  $L$  and a hemispherical cap on the end of the tether (Fig. 2.9). We will assume that  $r \ll R$  as is experimentally obvious. At the end of the derivation, we will assess whether the results from our simple geometry will extend to more realistic cells.

**Figure 2.9: Simplified Tether Geometry**

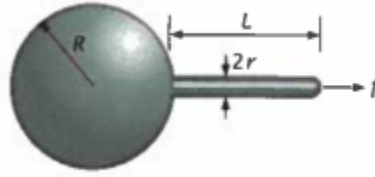


Figure from Phillips, 2013

We intend to calculate the free energy of the membrane configuration in Figure 2.9 in terms of  $R$ ,  $r$ , and  $L$ ; and then minimize this value in terms of the free parameters of the cell. Using (Eq. 2.5), we can calculate the free energy due to stretch of our geometry:

$$E_{\text{stretch}} \approx \frac{\frac{K_a}{2} (4\pi R^2 + 2\pi r L + 2\pi r^2 - a_0)^2}{a_0^2} \approx \frac{\frac{K_a}{2} (4\pi R^2 + 2\pi r L - a_0)^2}{a_0^2} \quad (2.7)$$

Using (Eq. 2.6), we can calculate the free energy due to bend of our geometry:

$$E_{\text{bend}} \approx 8\pi K_b + \frac{\pi K_b L}{r} + 4\pi K_b \quad (2.8)$$

Additionally, we need to include the energy from a change in volume working against a difference in pressure between the inside and outside of the cell:

$$E_{pressure} \approx \Delta p \left( \frac{4}{3} \pi R^3 + \pi r^2 L + \frac{2}{3} \pi r^3 \right) \approx \Delta p \left( \frac{4}{3} \pi R^3 + \pi r^2 L \right) \quad (2.9)$$

Lastly, we need to add the energy supplied by the force pulling the tether:

$$E_{work} = FL \quad (2.10)$$

Where F is the force applied to extrude the tether, which is assumed to be constant over the entire pulling process because of experimental evidence.

With the free energy now expressed in terms of R, r, L, and constants, we can now minimize with respect to our free parameters and get three equilibrium conditions of the system.

$$\frac{\partial E_{tot}}{\partial R} \approx \frac{K_a(a - a_0)}{a_0} 8\pi R + 4\pi \Delta p R^2 = 0 \quad (2.11)$$

$$\frac{\partial E_{tot}}{\partial r} \approx -\frac{\pi K_b L}{r^2} + 2\pi L \frac{K_a(a - a_0)}{a_0} + 2\pi \Delta p r L = 0 \quad (2.12)$$

$$\frac{\partial E_{tot}}{\partial L} \approx \frac{\pi K_b}{r} + 2\pi r \frac{K_a(a - a_0)}{a_0} + \pi \Delta p r^2 - F = 0 \quad (2.13)$$

The term  $K_a(a - a_0)/a_0$  is the tension on the membrane,  $\tau$ . Using this, and solving the R equation gives an expression for  $\Delta p$ , which we can then plug into the other equations:

$$\Delta p = -\frac{2\tau}{R} \quad (2.14)$$

$$-\frac{\pi K_b L}{r^2} + 2\pi L \tau - \frac{4\pi L r \tau}{R} \approx -\frac{\pi K_b L}{r^2} + 2\pi L \tau \approx 0 \quad (2.15)$$

$$r \approx \sqrt{\frac{K_b}{2\tau}} \quad (2.16)$$

Which could give us the tension if we could measure the radius of the tether as in Bo and Waugh, 1989. Since we want  $\tau$  as a function of  $F$ , we will plug in these expressions for  $r$  and  $\Delta p$  into our  $\partial E/\partial L$  equation:

$$\frac{\pi K_b}{r} + 2\pi r\tau - \frac{2\pi r^2\tau}{R} - F \approx \frac{\pi K_b}{r} + 2\pi r\tau - F \approx 2\sqrt{2}\pi\sqrt{K_b\tau} - F \approx 0 \quad (2.17)$$

$$F = 2\pi\sqrt{2K_b\tau} \quad (2.18)$$

Which we can then use to calculate  $\tau$  from our measurement of  $F$ , given a literature value of  $K_b$ . Additionally, more difficult experiments can be done to measure  $F$  and  $r$  simultaneously to calculate a value for  $K_b$ . Note that our value of  $R$  does not factor into any of our final equations given that  $R \gg r$ ; this suggests that our chosen spherical cell geometry did not noticeably affect our result.

### 2.5.3 Motivation for the presence of a restoring force of beads in optical tweezers

Here we will present an argument for the presence of a lateral restoring force on beads placed in a Gaussian bead using ray tracing. Ray tracing is only valid if the diameter of the bead is much greater than the wavelength of the light, which is not strictly true for our 1  $\mu\text{m}$  beads subjected to a near-infrared laser, but similar results can be obtained using

the opposite assumption that the diameter of the bead is much less than the wavelength of the light by treating the bead as an induced dipole.

Figure 2.10: Ray tracing of a bead in an optical trap

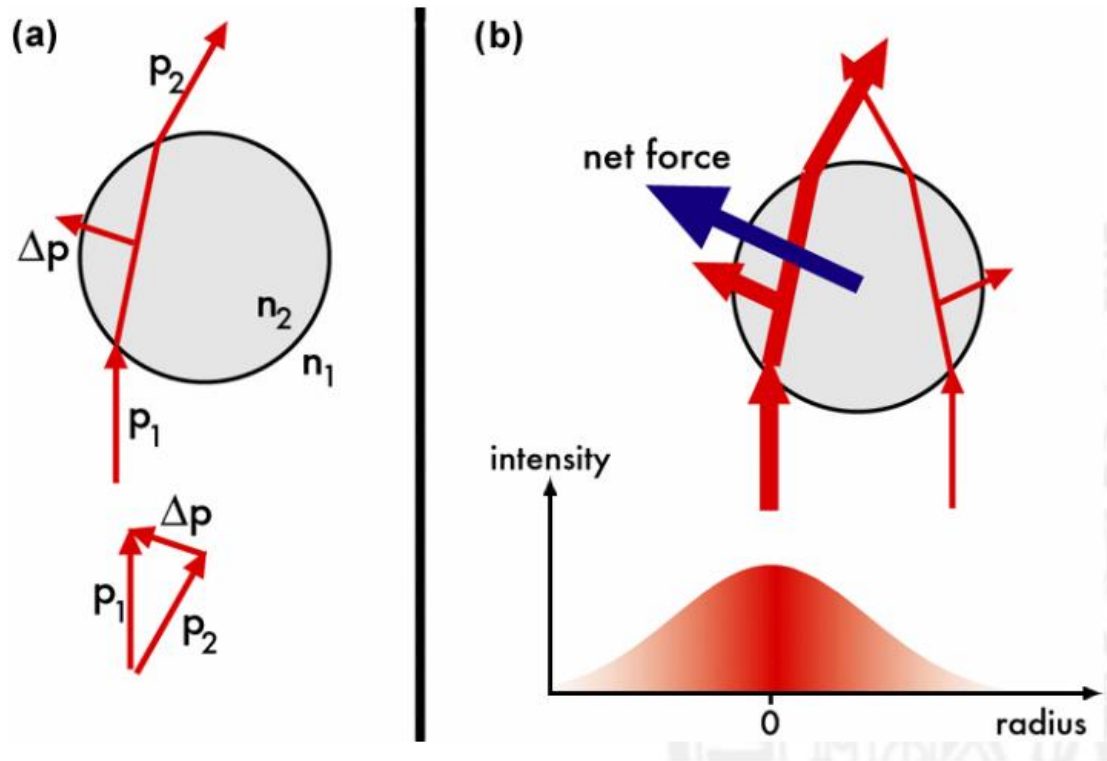


Figure from <http://home.uni-leipzig.de>

Consider the light ray  $p_1$  in (Fig. 2.10 A). Moving from the lower index of refraction surrounding medium into the higher index bead, its path will be bent towards the surface normal when entering the bead, and away from the normal when exiting as shown. This change in light direction will impart some momentum on the bead, roughly towards the side of the bead that the light entered. Of course, there will also be light

entering the opposite side of the bead as illustrated in (Fig. 2.10 B). However, one of the sides will be closer to the center of the beam, thus having a higher flux of light pass through it, thus imparting a greater force. Therefore, the bead feels a force moving it toward the beam center—a restoring force.

The above argument merely motivates the existence of a restoring force in the lateral directions, it does not allow us to calculate it or give us a functional form. In practice, one must calibrate the value of the restoring force experimentally, and only work with small displacements from the center of the trap so that the force can be approximated as a linear function of distance from the center of the trap.

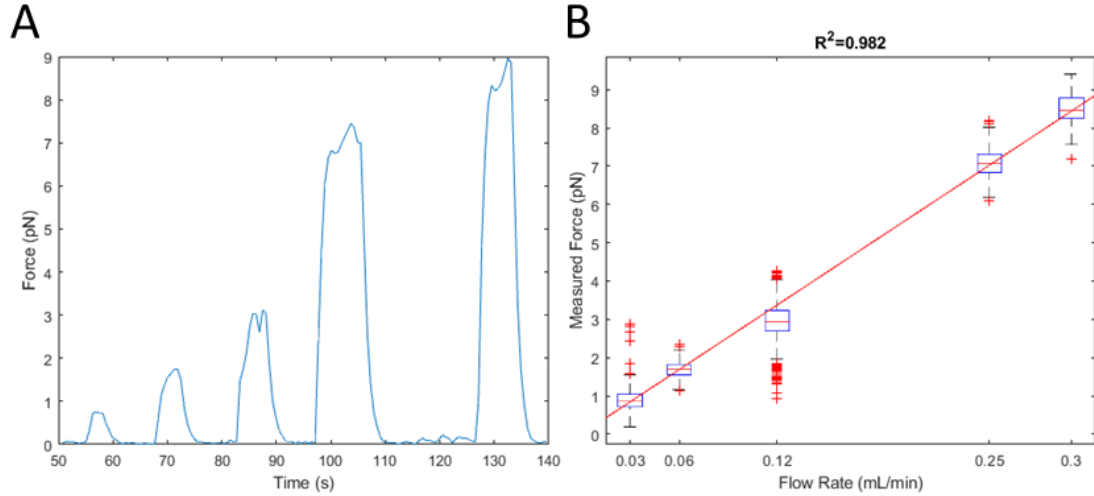
#### **2.5.4 Flow Calibration of Optical Trap**

To verify that our measured forces were accurate, we measured the trapping force of beads subjected to lateral flow of medium through the flow cell generated by the programed addition of medium at a constant rate by a syringe pump (syringepump.com). The resulting force graphs are shown in (Fig. 2.11 A). The spikes in this graph represent flows of .03, .06, .12, .25, and .3 mL/min. Because the optical trap was designed to trap beads close to the surface of the flow-cell, the forces registered by the optical tweezers were significantly less than the value calculated from assuming homogenous flow. The measured forces fit the expected linear relationship between flow rate and force with a  $R^2$  value of .982 (Fig. 2.11 B), proving that the tweezers were correctly calibrated at least up



to a multiplicative constant. As our experiments were relative in nature, this would be sufficient for our purposes.

**Figure 2.11: Flow calibration of the optical tweezers**

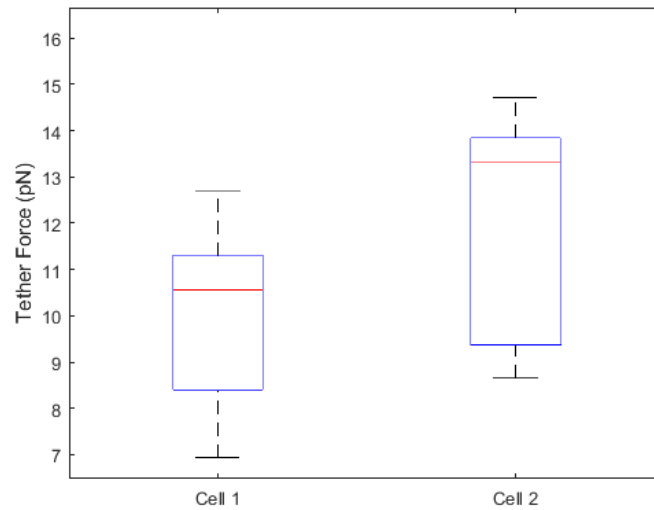


A) Time-course of a flow-calibration experiment. The trapped bead was subjected to intermittent flows of increasing strength. B) Quantification of the relationship between flow rate and measured force. The data fit the expected model of a line with 0 intercept with a  $R^2$  value of .982.

### 2.5.5 Verification of the consistency of tension measurements

To verify that our tether measurement technique gave consistent results, we preformed repeated measurements of tether force on the same cell with several different beads. In two separate experiments, we saw that the variation of the tether force was roughly 20%, giving us an estimate of the precision of our measurements of cell tension.

**Figure 2.12: Repeated tether measurements from the same cell**



Boxplots of the results of repeatedly measuring the tether force from the same cell. The red lines correspond to the median of the data, the boxes represent the interquartile range, and the whiskers represent the extrema. Standard deviations roughly correspond to 20% of the measured force

### **2.5.6 Cell Culture and Reagents**

BSC1 and U373 cells (gift of Steeve Boulant, Department of Infectious Diseases, Virology, Heidelberg University, Germany) were grown in Dulbecco's modified Eagle's medium (DMEM) containing 10% fetal bovine serum, penicillin/streptomycin. The final concentrations of M $\beta$ CD (Sigma-Aldrich) was 4 mM in serum-free L15

### **Chapter 3 Clathrin-mediated endocytosis subject to elevated membrane tension**

Derived from: Ferguson, J.P.\*, Huber, S.D.\*, Willy, N.M., Aygün, E., Goker, S., Atabey, T., and Kural, C. (2017). Mechanoregulation of clathrin-mediated endocytosis. *J. Cell Sci.* 130, 3631–3636.

*In this chapter my contributions are some osmotic shock experiments and analysis; development of two-color master-slave analysis; two-color clathrin/actin experiments and analysis; and average z-position analysis.*

#### **3.1 Abstract**

We characterized the tension response of clathrin-mediated endocytosis by using various cell manipulation methodologies. Elevated tension in a cell hinders clathrin-mediated endocytosis through inhibition of de novo coat initiation, elongation of clathrin coat lifetimes and reduction in the maximum rate of clathrin accumulation. Actin machinery supplies an inward pushing force necessary for internalization of clathrin coats under high tension. These findings suggest that the physical cues cells receive from their microenvironment are major determinants of clathrin-mediated endocytic activity.

### 3.2 Introduction

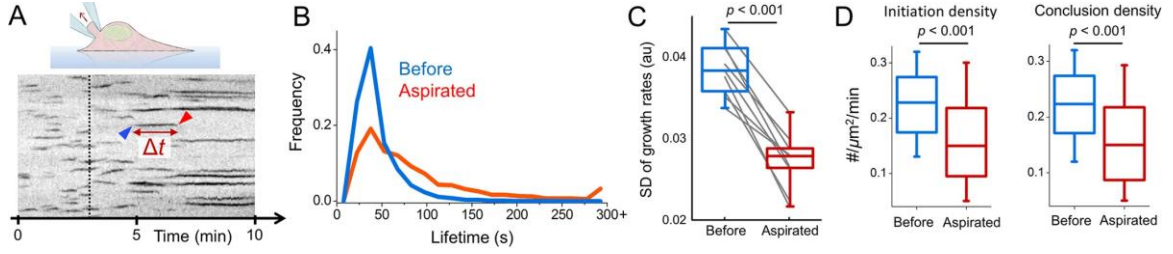
Clathrin-coated structures bear a major fraction of the endocytic load from the plasma membrane of eukaryotic cells. During the formation of an endocytic vesicle, clathrin heterohexamers assemble into a multifaceted cage that is linked to the plasma membrane by clathrin adaptors. Tension on the membrane hinders this process as it increases the energy cost of curvature formation (Sheetz, 2001). Curvature-bearing clathrin-coated pits are replaced by less-dynamic shallow coats when tension is elevated (Saleem et al., 2015). In various cellular contexts, actin dynamics supplements the energy required for formation of clathrin-coated vesicles under high membrane tension (Aghamohammadzadeh and Ayscough, 2009; Boulant et al., 2011; Kaur et al., 2014). However, actin-dependent clathrin-mediated endocytic events have a longer duration than their counterparts taking place at lower tension levels (Boulant et al., 2011). Here, we characterized the regulation of clathrin coat dynamics by membrane tension using cell manipulation techniques (i.e. microaspiration, cell squeezing and hypo-osmotic swelling) coupled with fluorescence live-cell imaging. Our results show that the density of endocytic clathrin-coated structures on the plasma membrane depends on tension, and actin machinery rescues internalization of clathrin coats under high tension by moving clathrin coats away from the membrane.

### 3.3 Results

We used three independent approaches to increase the tension on the plasma membrane while monitoring clathrin coat dynamics at the ventral (adherent) surface of cells.

Applying negative pressure on the plasma membrane by micropipette aspiration is an effective way to increase tension (Herant et al., 2005; Houk et al., 2012). We detected a significant increase in average clathrin coat lifetime (time elapsed between the origination and conclusion of the coat;  $44 \pm 23$  s versus  $88 \pm 73$  s, mean  $\pm$  s.d.,  $P < 0.001$ ;  $n_{cells}=9$ ,  $n_{traces}=40,943$ ; Fig. 3.1 A,B) in BSC1 cells upon microaspiration of the membrane. Impeded clathrin coat dynamics can also be observed as gradual disappearance of high-magnitude growth rates in clathrin traces (Ferguson et al., 2016). The standard deviation of clathrin growth rate distributions in our cells upon microaspiration decreased [ $0.038 \pm 0.003$  (before aspiration) versus  $0.027 \pm 0.004$  (during aspiration),  $P < 0.001$ ; Fig. 3.1 C]. We also found that increased tension reduced the surface density of clathrin coat initiation and conclusion events (Fig. 3.1 D).

**Figure 3.1: Aspiration of the plasma membrane slows down clathrin coat dynamics.**



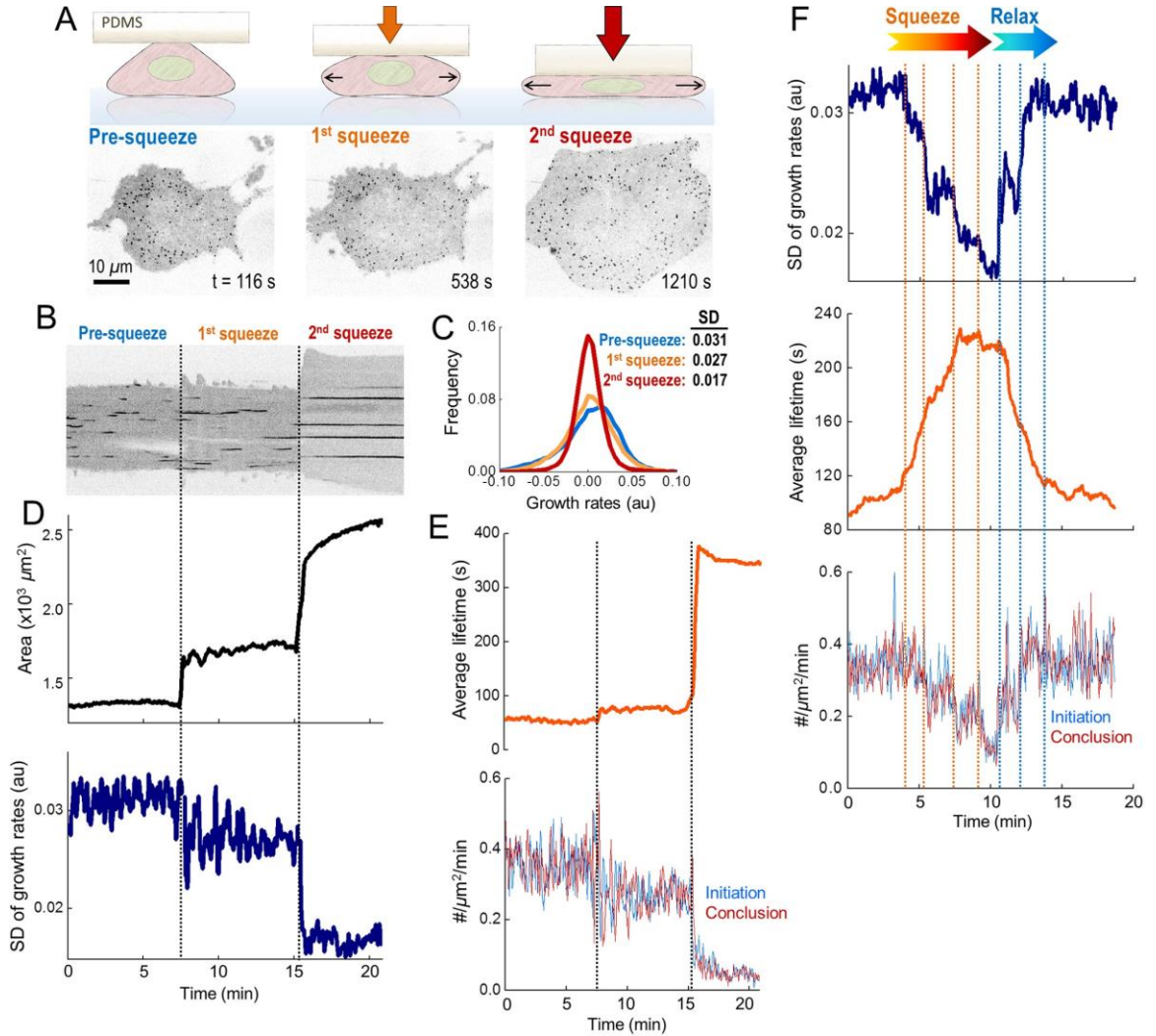
(A) Kymograph showing the clathrin activity at the ventral surface of a BSC1 cell expressing AP2–eGFP. Clathrin coat traces elongate gradually upon microaspiration (dashed line; Movie 1). Blue and red arrowheads mark the initiation and conclusion of a clathrin-coated structure, respectively.  $\Delta t$  is its lifetime. (B) Clathrin coat lifetime distributions are shown for nine BSC1 cells imaged before and during microaspiration ( $n_{\text{traces}}=40,943$ ). (C) For the same nine cells, the standard deviation of the clathrin growth rate distributions are shown in boxplots. Lines connect the standard deviation values obtained from the same cell before and during aspiration. The narrower growth rate distributions indicate slower clathrin coat dynamics. (D) Box plots are the initiation and conclusion densities of clathrin-coated structures before and during aspiration. In the boxplots, the box represents the 25–75th percentiles, and the median is indicated. The whiskers show the 10–90th percentiles. P-values were obtained with a two-tailed t-test.

To induce faster changes in plasma membrane tension, we increased the hydrostatic pressure in cells by squeezing them with a micromanipulator-controlled polymer cushion (Fig. 3.2 A,B). We used growth rate distributions obtained from clathrin coat intensity profiles to temporally resolve the rapid alterations in endocytic dynamics induced by squeezing (Ferguson et al., 2016). In good agreement with the microaspiration experiments, fast dissolution and fast formation phases in the growth rate distributions diminished with the increasing tension, whereas the frequency of the plateau phase increased (Fig. 3.2 C). Discrete changes in the tension could be resolved as stepwise reduction in the standard deviation of clathrin growth rates (Fig. 3.2 D). Furthermore, the average clathrin coat lifetimes increased while initiation and conclusion

densities decreased (Fig. 3.2 B,E). When we relieved the squeezing to verify the viability of cells, we found that the parameters determining clathrin coat dynamics reverted to normal (Fig. 3.2 F).

Hypotonic swelling is a straightforward and widely used approach to increase membrane tension (Boulant et al., 2011; Cocucci et al., 2014; Diz-Muñoz et al., 2016). Upon reducing the osmolarity of the imaging medium, we found that hypotonic swelling takes effect within minutes but the volume of cells converges back to the original values within an hour (Fig. 3.3 A). As expected, the temporary increase of the tension due to stretching of the membrane affected endocytic clathrin coat dynamics only temporarily (Fig. 3.3 B). We found that the average lifetime of clathrin-coated structures increased significantly in SUM159 cells (Aguet et al., 2016) under hypoosmotic shock ( $87 \pm 86$  s versus  $161 \pm 208$  s, mean  $\pm$  s.d.,  $P < 0.001$ ;  $n_{\text{cells}}=12$ ,  $n_{\text{traces}}=34,113$ ; Fig. 3.3 C). In accordance with the microaspiration and cell squeezing assays, increased tension resulted in reduction of the standard deviation of clathrin growth rates [ $0.018 \pm 0.003$  (pre-osmoshock) versus  $0.014 \pm 0.002$  (post-osmoshock),  $P < 0.001$ ; Fig. 3.3 D], and initiation and conclusion densities (Fig. 3.3E).

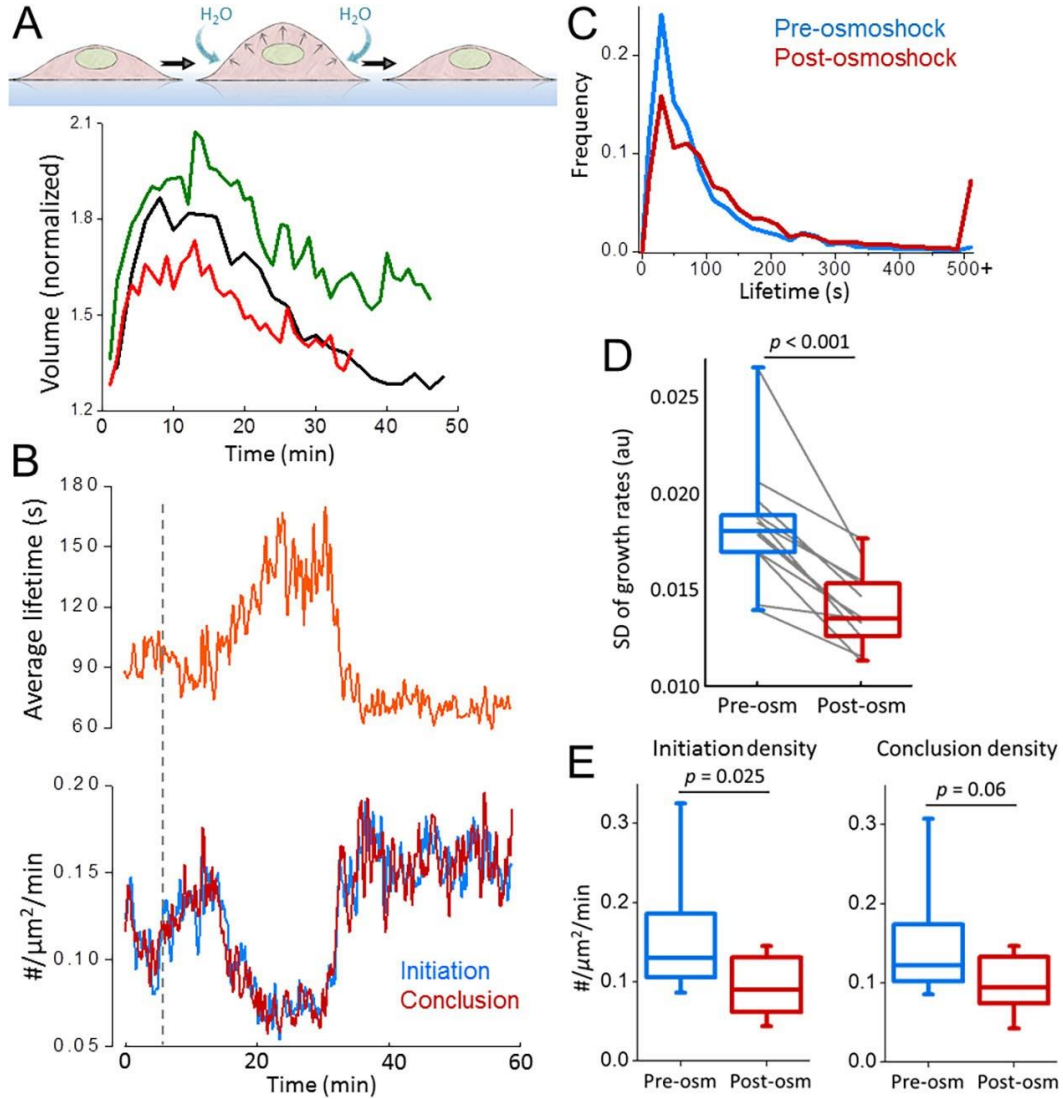
**Figure 3.2: Cell squeezing induces fast and reversible alterations in clathrin coat dynamics.**



(A) Cartoon and representative frames of a BSC1 cell are shown at different stages of squeezing. (B) Kymograph showing the temporal evolution of the clathrin traces detected at the ventral surface of the cell shown in A. Dashed lines mark the squeezing steps. (C) For the cell in A, normalized distributions of clathrin growth rates are plotted for different squeezing levels. The standard deviation of the distribution decreases as the tension increases. (D) For the same cell, the time variation of the ventral surface area (upper) and the standard deviation of the clathrin growth rates (lower). The stepwise changes in these parameters are due to stepwise changes in squeezing. (E) The response of the same cell to squeezing is shown as the mean clathrin lifetime (upper) and initiation and conclusion densities (lower). Dashed lines indicate change in squeezing ( $n_{\text{traces}}=8217$ ). (F) Standard deviation of clathrin growth rates (upper), mean lifetime (middle), and initiation and conclusion densities (lower) from a cell that undergoes increased stepwise squeezing (orange dashed lines) and relaxation (blue dashed lines) ( $n_{\text{traces}}=8255$ ).



**Figure 3.3: Hypotonic swelling inhibits clathrin coat dynamics temporarily.**

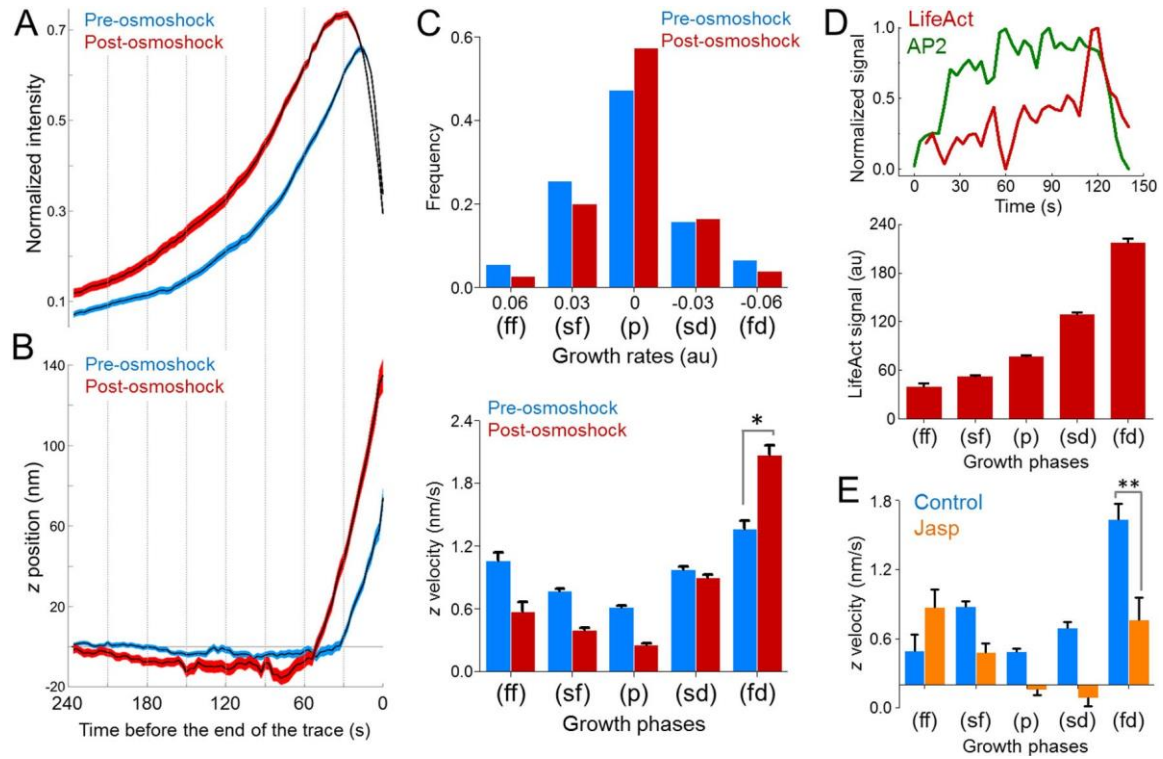


(A) Change in the volume (normalized to the initial value) is plotted for three BSC1 cells during hypotonic swelling (i.e. osmoshock). (B) Mean clathrin coat lifetime (upper), and initiation and conclusion densities (lower) are plotted against time for a BSC1 cell treated with hypotonic shock (dashed line). (C) Clathrin lifetime distributions are assembled pre- and post-osmoshock for 12 gene-edited SUM159 cells expressing AP2-eGFP ( $n_{\text{traces}}=34,113$ ). (D, E) For the same cells, the standard deviation of clathrin growth rates (D) and initiation and conclusion densities of clathrin-coated structures pre- and post-osmotic shock (E) are shown in boxplots. Lines connect the standard deviation values obtained from the same cell pre- and post-osmoshock. In the boxplots, the box represents the 25–75th percentiles, and the median is indicated. The whiskers show the 10–90th percentiles. P-values were obtained with a two-tailed t-test.

As plasma membrane tension increases, actin polymerization energy becomes indispensable for invagination of clathrin-coated pits. Therefore, inhibition of the actin machinery arrests clathrin coats prior to the scission phase (Boulant et al., 2011). There are two proposed models for actin-dependent formation of clathrin-coated vesicles under high tension (Hassinger et al., 2017). The first model predicts a vertical force generated by actin polymerization to move the clathrin coat away from the plasma membrane. The second model suggests formation of an actin collar that constricts the neck region directly (Collins et al., 2011). By tracing the three-dimensional (3D) displacement of clathrin-coated structures, we found that coats move ~100 nm into the cell before uncoating, and the inward displacement is significantly higher when the membrane tension is increased by hypotonic swelling (Fig. 3.4 A,B). We also found that the axial velocity of the inward movement is the highest during the fast dissolution phase of clathrin coats (Fig. 3.4 C). We adapted a master–slave approach (Aguet et al., 2013) to monitor the intensity profiles of clathrin coats (AP2S1–eGFP as the master; hereafter denoted AP2–eGFP) and colocalizing actin filaments (LifeAct–mCherry as the slave), simultaneously. As expected, the LifeAct signal peaked during the later stages of clathrin-coated vesicle formation (Fig. 3.4 D), and the axial velocity detected during the fast dissolution phase reduced significantly when the actin dynamics is inhibited upon jasplakinolide treatment (Fig. 3.4 E). These results indicate that actin polymerization provides the inward force that is required for constriction of the neck under high membrane tension, a mechanism

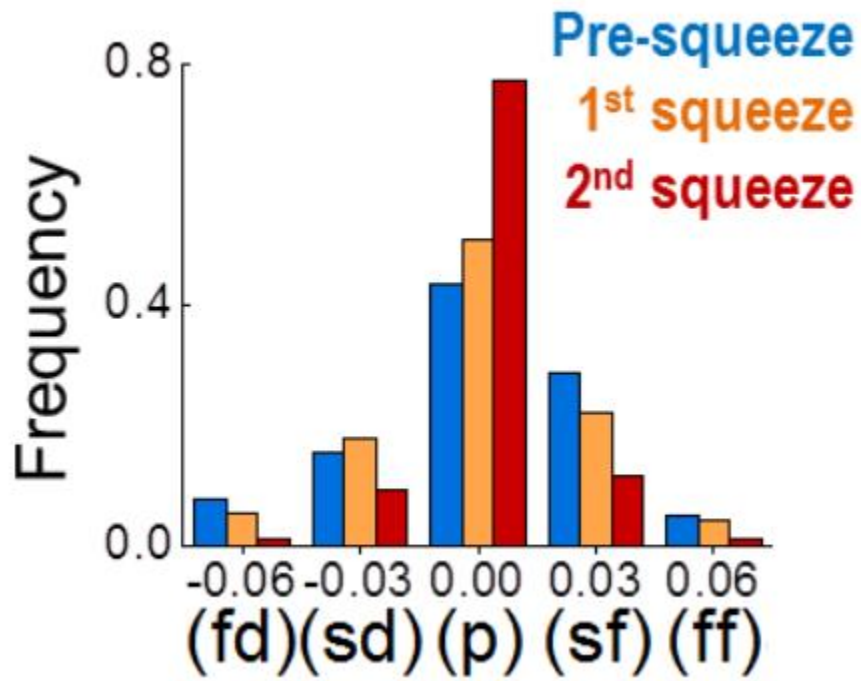
analogous to clathrin-mediated endocytosis in yeast (Aghamohammadzadeh and Ayscough, 2009).

**Figure 3.4: Actin dynamics mediate the inward movement of clathrin coats prior to disassembly.**



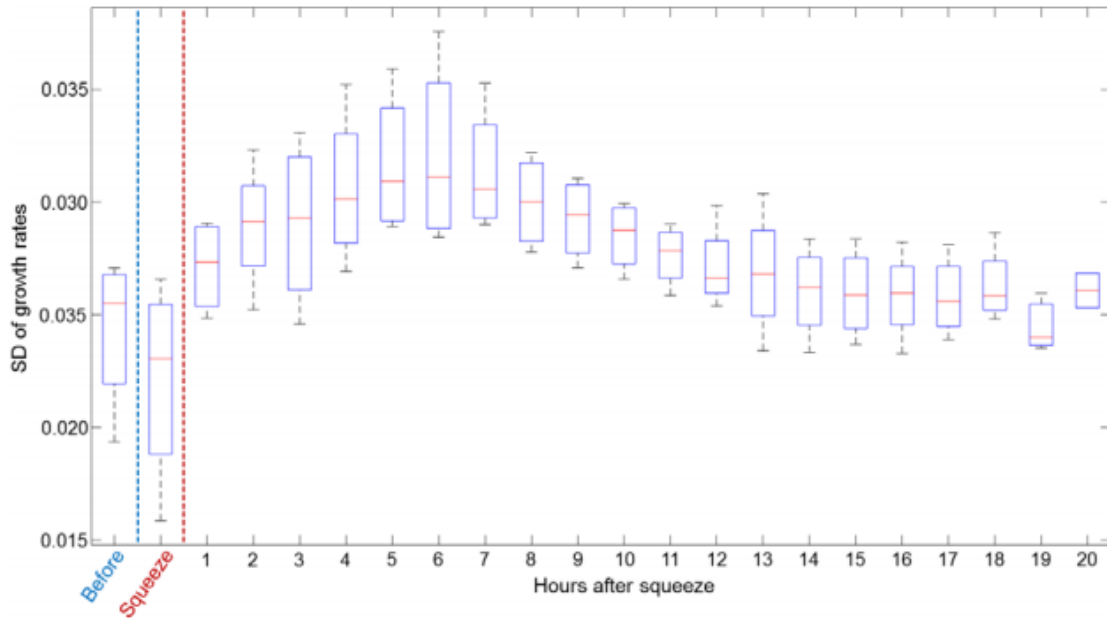
(A) Mean $\pm$ s.e.m. values for of normalized AP2 intensity traces (determined for a SUM159 cell before and after hypotonic swelling;  $n_{\text{traces}}=3728$ ). The traces are aligned at the end point before averaging. (B) Mean $\pm$ s.e.m. z displacements are shown for the two trace groups in A. (C) Top, growth rate distributions are assembled for eight SUM159 cells before and after hypotonic swelling ( $n_{\text{traces}}=30,409$ ). Different growth phases (ff, fast formation; sf, slow formation; p, plateau; sd, slow dissolution; fd, fast dissolution) were determined by quantifying the change in the clathrin coat signal over 12-s-long time windows (Ferguson et al., 2016). Bottom, for the same cells, bar plots show the mean $\pm$ s.e.m. of the z velocities of the trace fragments (12 s long) that are used to generate the growth rate distributions above. Trace fragments that have the highest z velocity are found in the fast dissolution (fd) phase. (D) Top, representative intensity traces of AP2 (green) and LifeAct (red) fluorescence during the formation of a clathrin-coated vesicle at the ventral surface of a BSC1 cell. Bottom, the relative LifeAct intensity (mean $\pm$ s.e.m.) colocalizing with clathrin coats is shown for different growth phases ( $n_{\text{cells}}=4$ ,  $n_{\text{traces}}=28,795$ ). Note that the growth phases are determined by using the master (AP2-eGFP) signal. (E) Bar plots show the z velocities (mean $\pm$ s.e.m.) corresponding to different growth phases for AP2 traces obtained from BSC1 cells in the absence and presence of jaspalokinide (Jasp) (Control,  $n_{\text{cells}}=7$ ,  $n_{\text{traces}}=20,204$ ; Jasp,  $n_{\text{cells}}=6$ ,  $n_{\text{traces}}=35,972$ ). \* $P<0.0001$ ; \*\* $P<0.001$  (two-tailed t-test).

Figure 3.5: Squeezing Growth Rates



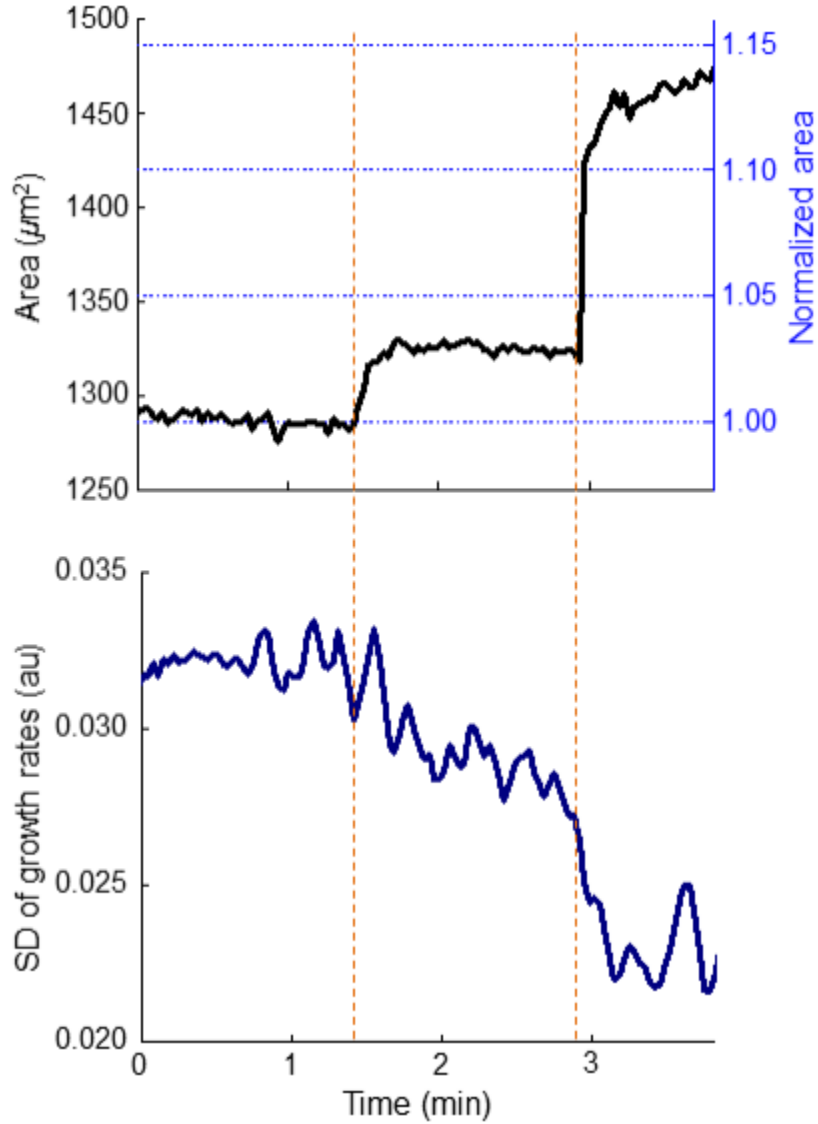
The growth rates at distinct levels of squeezing (Fig. 2C) are assembled in five bins that represent the different phases of clathrin-coated vesicle formation (fd, fast dissolution; sd, slow dissolution; p, plateau; sf, slow formation; ff, fast formation).

**Figure 3.6: Post-Squeeze dynamics**



To verify the viability of BSC-1 cells after squeezing we monitored the clathrin coat activity for up to 20 hours. We imaged cells for 2 minutes in each hour to minimize photobleaching and phototoxicity. The box plots show the SD of clathrin coat growth rates determined at different time points (Ncells = 4, Ntraces = 139678). The increased SD of growth rates after squeezing step signifies the retrieval of the endocytic dynamics in cells. Boxes extend to the quartiles, with a line at the median. Whiskers extend from the minimum to the maximum value.

Figure 3.7: Squeezing and area change



During development of the *Drosophila* wing imaginal disc, compression of the tissue changes the projected area of the center cells  $\sim 1.5$  fold (Aegerter-Wilmsen et al., 2012). In our squeezing experiments, compressions that result in milder changes in the projected cell area produce observable changes in clathrin coat dynamics. The upper panel shows the change in the area of a BSC-1 cell during two squeezing steps (shown by the orange dashed lines). The axis on the right shows the cell area normalized to the average pre-squeeze level. The lower panel is the change in the SD of clathrin coat growth rates.

### 3.4 Discussion

In this study, we used quantitative live-cell imaging in combination with diverse cell manipulation techniques to detect the changes in clathrin coat dynamics as cells undergo mechanical perturbations. This powerful approach allowed us to investigate the response of individual cells to mechanical stimuli in real time, rather than making a comparative analysis between different cells. Collectively, our assays reveal an inverse relationship between plasma membrane tension and endocytic clathrin coat dynamics. Increased tension manifests itself as reduced initiation and conclusion densities, elongated lifetime, and a reduced standard deviation of the clathrin coat growth rate distribution. These results suggest that the reduced density of clathrin-coated structures observed during mitosis (Aguet et al., 2016) and at the lamellae of migrating cells (Kural et al., 2015) can be a product of increased membrane tension (Fogelson and Mogilner, 2014; Kaur et al., 2014; Lieber et al., 2015; Raucher and Sheetz, 1999). Correspondingly, previously described feedback regulation between membrane tension and membrane-bending proteins in migrating cells (Tsujita et al., 2015) can explain the stark increase in clathrin coat density upon mechanical inhibition of cell protrusion.

Our results show that tension is an effective, fast-acting and reversible regulator of clathrin-mediated endocytosis. To induce hypotonic swelling, we reduced the osmolarity of the imaging medium to 63 mOsm. In a recent study, comparable changes in osmolarity are shown to increase the membrane tension  $\sim 2$ -fold (Diz-Muñoz et al.,



2016). This is within the boundaries of physiologically relevant variances in plasma membrane tension given that spreading of a cell results in an ~3-fold reduction in membrane tension (Gauthier et al., 2009), and the tension at the apical surface of polarized cells is ~2.5-fold higher than that at the basal surface (Dai and Sheetz, 1999). Compression of cells by surrounding mechanical cues has been proposed to control tissue morphogenesis at different stages of metazoan development (Desprat et al., 2008; Legoff et al., 2013; Rauskolb et al., 2014). In our cell-squeezing assays, we observed changes in clathrin-mediated endocytic activity even when the relative fold change in the cell area is lower than the levels detected in developmental processes associated with cell compression (Aegerter-Wilmsen et al., 2012). Dynamics and organization of the actin cytoskeleton were unperturbed in these assays. These findings suggest that morphological alterations involving mechanical forces within physiological contexts can induce abrupt changes in clathrin coat dynamics. Consequently, mechano-regulation of clathrin-mediated endocytosis can influence related biological processes that are central for development and homeostasis of multicellular organisms, such as signal transduction and cell shape regulation.

### **3.5 Materials and Methods**

#### **3.5.1 Cell culture, reagents and fluorescence imaging**

BSC1 cells stably expressing AP2–eGFP (gift of Steeve Boulant, Department of Infectious Diseases, Virology, Heidelberg University, Germany) were grown in Dulbecco's modified Eagle's medium (DMEM) containing 10% fetal bovine serum, penicillin/streptomycin. SUM159 cells gene edited to express AP2–eGFP (Aguet et al., 2016) (gift of Tomas Kirchhausen, Departments of Cell Biology and Pediatrics, Harvard Medical School Boston, MA) were grown in F-12 medium containing 5% fetal bovine serum (FBS), penicillin-streptomycin and hydrocortisone. Transient expression of LifeAct–mCherry (gift of Patrick M. Reeves, Vaccine & Immunotherapy Center, Charlestown, MA) in BSC1 cells stably expressing AP2–eGFP was carried out using Lipofectamine 2000 (Invitrogen) following the manufacturer's instructions, and imaging was performed 24–48 h after transfection. The final jasplakinolide (Enzo Life Sciences) concentration used to inhibit actin dynamics was 1  $\mu$ m.

The fluorescence imaging system is composed of an Eclipse TI-E microscope (Nikon) equipped with a perfect focusing system (PFS), a temperature-controlled chamber, a CSU-W1 spinning disk confocal unit (Yokogawa Electric Corporation), a 100 $\times$  objective lens (Nikon CFI PlanApochromat Lambda, NA 1.45) and an EMCCD camera (iXon DU897 Ultra; Andor Technology). All image acquisition was performed by using NIS Elements software.

Imaging of cultured cells was performed 30 min after plating on glass bottom dishes (Greiner Bio-One) in the case of squeezing cells. The plating time prior to aspiration and osmotic shock experiments was 24 h. All cells were maintained at an ambient temperature of 37°C during imaging. Images were acquired at a rate of 0.25–0.5 Hz with a laser exposure of 50–300 ms per frame. Imaging medium was Phenol Red-free L15 (Thermo Fisher Scientific) supplemented with 10% FBS. The snapshots and movies of fluorescence acquisitions are inverted to increase visibility.

### **3.5.2 Squeezing, micropipette aspiration and osmotic shock**

In squeezing experiments, a 15  $\mu$ l suspension of cells and imaging medium is plated in the middle of the imaging dish, forming a small droplet. A polydimethylsiloxane (PDMS) brick of  $\sim 10$  mm $\times$ 10 mm $\times$ 2.5 mm is placed on top of the droplet. The dish is capped and the cells are allowed to spread for  $\sim 30$  min (at this point cells are not in contact with the PDMS). After spreading, a micromanipulator (Narishige MMO-202ND, Narishige MMN-1) fitted with a rounded glass pipette tip is slowly brought into contact with the PDMS brick from above. The micromanipulator is used to press down on the PDMS while observing the cells under brightfield illumination. Fluorescence acquisitions start after the PDMS brick is brought into contact with the cells. The maximum level of compression is signaled by complete halting of clathrin coat activity. Further imaging is performed at various stages while the compression is released. In the microaspiration

experiments, a microinjection system (BRE110/E; Sutter Instrument) was used to control the negative pressure applied on the dorsal surface of cells via a 5–10- $\mu$ m-thick microneedle.

For osmotic shock experiments, SUM159 cells are cultured on four-well glass bottom plates (Fisher Scientific) and imaged every 3 s. At 5 min after the start of the experiment, 800  $\mu$ l of ddH<sub>2</sub>O is added to the 200  $\mu$ l of imaging medium to induce hypo-osmotic shock. The measured osmolarity level after this dilution is 63 mOsm. The cells are then imaged for another 20 min to study the cellular response. To compare clathrin coat dynamics before and after osmotic shock, two time windows are analyzed: the pre-osmoshock time window consists of the 5 min immediately prior to addition of water, whereas the post-osmoshock time window starts 2.5 min after water addition (to allow time for osmotic shock effects fully take hold) and runs for 5 min. For lifetime analyses, only traces whose mean time-point lies within the window are considered.

For the calculation of the cell volume, we used the 3D time-lapse spinning-disk confocal microscopy acquisitions. A custom MATLAB program was written to allow the user to select the boundary of the cell for each plane in a z-stack (available from the corresponding author upon request). The number of pixels inside of these boundaries was multiplied by the size of the pixels to determine the area of the cell in that stack. The volume was calculated by multiplying this area by the difference in position between the stacks and adding all those values together.

### 3.5.3 Single-particle tracking

cmeAnalysis software was used for two dimensional (2D) particle tracking (obtained from <http://lccb.hms.harvard.edu/software.html>) (Aguet et al., 2013). We used exclusionary criteria for the traces that last a single frame or persist consistently in the background without following a characteristic clathrin intensity profile (Ferguson et al., 2016). Selected traces are at least three frames long and contain a sequence that meets statistical criteria for demonstrating a linear increase or decrease in intensity (corresponding to clathrin coat growth and dissolution, respectively). Rejected traces were excluded from the calculation of initiation and dissolution densities, growth rate distributions, lifetime distributions and lifetime dipoles.

We used the traces that passed the rejection scheme to determine the average clathrin coat lifetime per frame. In each frame, we added together the lifetime of each trace that exists in that frame, and divided by the number of traces considered. The beginning and end of each trace is considered as an initiation and conclusion event, respectively. For each frame, initiation and conclusion densities (number/ $\mu m^2$  /minute) were determined by finding the number of traces that begin and end in that frame, multiplying by the frame length (2–4 s), dividing by the visible cell area (in  $\mu m^2$  ) and by 60 s.

A custom MATLAB program was used for the master–slave analysis (available from the corresponding author upon request). The traces in the master channel were determined by using the cmeAnalysis software as described above. To quantify the intensity in the slave channel, we determined the average intensity in a  $5\times 5$  pixel region around the structure, and then subtracted the background intensity, which was calculated as the average intensity of the outside pixels of the  $7\times 7$  pixel region around the structure.

3D traces and growth rate distributions of clathrin coats were determined as described previously (Ferguson et al., 2016). Z-velocities are calculated for each 12-s long trace fragment, which were used to determine the corresponding clathrin growth rates.

## **Chapter 4 Using clathrin coat dynamics to assess membrane tension differences**

Derived from: Willy, N.M., Ferguson, J.P., Huber, S.D., Heidotting, S.P., Aygün, E., Wurm, S.A., Johnston-Halperin, E., Poirier, M.G., and Kural, C. (2017). Membrane mechanics govern spatiotemporal heterogeneity of endocytic clathrin coat dynamics. *Mol. Biol. Cell* 28, 3480–3488.

*In this chapter, my contributions are deoxycholate experiments and some cholesterol depletion and osmotic shock experiments and analysis; some spreading analysis; and all optical tweezer experiments and analysis*

### **4.1 Abstract**

Dynamics of endocytic clathrin-coated structures can be remarkably divergent across different cell types, cells within the same culture, or even distinct surfaces of the same cell. The origin of this astounding heterogeneity remains to be shown. Here we show that cellular processes associated with changes in effective plasma membrane tension induce significant spatiotemporal alterations in endocytic clathrin coat dynamics. Spatiotemporal heterogeneity of clathrin coat dynamics is also observed during morphological changes

taking place within developing multicellular organisms. These findings suggest that tension gradients can lead to patterning and differentiation of tissues through mechanoregulation of clathrin-mediated endocytosis.

## **4.2 Introduction**

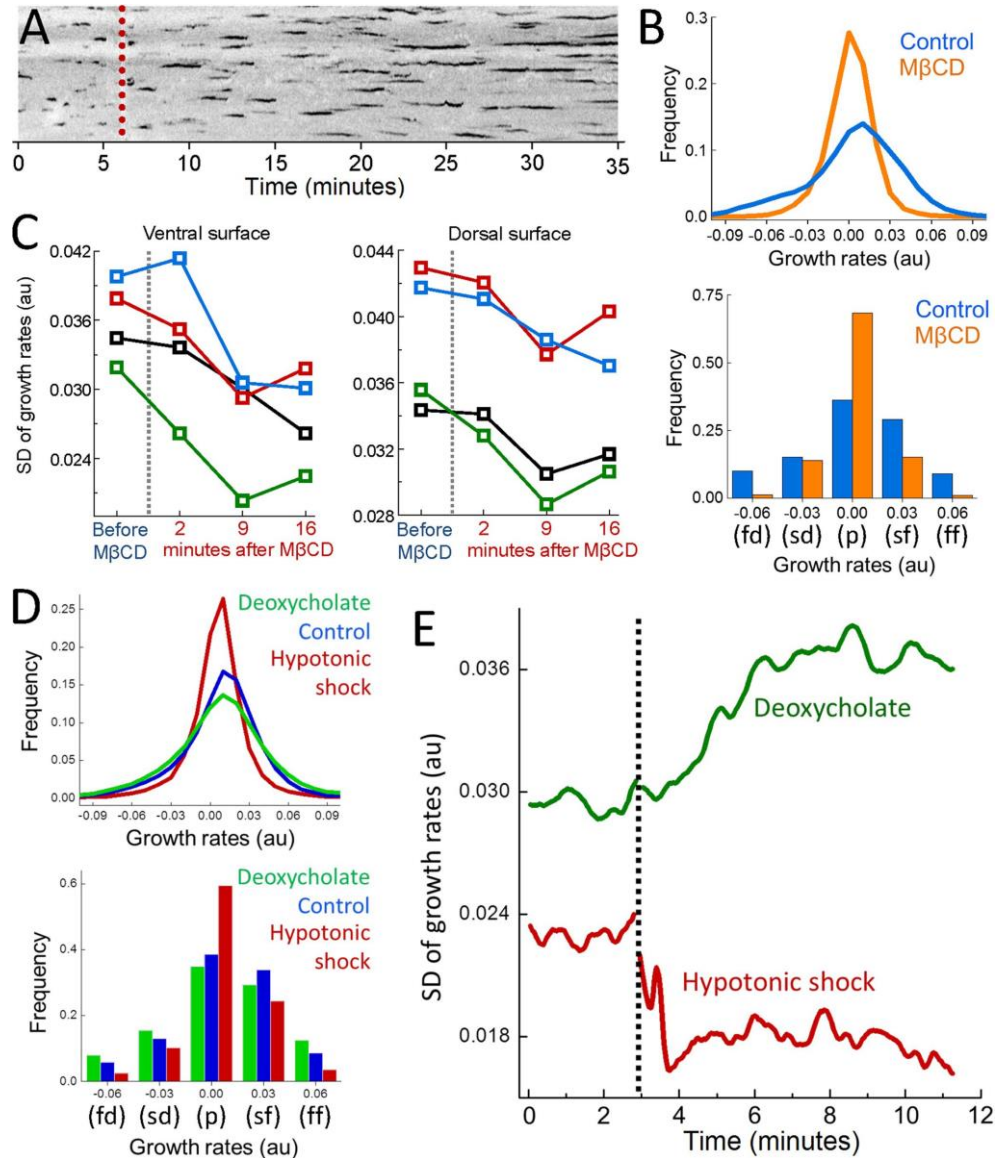
Clathrin-mediated endocytosis (CME) is the most prominent internalization mechanism of membrane lipids and proteins from the cell surface. The major building blocks of endocytic clathrin coats, clathrin triskelions, can assemble into polyhedral cages in a seemingly infinite number of geometries (Heuser et al., 1987; Heuser, 1989). The dynamic properties of clathrin-coated structures can be strikingly diverse as well. Lifetime--the time it takes for formation and internalization of endocytic clathrin coats--can be an order of magnitude disparate even between structures within the same cell (Ferguson et al., 2016). Here we show that cellular processes associated with membrane tension gradients, namely spreading and migration, result in increased spatiotemporal heterogeneity of endocytic clathrin coat dynamics. The variations in clathrin coat dynamics coincide with gradients in plasma membrane tension, which is a potent regulator of endocytic processes (Dai and Sheetz, 1995). We also show that spatiotemporal changes in clathrin coat dynamics take place during developmental processes shaping *Drosophila melanogaster* embryos.



### 4.3 Results

Physical factors that increase the energy cost of curvature generation on the plasma membrane slow down formation of clathrin-coated vesicles. Using quantitative imaging of fluorescently tagged clathrin coat components (clathrin or AP2) within live cells, this phenomenon can be observed as elongated coat lifetime (Figure 4.1 A) (Boulant et al., 2011). Alternatively, mechano-regulation of CME dynamics can be monitored at distinct surfaces of a cell through growth rate distributions, which are assembled by quantifying the changes in the fluorescence signal of individual clathrin coats within short time windows (Ferguson et al., 2016). High magnitude growth rates, that is, rapid changes in the clathrin coat intensity corresponding to fast formation and fast dissolution of the coat, diminish with increasing plasma membrane tension. Therefore, the standard deviation (SD) of the growth rate distributions decreases when the effective membrane tension is increased by cholesterol depletion or hypotonic swelling (Figure 4.1 B–E) (Dai et al., 1998; Khatibzadeh et al., 2012; Diz-Muñoz et al., 2016; Sun et al., 2007). Conversely, SD of growth rate distributions increases when tension is reduced by deoxycholate treatment (Figure 4.1 D and E) (Raucher and Sheetz, 1999; Batchelder et al., 2011).

**Figure 4.1: Monitoring mechanoregulation of clathrin coat dynamics in real time.**



(A) Depletion of plasma membrane cholesterol by methyl- $\beta$ -cyclodextrin (M $\beta$ CD) increases the adhesion energy between membrane and the cytoskeleton, and thereby inhibits curvature formation by clathrin-coats (Subtil et al., 1999; Sun et al., 2007; Khatibzadeh et al., 2012). A 35-min-long kymograph shows clathrin coat dynamics at the ventral surface of a BSC1 cell stably expressing the  $\sigma 2$  subunit of AP2 fused with enhanced green fluorescent protein (EGFP). The dashed line marks the addition of M $\beta$ CD. The traces corresponding to individual clathrin-coated structures elongate as clathrin pits are gradually replaced by less dynamic flat arrays (plaques).

Continued

## Figure 4.1: Continued

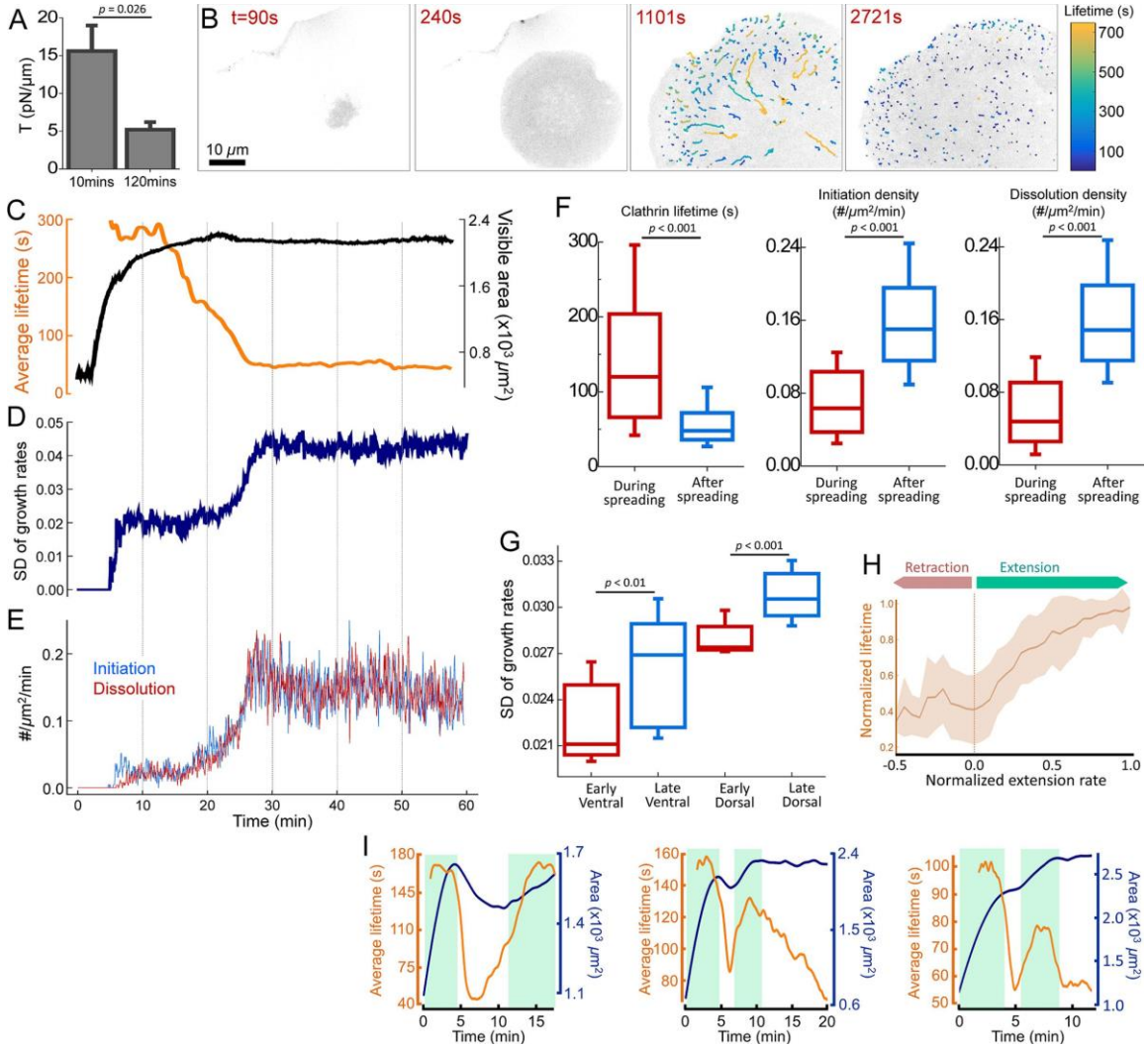
(B) For the cell in A, growth rate distributions are assembled using the traces detected before cholesterol depletion (Control; the first 5 min of the acquisition) and after (MBCD; the last 5 min of the acquisition). As clathrin coat dynamics slow down, growth rate distribution gets narrower (top). The distribution is also displayed using five bins corresponding to five growth phases (bottom; fd: fast dissolution, sd: slow dissolution, p: plateau, sf: slow formation, ff: fast formation). High-magnitude slopes, corresponding to fd and ff phases, diminish due to inhibition of CME. (C) SD of clathrin growth rate distributions are shown for the ventral and dorsal surfaces of four BSC1 cells before and after MBCD treatment. (D) Growth rate distributions are assembled using AP2 traces detected in SUM159 cells under different conditions (top;  $N_{\text{cells}} = 4$ ). With application of hypotonic shock (Dai et al., 1998; Diz-Muñoz et al., 2016), CME slows down due to increasing in-plane tension. Deoxycholate treatment reduces membrane tension (Raucher and Sheetz, 1999; Batchelder et al., 2011) and results in increased clathrin coat dynamics. The distributions are also displayed using five bins corresponding to distinct growth phases (bottom). (E) Temporal change in the SD of clathrin coat growth rates is plotted for two SUM159 cells. The dashed line marks the application of hypotonic shock or deoxycholate.

### 4.3.1 Clathrin coat dynamics in spreading and migrating cells

Membrane tension reduces gradually during cell spreading (Gauthier et al., 2009).

Changes in the SD of growth rates in both ventral and dorsal surfaces demonstrate that clathrin coat dynamics increase across the entire cell (Figure 4.2 D and G). We also found that initiation and dissolution densities of clathrin-coated structures increase significantly with the completion of spreading (Figure 4.2 E and F).

**Figure 4.2: Clathrin coat dynamics reflect changing membrane tension throughout cell spreading.**



(A) Optically trapped beads are used to measure membrane tether forces of BSC1 cells at early and late stages of spreading. Membrane tension values (mean + standard error) are shown for cells plated for 10 and 120 min ( $N_{\text{cells}} = 12$ ). (B) Snapshots show spreading of a BSC1 cell expressing AP2-EGFP. Detected clathrin coat traces are colored according to the lifetime. (C) Time variations of the average clathrin coat lifetime (orange) and visible spreading area (black) of the cell in B. SD of growth rates (D), and initiation and dissolution densities of clathrin coats (E) are plotted for the same cell. Shortening of lifetimes, increasing SD of growth rates, and increased initiation and dissolution rates establish increased endocytosis rates with the completion of spreading. (F) Box plots show the cumulative comparison of the clathrin coat lifetime and initiation/dissolution densities obtained during and after spreading of BSC1 cells ( $N_{\text{cells}} = 24$ ,  $N_{\text{traces}} = 41,989$ ).

Continued

## Figure 4.2: Continued

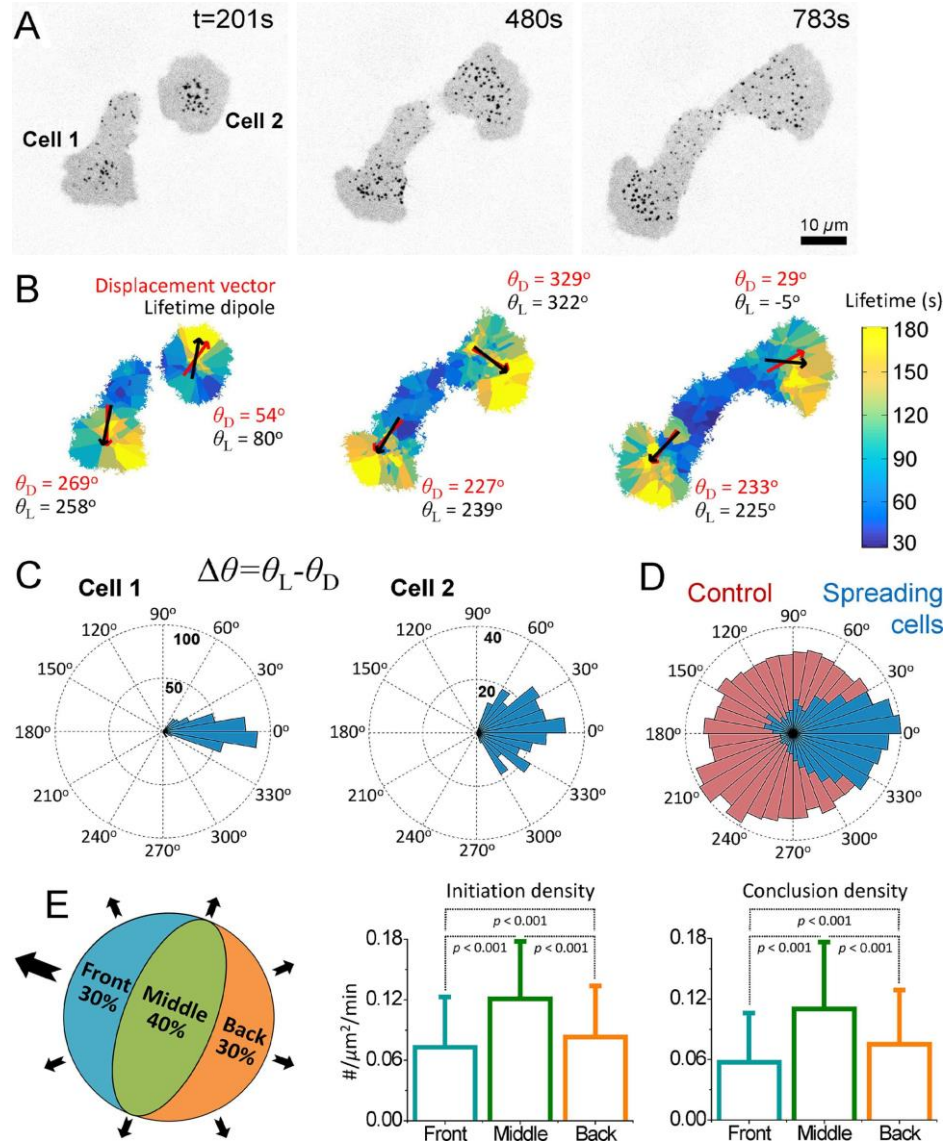
(G) SD of growth rates are calculated for the ventral and dorsal surfaces of BSC1 cells at early and late stages of spreading (measurements are separated by 30–40 min;  $N_{\text{cells}} = 11$ ). Boxes extend to the quartiles, with a line at the median. Whiskers extend from the 10th to 90th percentiles. (H) The plot shows the normalized clathrin coat lifetime ( $\text{mean} \pm \text{SD}$ ) vs. normalized extension rate of the ventral surface (area/time) obtained from 24 spreading cells. (I) Spreading area (blue) and average clathrin coat lifetime (orange) in cells featuring periods of spreading (shaded green regions) as well as retraction or pause. p values were obtained using the two-tailed t test.

Extension of the cell surface area is associated with increasing membrane tension (Gauthier et al., 2011; Houk et al., 2012; Masters et al., 2013). In good agreement with this observation, we detected a strong correlation between the rate of area extension and average clathrin coat lifetime in spreading cells (Pearson's  $r = 0.67$ ; Figure 4.2 H). This phenomenon is particularly conspicuous in cells that undergo multiple rounds of extension. When spreading is interrupted temporarily, clathrin coat lifetimes converge to the values observed during low-tension phases. Lifetimes elongate back to the values observed under high tension as soon as the cells start to spread again (Figure 4.2 I). Together, our findings show that temporal variations in tension have direct effects on dynamics and distribution of endocytic clathrin coats in cells.

Polarization of cells induces spatial heterogeneity in effective membrane tension (Dai and Sheetz, 1999; Lieber et al., 2015). Theoretical studies predict a strong front-to-rear tension gradient at the ventral surface of protruding cells (Fogelson and Mogilner, 2014). We found that the spatial heterogeneity in clathrin coat dynamics outlines the predicted tension gradient at the ventral surface of asymmetrically spreading cells (Figure

4.3). Figure 4.3 B shows clathrin lifetime maps of two spreading cells in which every data point is given the average value of the closest three clathrin coats' lifetime. We found that long-lived clathrin-coated structures are predominantly located near the leading edge. To better quantify this trend, for each time point of spreading, we calculated the lifetime dipole moment, which is a vector pointing in the direction of increasing clathrin coat lifetime. We detected a significant correlation between the direction of the lifetime dipole and the cells' center-of-mass displacement even when cells change directions (Pearson's  $r = 0.53$ ; Figure 4.3 B–D). As a control, we randomly exchanged the lifetime values between clathrin coats and recalculated the dipoles. The rose diagrams generated using the angular separation between the simulated lifetime dipoles and cells' original displacement directions were omnidirectional, indicating that the control analyses had no preference for the correct direction (Figure 4.3 D). We also found that clathrin coat distribution is significantly heterogeneous even when the net cellular displacement is due to slight asymmetry of the spreading. Initiation and dissolution densities are the lowest within cellular regions with the highest extension rate (Figure 4.3 E).

**Figure 4.3: Heterogeneous clathrin dynamics maps the tension gradient in protruding cells.**



(A) Snapshots show two asymmetrically spreading BSC1 cells expressing AP2-EGFP. (B) Lifetime maps of the cells in A. This representation allows analyzing the local lifetime and density information by the color and size of the domains, respectively, that is, the domain sizes are inversely related to the local density of clathrin coats. The clathrin coat lifetime dipole moments are shown by black vectors for each cell. The displacement directions of the cellular centers of mass for the given frames are shown by red vectors.  $\theta_L$  and  $\theta_D$  represent the angles of the lifetime dipoles and displacement vectors, respectively. (C) Rose plots are assembled using the angular separation between the lifetime dipole vectors and the displacement vectors ( $\Delta\theta = \theta_L - \theta_D$ ) for the two spreading cells in A and B.

Continued

### Figure 4.3: Continued

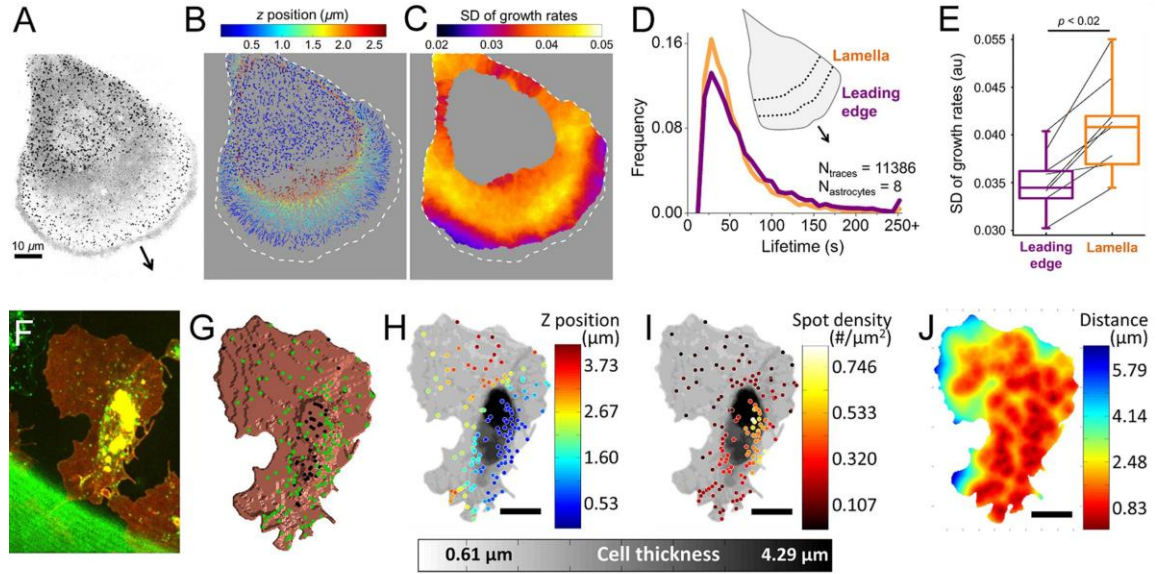
(D) The blue angular histogram shows  $\Delta\Theta$  values obtained from 15 spreading cells (total spreading time is 123 min). The red histogram shows the cumulative result of five simulations (using the same 15 cells) in which  $\Theta_L$  values are determined after clathrin coat lifetimes are randomly exchanged within a cell. (E) Asymmetrically spreading cells are sectioned into three regions (front: 30% of the cell area next to the leading edge; back: 30% of the cell area at the opposite side of the leading edge; middle: the remaining 40% of the cell area in between the front and back regions) in each frame of spreading movies. Both the front and back are extending regions. However, initiation and conclusion densities (shown as bar plots; mean + SD) are the lowest at the front region, which has the highest extension rate. p values were obtained using the two-tailed t test.

Tether force measurements revealed a significant front-to-rear tension gradient at the lamellipodial fragments of migrating keratocytes (Lieber et al., 2015). Such fragments cannot be isolated from migrating astrocytes for tension measurements. However, at the dorsal surface of these cells, we detected significant spatial heterogeneity in CME dynamics accompanying the expected tension gradient. Clathrin coats originating in the proximity of the leading edge have longer lifetimes ( $69 \pm 51$  s [leading edge] vs.  $58 \pm 39$  s [lamella],  $p < 0.001$ ; Figure 4.4 D) and narrower growth rate distributions ( $0.035 \pm 0.003$  [leading edge] vs.  $0.041 \pm 0.005$  [lamella],  $p < 0.02$ ; Figure 4.4 E). As a visualization tool for the spatial distribution of the clathrin dynamics, we generated growth rate maps in which each pixel is given the value of the SD of the growth rates detected in a circular neighborhood. In this representation, regions of the cell that have slower clathrin dynamics have smaller SD values (Figure 4.4 C). A comparative analysis of clathrin coat initiation and dissolution densities at the two regions is infeasible due to the complex three-dimensional (3D) geometries of the membrane ruffles appearing at the



leading edge (Kural et al., 2015). Collectively, our results demonstrate that the cellular processes associated with spatial divergences in plasma membrane tension increase the heterogeneity of CME in cells.

**Figure 4.4: Heterogeneous CME during in vitro and in vivo cell migration.**



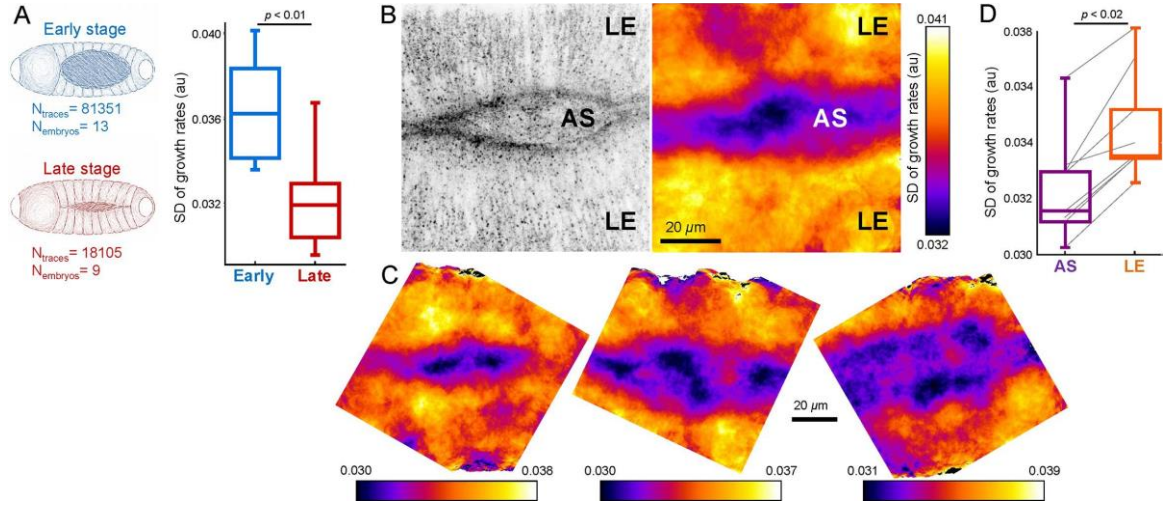
(A) Maximum z-projection image shows clathrin-coated structures at the ventral and dorsal surfaces of an U373 astrocyte expressing AP2-GFP. The arrow points toward the direction of extension. (B) Clathrin coat traces obtained from the cell in A are color-coded according to their z-position relative to the substrate. (C) Growth rate map of the dorsal surface is created by calculating the SD of clathrin growth rates within a 4.8- $\mu\text{m}$  radius. SD values are lower in the vicinity of the leading edge due to slower clathrin dynamics. Dashed lines represent the cell boundary. (D) Normalized distributions show lifetimes of dorsal clathrin coats positioned within an 8- $\mu\text{m}$  neighborhood of the leading edge (indigo) and the dorsal coats positioned in the lamellar region between 8 and 16  $\mu\text{m}$  from the leading edge (orange). (E) Box plots show the SD of growth rate distributions assembled using the leading edge and lamellar clathrin coat populations from eight astrocytes ( $N_{\text{traces}} = 11,386$ ). Connected lines indicate the values obtained from the same astrocyte. The narrower distribution obtained for the leading edge group (indigo) indicates slower clathrin dynamics at this region. Boxes extend to the quartiles, with a line at the median. Whiskers extend from the 10th to 90th percentiles.  $p$  value was obtained using the two-tailed  $t$  test. (F) Hemocytes expressing clathrin-GFP (green) and CD4-tdTomato (red) are imaged at the ventral surface of late *Drosophila* embryos. (G) CD4 signal is used to generate a 3D mask representing the surface of the hemocyte. Positions of the clathrin coats within 320-nm neighborhood of the surface are shown with green dots. (H, I) Grayscale represents the thickness of the hemocyte. Endocytic clathrin coats are color coded according to their z-positions in H and local density of clathrin spots calculated within a 5- $\mu\text{m}$  cube in I. (J) Each pixel in the hemocyte image is color coded according to its average distance to the three closest clathrin coats. Scale bars in H–J are 8  $\mu\text{m}$ .

### 4.3.2 Spatiotemporal variations in clathrin dynamics of *Drosophila* embryos

We expect spatiotemporal heterogeneity in clathrin coat dynamics to be prominent during developmental processes associated with dynamic tissue mechanics. It was previously shown that tension-based regulation of receptor endocytosis has important functions in development of *Drosophila* embryos (Pouille et al., 2009). Since quantification of clathrin lifetimes is error-prone within tissue contexts, we used growth rates and spatial distributions of clathrin-coated structures to probe CME in this system (Ferguson et al., 2016). During late stages of *Drosophila* embryogenesis, hemocytes migrate along the ventral nerve cord to populate the entire embryo. Unlike *in vitro* migration systems, embryonic hemocytes are physically constrained by the 3D environment and therefore do not form membrane ruffles at their lamellipodial extensions (Tucker et al., 2011). Figure 4.4 F shows the maximum z-projection image of a hemocyte expressing fluorescently tagged clathrin and the membrane marker CD4. We assessed the 3D positions of clathrin structures to distinguish the endocytic coats, which are in the vicinity of the cell surface (Figure 4.4 G and H) (Kural et al., 2012), and used alternative visualization tools to analyze the spatial distribution of endocytic clathrin coats. In Figure 4.4 I, positions of endocytic clathrin coats are color coded according to the density of neighboring coats within the 5- $\mu$ m neighborhood. In Figure 4.4 J, the heat map shows each pixel's average distance to the three closest clathrin coats.

During dorsal closure of the *Drosophila* embryo, tension on the amnioserosa (AS) tissue increases and the tissue volume reduces gradually (Ma et al., 2009; Saias et al., 2015). As expected, we detected significant reduction in clathrin dynamics at later stages of the dorsal closure (SD:  $0.036 \pm 0.003$  [early] vs.  $0.032 \pm 0.002$  [late],  $p < 0.01$ ; Figure 4.5 A). Using SD maps, we also discovered that CME dynamics is spatially heterogeneous at the dorsal surface of the embryo (Figure 4.5 B and D). Growth rate analysis revealed that clathrin dynamics are markedly slower at the AS compared with the two flanks of the lateral epidermis (LE) tissue (SD:  $0.032 \pm 0.002$  [AS] vs.  $0.035 \pm 0.002$  [LE],  $p < 0.02$ ; Figure 4.5 C). Such a divergence in endocytic dynamics was anticipated, considering the distinct physical properties of AS and LE cells and the mechanical roles they play during dorsal closure (Brodland et al., 2014; Ducuing and Vincent, 2016; Pasakarnis et al., 2016).

**Figure 4.5: Spatiotemporal variations in clathrin dynamics can be detected within tissues of *Drosophila* embryo.**



(A) Clathrin dynamics slow down with increasing tension during late stages of the dorsal closure. Box plots show the SD of clathrin growth rate distributions obtained from early and late stage AS tissues. Reduced SD is a hallmark of slowed-down endocytosis (Ferguson et al., 2016). (B) Left, clathrin-coated structures at the dorsal surface of a *Drosophila* embryo. AS appears as narrow opening between the two flanks of lateral epidermis (LE). Right, SD map of the clathrin growth rates obtained from the same area. The map is created by calculating the SD of apical clathrin growth rates within an 8- $\mu$ m radius. Lower SD values in the AS region display slower clathrin dynamics with respect to the neighboring LE. (C) More examples demonstrating the heterogeneous clathrin dynamics at the dorsal surface of late *Drosophila* embryos. (D) Box plots show the SD of clathrin growth rate distributions obtained from LE and AS of eight embryos. Connected lines indicate the values obtained from the same embryo. Boxes extend to the quartiles, with a line at the median. Whiskers extend from the 10th to 90th percentiles. p values were obtained using the two tailed t test.

## 4.4 Discussion

In this study, we have shown that spatial and temporal variations in cell membrane tension dominate the dynamics of clathrin-coated structures. Endocytic machinery must overcome the major constituents of the effective membrane tension--in-plane tension and membrane-cytoskeleton adhesion--to deform the plasma membrane (Sheetz, 2001). In-plane tension is assumed to be in equilibrium across the entire plasma membrane due to

fast flow of membrane lipids. However, membrane-cytoskeleton adhesion can be heterogeneous and induce stark differences in the clathrin dynamics between distinct surfaces of a cell (Dai and Sheetz, 1999; Boulant et al., 2011). Similarly, adhesion to the substrate can inhibit curvature formation and slow down clathrin coat dynamics locally. Therefore, non-uniform adhesion of a cell to the substrate creates another layer of heterogeneity in clathrin dynamics (Batchelder and Yarar, 2010; Ferguson et al., 2016).

We believe that spatiotemporal heterogeneity in clathrin coat dynamics plays important roles in central cellular processes. Mechano-inhibition of endocytosis at early stages of cell spreading might elevate the rate of extension of the plasma membrane area (Gauthier et al., 2009, 2011). Inhibition of endocytosis at the leading edge of migrating cells may facilitate cell protrusion by allowing net membrane deposition to this region (Bretscher, 2014). Similarly, increased tension at the amnioserosa tissue of developing embryos may account for the gradual reduction of the cell volume through inhibition of endocytosis in the late stages of the dorsal closure. Future studies should be directed toward investigating the mechano-regulation of endocytosis *in situ* and elucidating the roles it plays at the organismal level.

## 4.5 Materials and Methods

### 4.5.1 Cell culture and fluorescence microscopy

BSC1 and U373 cells stably expressing  $\sigma$ 2-EGFP were cultured in DMEM (Life Technologies) containing penicillin/streptomycin and 10% fetal bovine serum (FBS). Gene-edited SUM159 cells were grown in F-12 medium containing 5% FBS and 1  $\mu$ m/ml hydrocortisone (Aguet et al., 2016). Live cells and embryos were imaged using a Nikon Eclipse (TI-E) microscope equipped with a 100 $\times$  objective lens (Nikon CFI Plan-Apochromat Lambda, NA 1.45), a CSU-W1 spinning disk confocal head (Yokogawa Electric Corporation) and an electron-multiplying charge-coupled device (EMCCD) camera (iXon DU897 Ultra; Andor Technology). Sample temperature and z-position were stabilized using a temperature controlled chamber and perfect focusing system (PFS), respectively. NIS Elements software was used for image acquisition.

Spreading cells were imaged on glass bottom dishes (Greiner Bio-One) directly after plating. The plating time prior to astrocyte migration experiments was 8–24 h. Live cell imaging is performed at 37°C ambient temperature within L15 (Thermo Fisher Scientific) supplemented with 10% FBS. Images were acquired at 0.25–0.5 Hz, and laser exposure lasted for 50–300 ms per frame. The final concentrations of M $\beta$ CD and deoxycholic acid (Sigma-Aldrich) were 10 and 0.4 mM in serum-free L15, respectively. Hypotonic shock was performed using 1:5 dilution of the imaging medium using

deionized water. In the figures and movies, fluorescence acquisitions are inverted to increase visibility.

#### **4.5.2 Fly strains and in vivo imaging**

We used the UAS/GAL4 system to monitor clathrin dynamics in *Drosophila* embryos. Arm-GAL4, CLC-GFP, and CD4-tdTom strains were provided by the Bloomington *Drosophila* Stock Center. srpHemo-GAL4 was a gift from Norbert Perrimon (Harvard Medical School). Embryos were collected and aged for 11–13 h at 25°C. After dechoriation, embryos were mounted on coverslips and immersed in halocarbon oil. Clathrin dynamics at the dorsal and ventral surfaces were imaged at 22°C using 3D time-lapse acquisitions. In amnioserosa, apical clathrin coats were identified by filtering out the bright puncta corresponding to organelle-bound clathrin-coated structures as described earlier (Ferguson et al., 2016). In Figure 4.5 A, maximum amnioserosa openings for the early- and late-stage embryos were  $81.5 \pm 13.0$  and  $28.2 \pm 10.6$   $\mu\text{m}$ , respectively.

To analyze hemocyte images, clathrin coats were found using a simple threshold of the clathrin channel and localized using the center of intensity of the fluorescence signal (Kural et al., 2012). Similarly, the membrane was identified using a threshold on the CD4 channel. Using the built-in MATLAB function, `isosurface`, a triangular mesh of the membrane surface was generated. Clathrin coats were defined to be endocytic if they



were  $< 320$  nm from the nearest surface voxel. The spot density was determined by counting all endocytic coats around a spot within a 5- $\mu$ m cube and then dividing that by the sum of the area from the triangulated mesh found within the cube. The distance map was generated by determining the average distance of the three closest endocytic clathrin spots for each pixel on the surface.

#### **4.5.3 Two-dimensional tracking of clathrin-coated structures**

We used cmeAnalysis software for 2D single particle tracking (Aguet et al., 2013). We used a previously developed trace rejection scheme to filter traces that do not follow a characteristic clathrin coat intensity profile (Ferguson et al., 2016). We used the traces that pass the rejection scheme in the calculation of lifetime distributions, growth rate distributions, initiation/dissolution densities and lifetime dipoles.

To determine the temporal evolution of the average clathrin coat lifetime, for each frame of a movie, we added together the lifetime of each trace that exists in that frame and divided by the number of traces considered.

#### **4.5.4 Three-dimensional tracking of clathrin-coated structures**

We used the z-position information to distinguish the dorsal and ventral clathrin coats in cells (Figures 4.1 C, 4.2 G, and 4.4 B). cmeAnalysis software was used to analyze each z-plane of 3D time-lapse movies (followed by the trace rejection scheme detailed above).

The resulting data were combined to link traces which occur at the same lateral position in two adjacent z-planes. Coincident traces had to remain within one pixel (160 nm) x-y distance for at least three frames. The resulting trace was assigned the maximum intensity value among all traces considered for combination. Axial positions were calculated using the intensity-weighted mean z-position of all traces considered. The algorithm for trace combination ran from the outermost z-planes to the innermost, alternating between the top and the bottom to ensure that there was no directional bias and all possible trace combinations were considered.

#### **4.5.5 Growth rate distributions**

Clathrin coat intensity traces were normalized by subtracting a global minimum and dividing by the resulting maximum. From this normalized trace, each 12-s interval was used in a least-squares fit to determine the growth rate of each interval. A trace had to be at least 12 s long to be included in the distribution. An arbitrary bin width (0.03) was found to delineate five distinct growth phases (fast dissolution, slow dissolution, plateau, slow formation, and fast formation) (Ferguson et al., 2016).

To determine the SD of the growth rates per frame, we generated a list of the intensity slope of each trace within that frame and took the SD of that list. When the data are sparse, we used the walking average of three adjacent frames. We used PFS to eliminate sample defocusing triggered by the squeezing procedure. We found that the

adjustment of the PFS resulted in a single frame of artificial growth rate values due to abrupt changes in the clathrin coat fluorescence intensities. Those frames are excluded from the analyses.

SD maps of clathrin coat growth rates in Figures 4.4 and 4.5 are made by, for each pixel within the cell, calculating the SD of all growth rates within 4.8 and 8  $\mu\text{m}$ , respectively.

#### **4.5.6 Lifetime maps and dipole vectors**

Lifetime maps in Figure 4.3 are made of a given frame by calculating the average lifetime of the three closest clathrin-coated structures for each pixel within the cell. Patches of color are regions where the set of closest clathrin coats are the same, so color is an indication of local lifetime and the size of the patch is an indication of local clathrin coat density (larger patches indicate lower density).

Lifetime dipoles were calculated using the equation:  $\sum_{i=1}^N (T_i - \bar{T}) r_i$ , where  $T_i$  and  $r_i$  are the lifetime and the position of the  $i$ th clathrin-coated structure and  $\bar{T}$  is the average lifetime of all clathrin-coated structures in the frame. Abortive clathrin coats with lifetimes less than 20 s, hotspots, and clathrin-coated plaques that do not disappear until the end of the acquisitions were excluded from the calculation of lifetime dipoles. In the randomization scheme used for the control analyses, the positions of clathrin-coated structures remained untouched to validate that the reciprocity between the lifetime dipole and cell displacement is due only to the spatial distribution of lifetimes within the cell.

#### 4.5.7 Tether force measurements

We used optically trapped beads to quantify membrane tether forces. An optical tweezers system was built based on a previous design; however, only one of the two traps was used in this application (Bustamante et al., 2009). Polystyrene beads (1  $\mu\text{m}$ ; Spherotech) were coated with fibronectin (Sigma-Aldrich) before the experiments. Cells were incubated for 10 min or 2 h before the experiments for measuring membrane tension at different stages of spreading. Membrane tension values ( $T$ ) are calculated using  $T = F_T^2 / 8\pi^2 B$ , where  $F_T$  is the measured membrane tether forces and  $B$  is the bending modulus of the plasma membrane, and the value is assumed to be 0.27 pN  $\mu\text{m}$  (Hochmuth et al., 1996).

## **Chapter 5 *In Vitro* Characterization of CALM recruitment to clathrin coated structures**

Derived from a manuscript in preparation by: Huber, S., Smith, A., Kural, C., and Cocucci, E.

*In this chapter, my contributions were all experiments and analyses except gene editing of the cells and the quantification thereof with western blot.*

### **5.1 Abstract**

We characterized the dynamics of CALM recruitment to clathrin-coated structures in gene-edited SUM CALM-eGFP cells, which allowed us to study CALM recruitment dynamics for the first time without CALM overexpression and the problems therein. We found that cells with 60% reduced CALM expression function normally in ideal conditions, but struggle to internalize vesicles when membrane tension is elevated. This suggests that the curvature driving ability of CALM is only necessary under conditions where curvature formation is impeded. We also compared the super-resolved localization of CALM to that of AP2 using TIRF-SIM and find that CALM localizes to small puncta within larger AP2-coated structures, suggesting that the curvature sensing ability of

CALM causes it to have strong preference for curved sections of the large, mostly flat clathrin plaques.

## 5.2 Introduction

Clathrin-mediated endocytosis (CME) is an essential process in all mammalian cells that is responsible for the uptake of extracellular proteins and receptors (Conner and Schmid, 2003). The most prevalent protein in CME and namesake for the process, clathrin, can self-assemble into a round cage (Crowther et al., 1975). This provides some of the energy necessary to bend the initially flat plasma membrane into a round clathrin-coated pit (CCP), which can then pinch off from the surrounding membrane. However, clathrin by itself cannot bind to the membrane, so it can only form empty cages in the absence of accessory proteins.

Aside from clathrin, the two most prevalent CME proteins, AP2 and CALM, can simultaneously bind to clathrin and membrane lipids, which allows them to act as clathrin-membrane adaptors (Borner et al. 2012; Popova et al., 2013). Using overexpression of clathrin-GFP and AP2-GFP, the recruitment dynamics of clathrin and AP2 were studied *in vitro* as early as 1999 and 2003, respectively (Gaidarov et al., 1999; Wu et al., 2003). Unfortunately, overexpression of CALM inhibits CME by sequestration of clathrin, so CALM could not be studied in the same way (Tebar et al., 1999).

Despite this problem, CALM could be still be studied by indirect means such as depletion experiments. CALM depletion results in larger, more irregular clathrin-coated structures (CCSs) (Meyerholz et al., 2005), as well as an increase in abortive clathrin structures and longer lifetimes of productive pits (Mettlen et al., 2009). CALM-depleted mice are dwarfed in size and have severe anemia (Suzuki et al., 2012). Additionally, abnormal CALM has been linked to Alzheimer's disease (Harold et al., 2010), and CALM was shown to partially suppress amyloid beta peptide toxicity in yeast (Treusch et al., 2011).

Only recently have CALM recruitment dynamics been studied *in vitro* (Miller et al., 2015). In that study, it was found that CALM functions in curvature generation as a curvature sensor and inducer. Along with their important biochemical characterization of CALM, Miller et al. also briefly described the *in vitro* recruitment of CALM, and found that it followed AP2 recruitment very closely except during a short window shortly before scission. In another recent *in vitro* study, it was found that CALM intensity profiles more closely correlate with curvature appearance in pits than that of AP2 or clathrin (Scott et al., 2018).

In this study, we seek to further test the *in vitro* recruitment dynamics of CALM to clathrin-coated structures using a cell line that we gene-edited to express CALM-eGFP at endogenous levels, thereby avoiding the problems associated with CALM overexpression.

## 5.3 Results

### 5.3.1 Characterization of the numbers of proteins recruited to clathrin-coated pits

The first quantity we wished to characterize in these cells was the number of each protein recruited to pits by the time of scission. To convert intensity values to absolute numbers of proteins we calculated the approximate substitution ratio through western blot and the intensity of single eGFPs through photobleaching analysis of free eGFP as in Cocucci et al. (2012).

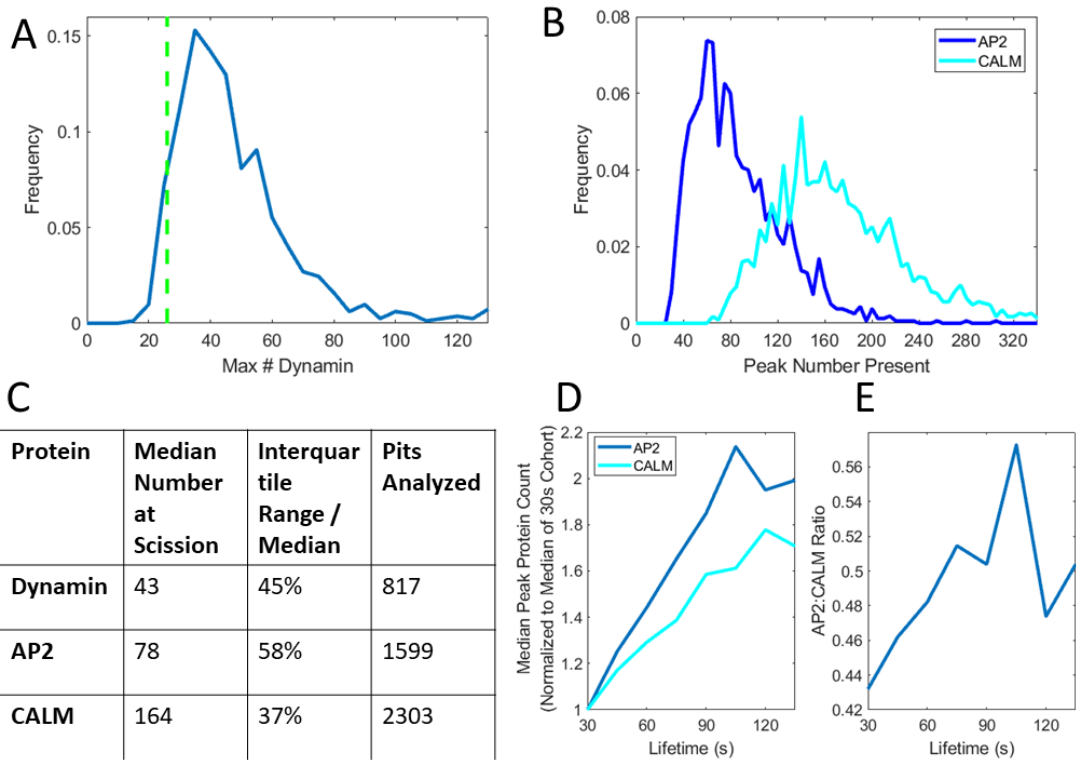
We first characterized the recruitment numbers of our Dynamin-eGFP cells to compare to the results of Cocucci et al. (2014). We used *cmeAnalysis* package for automated detection of dynamin-containing structures (Aguet et al., 2013), along with our previously described selection code for recognizing full traces (Ferguson et al., 2016). We then plotted the calibrated distribution of dynamin peak intensities as in Cocucci et al. (2014). The resulting distribution was in very good agreement with the previous result (Fig. 5.1 A).

We then calculated the calibrated peak intensity distribution of our AP2-eGFP and CALM-eGFP cells (Fig. 5.1 B). We found that the median number of CALM and AP2 proteins was similar, but the variance in CALM intensities between different pits was much less than that of AP2. In order to compare AP2 and CALM numbers of similar pits, we grouped our traces into lifetime cohorts and compared the median AP2 and



CALM numbers of corresponding cohorts. We saw that AP2 recruitment number increases more drastically with lifetime (Fig. 5.1 D, E). This suggests that large pits need fewer CALM molecules per AP2 to internalize when compared to small pits.

**Figure 5. 1: Calibrated Intensity Results**



(A) Histogram of peak number of dynamin molecules recruited at scission. (B) Histogram of peak number of AP2 and CALM proteins recruited at scission. (C) Summary statistics of the distributions in A and B. (D) Median peak AP2 and CALM count for pits in different lifetime cohorts. (E) Median AP2:CALM ratio for the cohorts in D.

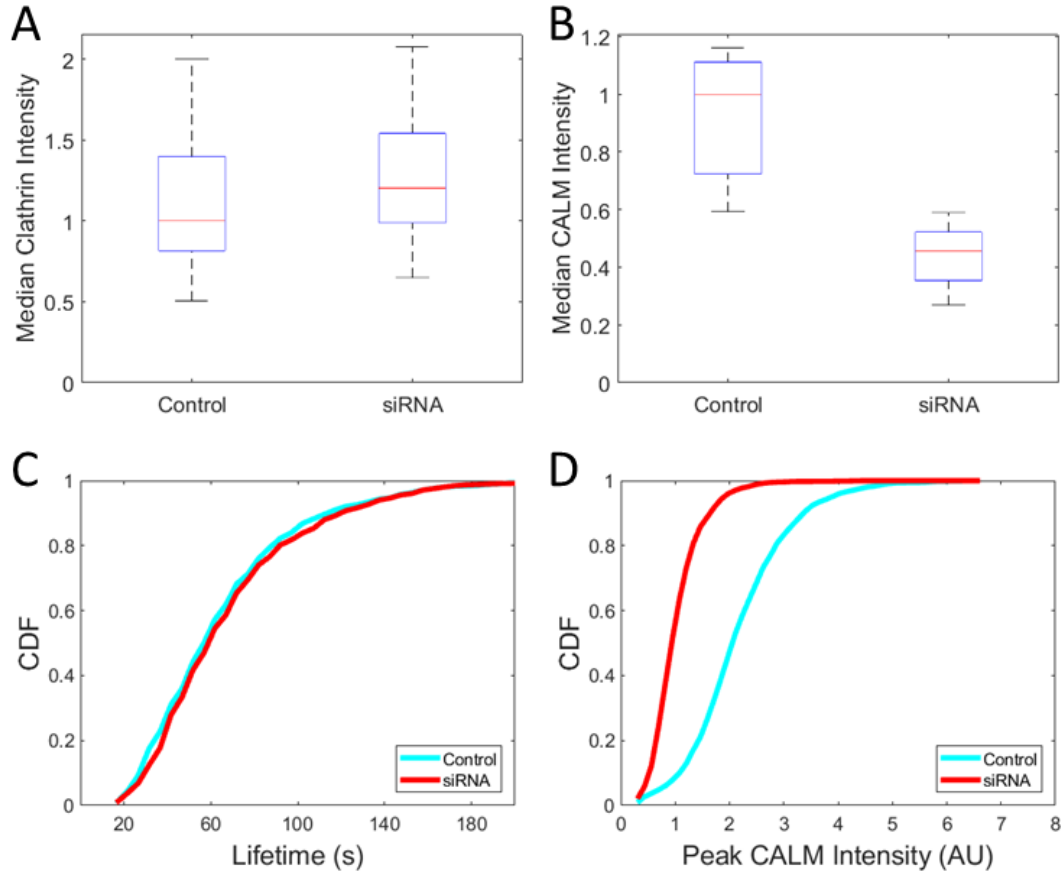
### 5.3.2 Clathrin coated pit dynamics in CALM siRNA cells

Next, we quantified the effects of lowered CALM expression on clathrin dynamics. To do so, we transiently transfected our cells with CALM siRNA to partially block CALM

expression. In order to avoid potential bias caused by tracking puncta labelled by CALM-eGFP, we simultaneously transfected our cells with CLCa-ruby to use as a marker for CCS tracking. We also transfected a control group of cells with the CLCa-ruby plasmid in the same way without CALM siRNA.

We compared the clathrin and CALM signal between the control and siRNA cells (Fig. 5.2 A,B). As expected, the clathrin signal in the control cells was on average the same as the clathrin signal in the siRNA cells. The CALM signal in the siRNA cells was roughly 60% lower than that of the control cells, confirming the efficacy of the siRNA. Dynamically, the control and siRNA cells were very similar; the medians of the lifetime distributions differed by only 2 seconds, despite the fact that the siRNA pits recruited far less CALM by the time of scission (Fig. 5.2 C,D). This suggests that, under ideal conditions, pits can function normally with 60% reduced CALM expression.

**Figure 5.2: Effects of 60% CALM reduction**

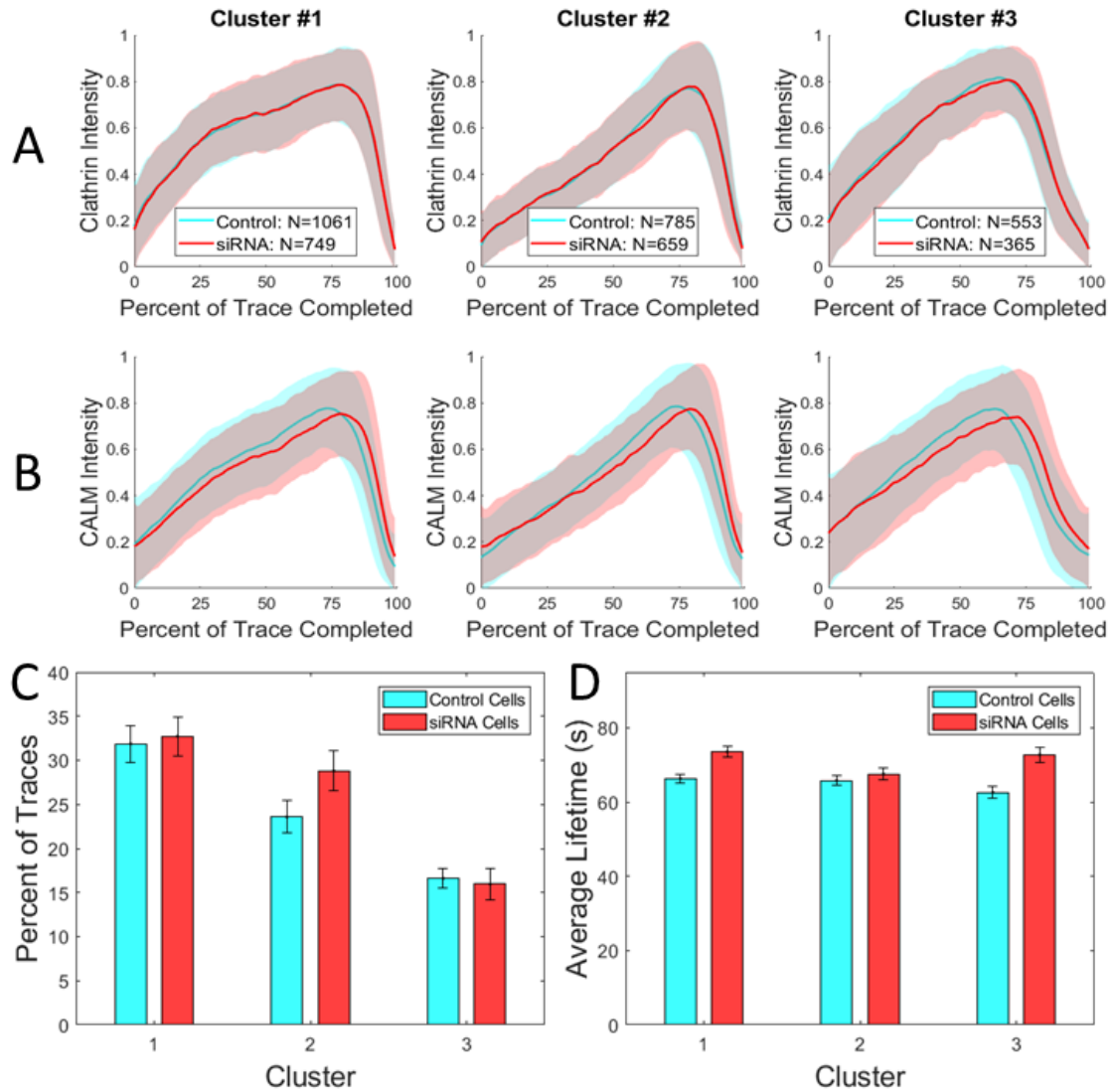


(A), (B) Boxplots of the median clathrin and CALM intensity of puncta for each cell in the control and CALM siRNA groups ( $N_{\text{control}}=15$ ,  $N_{\text{siRNA}}=13$ ). (C) Cumulative distribution function of lifetimes of pits for control and CALM siRNA groups ( $N_{\text{control}}=2399$ ,  $N_{\text{siRNA}}=1773$ ). (D) Cumulative distribution function of peak CALM intensities of pits for control and CALM siRNA groups

To probe the recruitment dynamics of the siRNA cells further, we used our previously described hierarchical trace-clustering algorithm to separate clathrin intensity traces of single clathrin-coated pits by shape (Ferguson et al., 2016). We found three highly populated clusters: cluster 1 had highly plateaued recruitment, cluster 2 had linear

recruitment, and cluster 3 had recruitment in between 1 and 2 (Fig. 5.3 A). The average clathrin traces of these clusters looked very similar between control and siRNA cells; however, the average CALM traces of the siRNA cells showed CALM recruitment that peaked about 10% later in the pits' lifetimes than that of the control cells (Fig. 5.3 B). Additionally, we found that the siRNA traces had a slightly higher tendency towards cluster 2 (Fig 5.3 C), suggesting that the scarcity of CALM causes an increased probability of linear pit growth. Lastly, we found that the average lifetime of each cluster was somewhat higher in the siRNA cells (Fig. 5.3 D). In summary, we found that cells with 60% reduced CALM expression can function normally, aside from small changes in CALM recruitment and lifetime.

Figure 5. 3: Comparing Trace Clusters between Control and siRNA Conditions



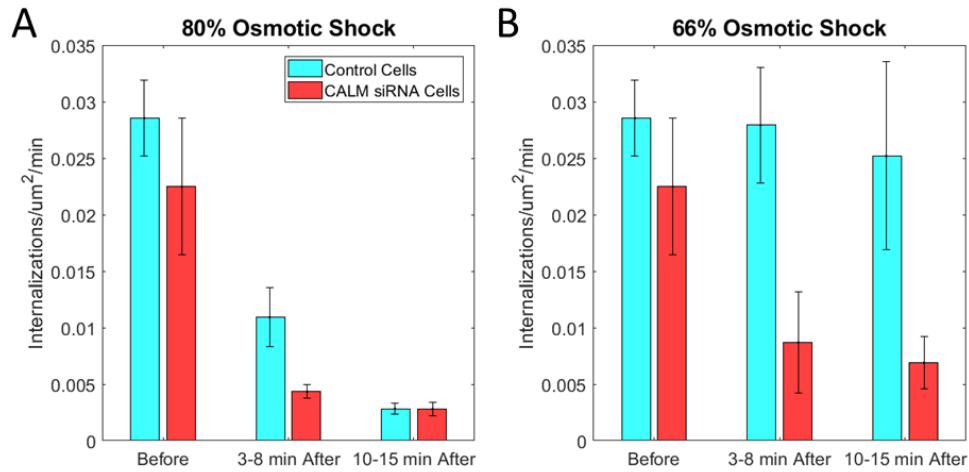
(A) Average clathrin intensity profiles of pits from control and siRNA cells of the three most populated clusters of clathrin traces when the traces were normalized in intensity and lifetime and hierarchically clustered. The shaded regions are the standard deviation of each timepoint in the average trace. (B) Average CALM intensity profiles of the clathrin clusters from A. (C) Percent of traces in each group that fall into each of the three clusters from A. Error bars represent standard error of the mean by cell (D) Average lifetime of traces from each cluster from A. Error bars represent standard error of the mean by cell

### **5.3.3 Clathrin coated pit dynamics in CALM siRNA expressing cells subject to elevated membrane tension**

CALM has been previously found to help in the generation of membrane curvature in clathrin-coated pits (Miller et al., 2015). Additionally, we have previously found that an increase in membrane tension decreases the internalization rate of pits, likely due to the additional energy required to curve the membrane (Ferguson et al., 2017). Combining these two findings, we hypothesized that cells with lowered CALM expression would be more strongly affected by increased membrane tension, as measured by pit internalization rate. To test this, we subjected our control and CALM siRNA cells to osmotic shock, which transiently elevates membrane tension (Ferguson et al., 2017).

We first subjected our cells to an osmotic shock that lowered the osmolarity of the medium by 80%. Under this very strong shock, we found that the dynamics of all cells were almost completely stalled after 10 minutes (Fig. 5.4 A). In the 10 minutes immediately after the addition of water to the medium, though, we saw a significantly higher internalization rate in our control cells compared to that of our CALM siRNA cells (Fig. 5.4 A, middle two bars). This suggests that while the cells were swelling, they were temporarily in a state where the membrane tension was too high for siRNA cells to internalize pits, but not so high as to completely halt the dynamics of the control cells.

**Figure 5. 4: Internalization Rates under Osmotic Shock**



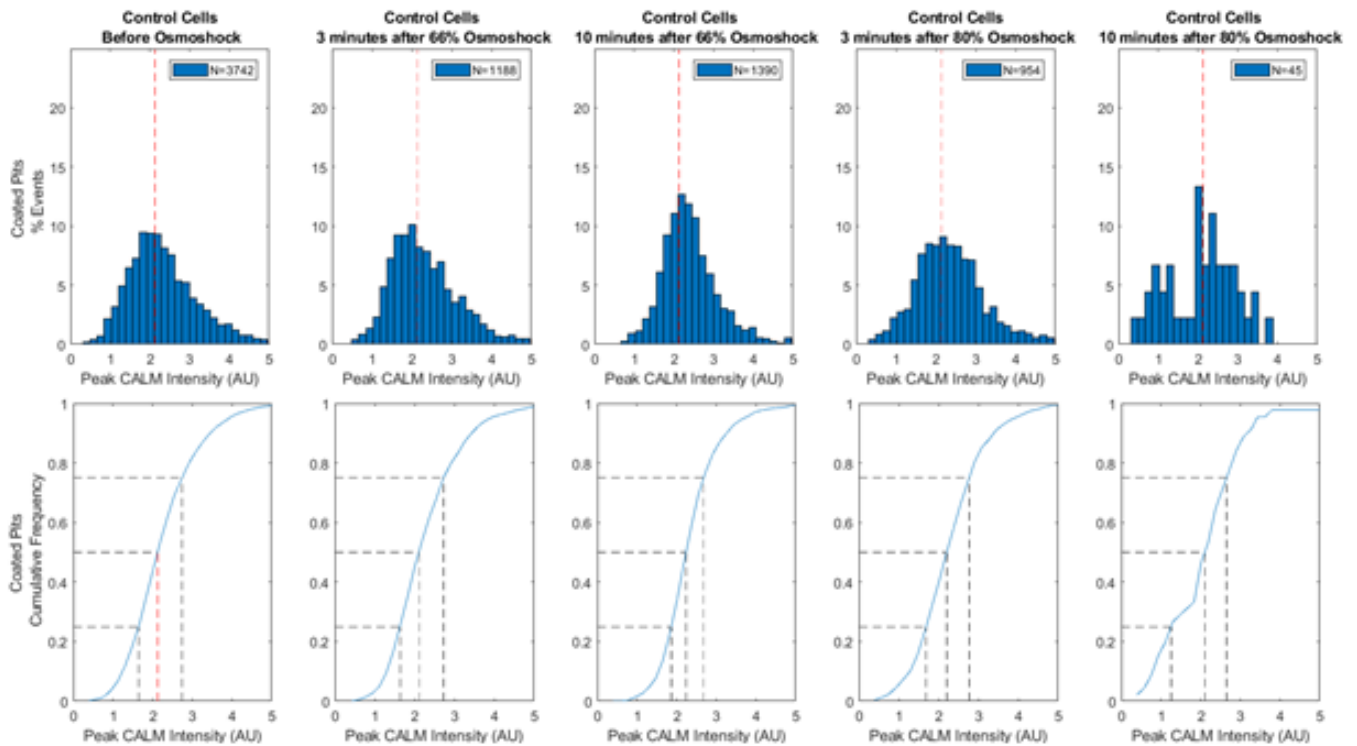
(A) Average number of internalizations per square micron per minute for control and CALM siRNA cells subjected to medium suddenly shocked to a final concentration of 80% water (Number of cells in each group from left to right: 18, 15, 13, 13, 13, 12). (B) Average number of internalizations per square micron per minute for cells subjected to medium suddenly shocked to a final concentration of 66% water (Number of cells in each group from left to right: 18, 15, 5, 6, 5, 6).

We then tried to replicate this intermediate-tension state by subjecting our cells to a weaker osmotic shock of 66% water. In this condition, the internalization rate of the control cells was not significantly affected, even after 10 minutes, while the internalization rate of the siRNA cells was reduced by roughly 2/3 (Fig. 5.4 B). This provided further evidence that cells with reduced CALM expression have reduced CME efficiency under elevated membrane tension.

Additionally of interest was the effect osmotic shock had on the CALM content of pits at scission. We hypothesized that the minimum number of CALM molecules needed to successfully complete a pit would increase when tension increased. In actuality, we

saw that the distribution of peak CALM intensities was always very wide with no apparent change in minimum (Fig. 5.5 and 5.6). There was a change in the median of these distributions under osmotic shock, however: We found that the median peak CALM intensity of pits in our siRNA cells increased markedly after 10 minutes of either 66% or 80% shock (Fig. 5.6). Interestingly, the median did not change in the first 10 minutes of the shock, suggesting that some delayed mechanism causes pits to start

**Figure 5. 5: CALM Present at Scission under Hypotonic Shock in Control Cells**

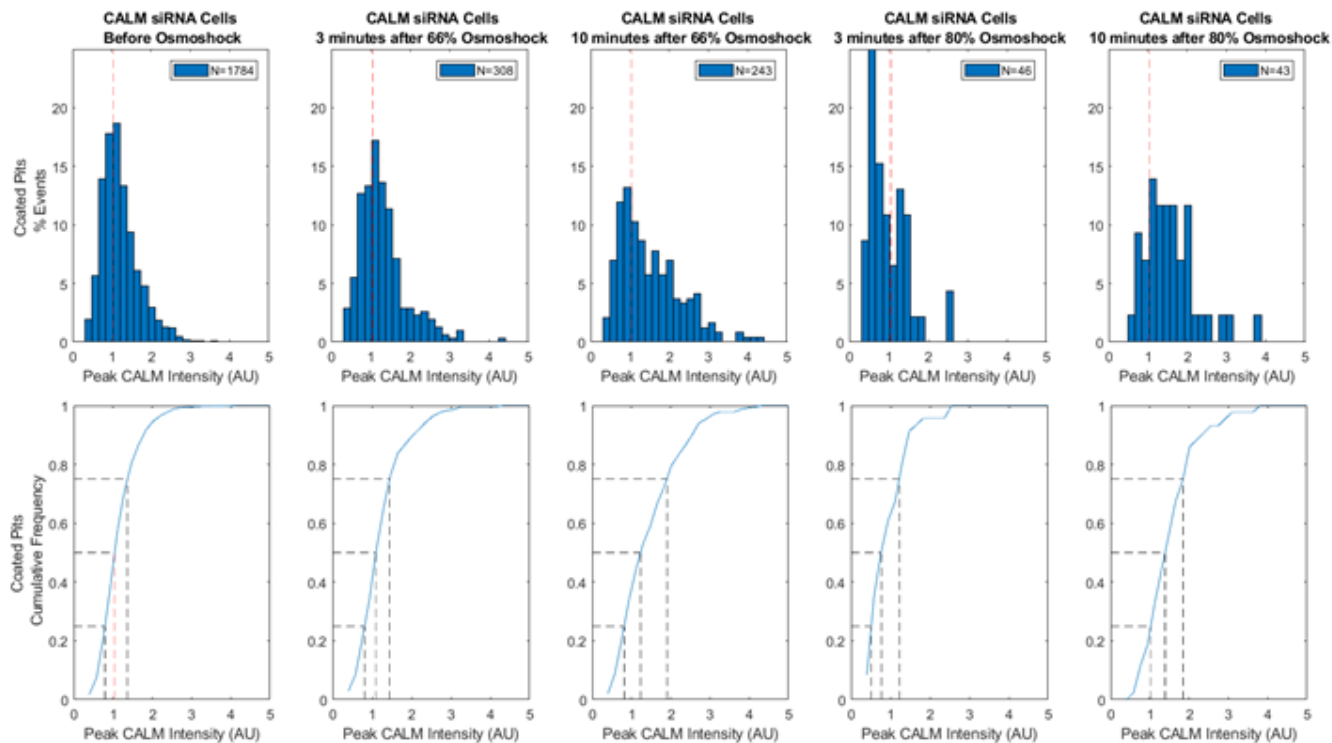


accumulating more CALM to oppose tension.

Histograms (top) and Cumulative distribution functions (bottom) of productive pits in control cells under our different osmotic conditions. Dashed lines in the CDFs denote quartiles, and the dashed red line in the histograms denotes the median of the control pre-osmotic shock distribution



**Figure 5. 6: CALM Present at Scission under Hypotonic Shock in CALM siRNA Cells**



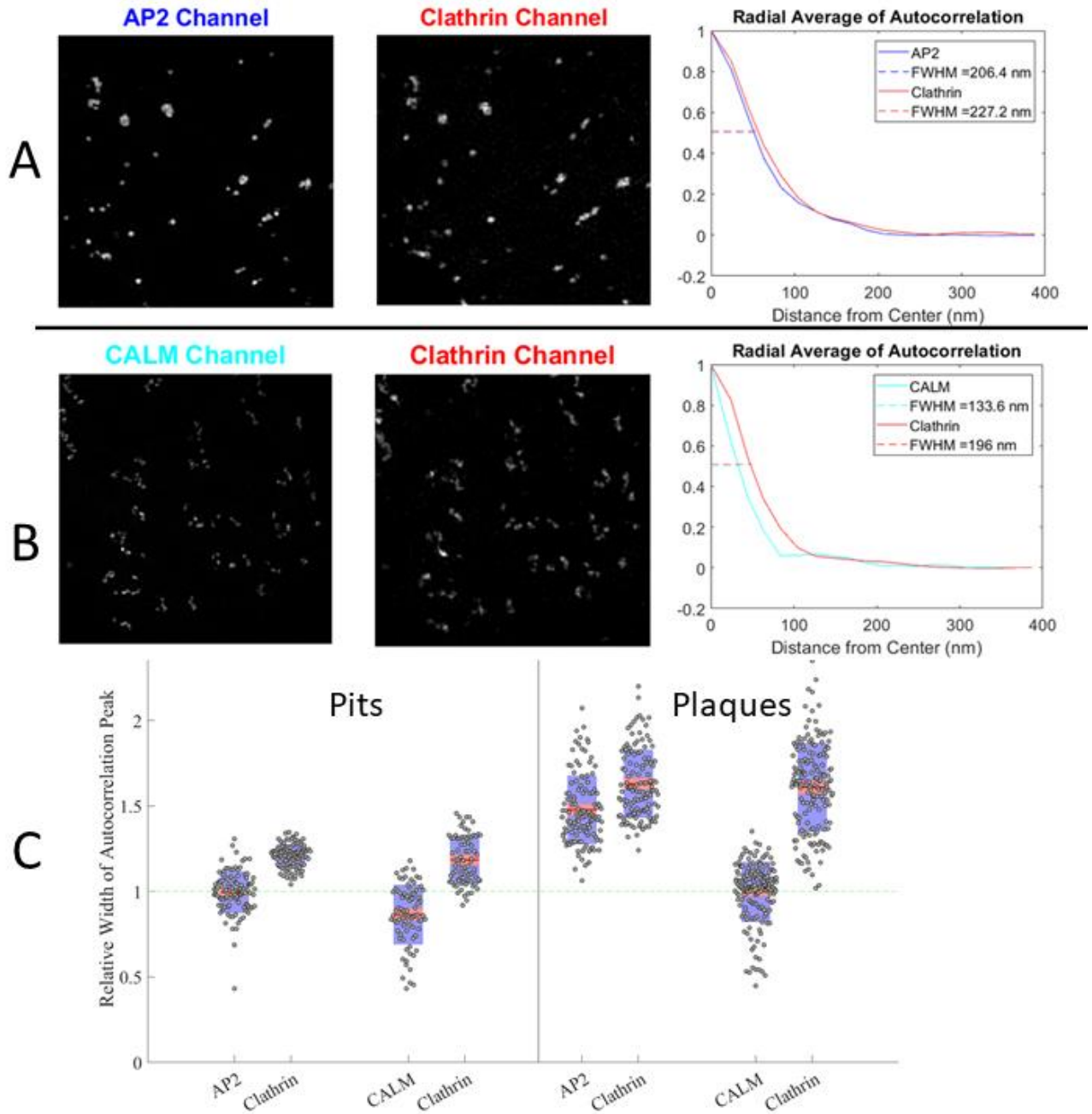
Histograms (top) and Cumulative distribution functions (bottom) of productive pits in control cells under our different osmotic conditions. Dashed lines in the CDFs denote quartiles, and the dashed red line in the histograms denotes the median of the control pre-osmotic shock distribution

### 5.3.4 Super-resolved localization of CALM in large, clathrin-coated structures using TIRF-SIM

TIRF-SIM is a super-resolution imaging technique that combines the low cytosolic background of Total Internal Fluorescence Microscopy (TIRF) with the sub-diffraction resolution of Structured Illumination Microscopy (SIM) (Chung et al., 2006). To further characterize these gene-edited CALM-eGFP cells, we ran 2-color TIRF-SIM on our

CALM-eGFP cells overexpressing clathrin light chain A-ruby. Upon inspection of the images, it seemed as though large structures seen in the clathrin channel appeared as collections of closely spaced small structures in the CALM channel (Fig. 5.7 B). To assess the possibility of this being an artifact of the naturally better resolution of the shorter wavelength CALM channel, we repeated these experiments on similarly gene-edited SUM AP2-eGFP cells, also overexpressing clathrin light chain A-ruby. In these cells, large structures in the clathrin channel appeared as similarly large structures in the AP2 channel (Fig 5.6 A) indicating that the localization of AP2 in large structures does indeed differ from that of CALM.

Figure 5.7: Autocorrelation Analysis of TIRF-SIM Images



(A) (left 2 panels) Example AP2/Clathrin 2-color field of view. (right panel) Radial average of the autocorrelation image of the images. Dashed lines show the full width at half max of the peaks. (B) (left 2 panels) Example CALM/Clathrin 2-color field of view. (right panel) Radial average of the autocorrelation

image of the images. Dashed lines show the full width at half max of the peaks. (C) Boxplots of the full width at half max of manually selected pits and plaques in each channel. Widths were normalized to the median full width at half max of the pits in the AP2 channel (green dashed line).

To quantify this effect, we used image autocorrelation analysis on areas of interest with the large structures we wished to probe. The center of the autocorrelation image of a series of objects is a global maximum that decays with a width that roughly corresponds to  $\sqrt{2}$  times the average width of the objects (Robertson and George, 2012). With that in mind, we calculated the radial average of the center of the autocorrelation image, and examined width of the resulting peaks. We consistently found that the full width at half max of CALM autocorrelation images was much smaller than that of their corresponding clathrin images, while the full width at half max of AP2 autocorrelation images was only marginally smaller than that of their clathrin images (Fig. 5.7 A, B right panel). This however did not hold for areas of interest containing only small clathrin coated structures.

To quantify this final assertion, we manually selected 467 total clathrin structures among the two cell types and classified them as either “pits” (a single Gaussian-shaped object that internalizes in one step), or “plaques” (large, non-Gaussian-shaped objects). We then ran our autocorrelation width analysis on the small regions containing each single object. In pits, both AP2 and CALM are spread across similarly sized regions, as evidenced by their autocorrelation widths (Fig. 5.7 C left panel). However, in plaques, AP2 is spread over a region that is roughly 40% wider than that of CALM (Fig. 5.7 C right panel). Furthermore, the median CALM autocorrelation width in plaques is very

similar to that of pits, suggesting that CALM may localize to small, pit-sized regions of plaques.

## **5.4 Discussion**

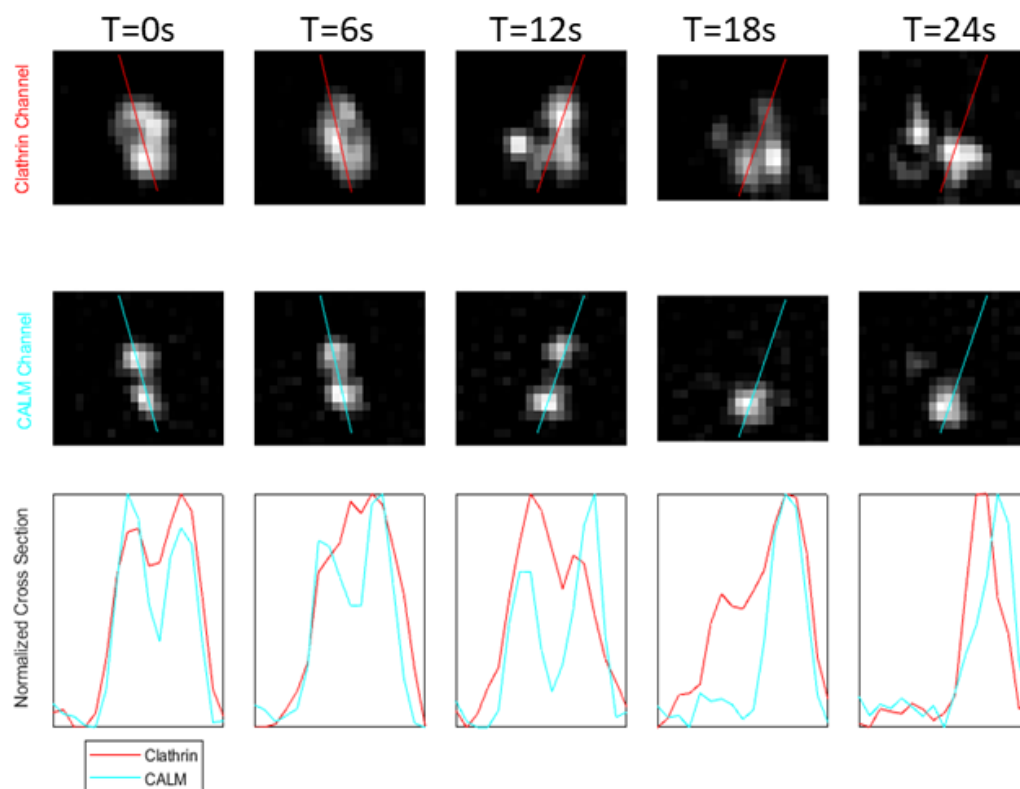
In this work, we characterized the recruitment of CALM to clathrin-coated pits using gene-edited SUM CALM-eGFP cells. We quantified the number of CALM molecules present in pits at scission and the localization of CALM in large, clathrin-coated structures. We also analyzed the dynamic changes caused by reducing CALM expression by 60% in isotonic as well as hypotonic conditions.

We found that CALM is present in CCPs in similar numbers to that of AP2 and dynamin, but with less variation in values from pit to pit. If the main functions of CALM are curvature sensing and generation as hypothesized by Miller et al. (2015), this may be due to the fact that larger vesicles have membranes that are less strongly curved, thus reducing the CALM needed per unit area of membrane.

Our finding that the amount of CALM in CCPs at the time of scission increases only after 10 minutes of hypo-osmotic shock is interesting because it suggests a compensatory mechanism with which CALM is deployed to act against elevated membrane tension. It also suggests an approximate time of 10 minutes for this mechanism to take effect.

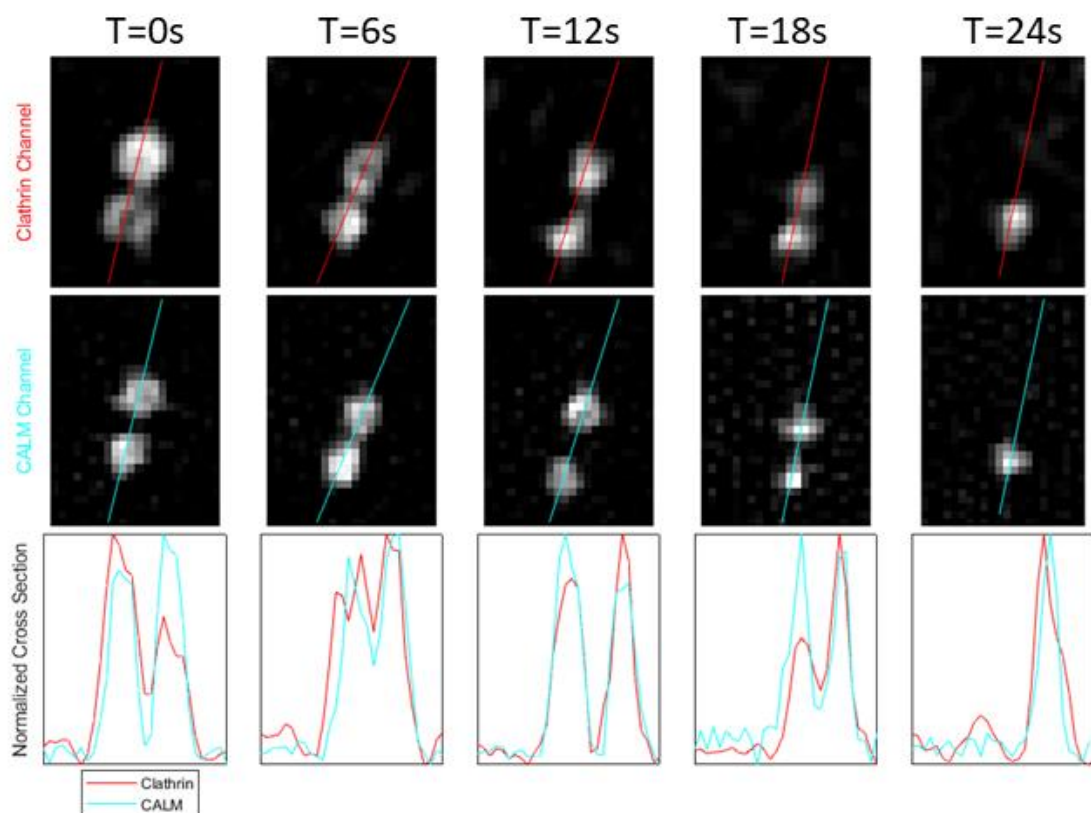
Our finding that CALM may localize to small, pit-sized regions of clathrin-coated plaques may be related to the fact that CALM has been shown to be a sensor and driver of membrane curvature (Miller et al., 2015). It has been previously suggested that the edges of flat clathrin-coated plaques may be able to gain curvature and eventually pinch off into vesicles (den Otter et al., 2011). Indeed, EM images often show large, clathrin-coated objects with heterogeneous curvature profiles (Heuser, 1989). Additionally, polarized TIRF measurements of pit curvature have been shown to correlate with CALM intensity of individual pits (Scott et al., 2018). We hypothesize that the pit-sized regions we see CALM in are curved sections of plaques, which attract more CALM than the adjacent flat sections. In support of this idea, we have documented instances of these regions quickly leaving the field of view, as if that section of the plaque were internalized (Fig. 5.8 and 5.9).

Figure 5.8: Example of Plaque Internalization Event



Clathrin (top) and CALM (middle) frames of a plaque internalization event. (bottom) Cross-sectional profile for both channels.

**Figure 5.9: Example of the Internalization of One of Two Nearby Pits**



Clathrin (top) and CALM (middle) frames of a pit internalization event nearby to another pit. (bottom) Cross-sectional profile for both channels.

## 5.5 Materials and Methods

### 5.5.1 Cell culture

SUM159 cells gene edited to express AP2-eGFP (Aguet et al., 2016) (gift of Tomas Kirchhausen, Departments of Cell Biology and Pediatrics, Harvard Medical School Boston, MA), as well as our cells gene edited to express CALM-eGFP were grown in F-



12 medium containing 5% fetal bovine serum (FBS), penicillin-streptomycin and hydrocortisone.

### **5.5.2 Fluorescence Imaging**

The imaging system for all but the TIRF-SIM section was an Eclipse TI-E microscope (Nikon) equipped with a temperature controlled chamber, a CSU-W1 spinning disk confocal unit (Yokogawa Electric Corporation), a 100× objective lens (Nikon CFI Plan-Apochromat Lambda, NA 1.45) and an EMCCD camera (iXon DU897 Ultra; Andor Technology). Image acquisition was done using NIS Elements software. All confocal movies were 5 minutes long, taken at .5 frames per seconds with 100 ms exposure time per channel.

To calculate the intensity of a single eGFP, we imaged a slide of sparse, free eGFP molecules with a long exposure time, and calculated the intensity change during single steps of photobleaching as in Cocucci et al. (2012).

TIRF-SIM imaging was performed at the Advanced Imaging Center (AIC) of the Janelia Research Campus. This system uses an inverted microscope (Axio Observer; ZEISS), and a sCMOS camera (ORCA-Flash4.0; Hamamatsu), with a 1.49-NA 100x objective lens (Olympus Life Science, CA, USA). Structured illumination was achieved as described in Li et al. (2015).

### **5.5.3 Image Detection and Tracking**

Tracking was done using the cmeAnalysis MATLAB package (Aguet et al., 2013). The output traces were then filtered using our previously described trace-rejection algorithm (Ferguson et al., 2016). All 2-channel tracking was done only using data from the 560 nm (clathrin) channel in order to not introduce bias to siRNA cells with lower 488 (CALM) signal. Intensity in both channels was then calculated using the pixel-sum scheme described above.

### **5.5.4 Single GFP Intensity Calibration**

Free eGFP was plated onto coverslips. These slides were then imaged with 4 s exposure per frame for 2-5 minutes. The resulting movies were then tracked and instances of step-like bleaching events were manually selected. Intensity of puncta was calculated as the mean intensity of a 5x5 pixel window around the puncta minus a background value calculated as the median intensity of the 24 pixels immediately surrounding the signal window.

### **5.5.5 Object Dissolution Verification**

We developed an algorithm for screening all clathrin fluorescent traces for true scission events. The goal thereof was to create a set of criteria that identified most events while strictly avoiding false positives, so that quantities of CALM at scission could be

measured. Briefly, this algorithm scanned all traces for spans of fast, linear intensity decrease that ended with a sufficiently dim time-point. A maximum displacement per frame was also imposed to preclude tracking errors. This algorithm was tuned and checked using the below described manual analysis software. In situations of especially low scission rates where a few false positives could be problematic, manual verification was used.

#### **5.5.6 Autocorrelation Analysis**

A MATLAB function was previously developed to facilitate manual pit and plaque selection (Ferguson et al., 2018). This was used to select suitable structures for 2-channel autocorrelation analysis from the clathrin channel of our movies. Some areas that were in-focus in the clathrin channel appeared out-of-focus in the adaptor channel, so a cross-correlation minimum of .5 was imposed to filter out these structures.

Manually selected and cropped 2-channel TIRF-SIM structures were aligned using the maximum of the cross-correlation of the images. Autocorrelation images were then made using MATLAB built-in “xcorr2”.

## **Chapter 6 Conclusions and Future Work**

In this thesis, we have described several techniques developed to characterize further the process of clathrin-mediated endocytosis. We developed growth rate analysis to improve the time resolution of our measurements. We adapted hierarchical clustering analysis to study different recruitment shapes. We applied autocorrelation image analysis to super-resolved images to quantify the differences in localization of different proteins.

We used these techniques to quantify the precise effect that membrane tension has on CME. We found that an increase in membrane tension slows the protein recruitment and scission of clathrin-coated pits. This effect allowed us to make indirect observations about the relation between membrane tension and other processes with much higher spatial and temporal resolution than could be achieved with the state-of-the-art direct tension measurement techniques. We also found that the clathrin adaptor protein CALM is important for the internalization of clathrin-coated pits under increased membrane tension, but is not important under normal tension conditions. This fact is interesting given the cellular investment in the protein represented by its high copy number.

There is still much work to be done with these techniques. We spent Chapter 5 characterizing the dynamics of cellular recruitment of CALM, but there are many other

CME proteins that could be studied in the same way. One such protein is dynamin, which accumulates in a ring around the neck of a completing CCPs and contracts to induce scission (Cocucci et al., 2014). Two-color analysis of dynamin and clathrin is of interest because dynamin is one of the best markers for scission in CME. This data could be used to study the poorly-understood CCP subpopulation termed “abortives” (Aguet et al., 2013). These structures aggregate clathrin similarly to normal pits, but dissolve before they can internalize cargo. Therefore, they disappear without a scission-related spike of dynamin. Dual-color microscopy of AP2 and dynamin would allow us to assess the effect of membrane tension on the abortive subpopulation.

The most direct scission signature is the division of endocytic cargo from the external environment. A “pH cycling” technique has been developed to identify this signature (Taylor et al., 2011). Briefly, an endocytic cargo receptor is labelled with a fluorescent marker that only fluoresces at a specific pH. The environmental pH is then cyclically changed so that the receptors flash on and off. When scission occurs, the internalized receptors are isolated from the cycling pH, which can be identified by the receptors not flashing. An implementation of this technique could also allow us to identify vesicle scission events while allowing us to quantify the amount of receptors internalized by each event.

Several of our techniques were developed to work around the fact that our pit tracking software is not perfect. Our current implementation of our tracking software

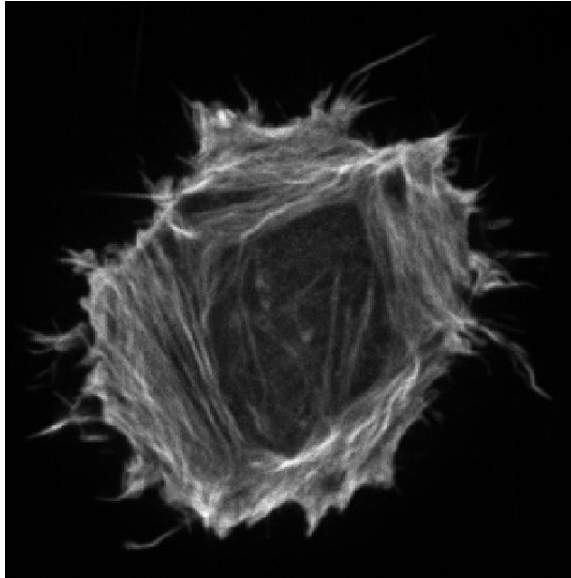
verifies the accuracy of traces by looking for linear sections of recruitment and dissolution, but this is far from flawless. One potential use for the AP2/dynamin or pH cycling data described above would be to generate a labelled dataset of traces where the authenticity of each trace is verified by a definitive signature of scission. This dataset could then be used to optimize and test an improved trace verification scheme.

Many different approaches could be applied to the problem of trace verification. One of our current most promising options is the previously described hierarchical clustering algorithm: All clathrin intensity traces could be input into this algorithm and then traces in clusters shaped like canonical pits could be considered “true” pits. We used this technique briefly in Chapter 5, but it has significant room for optimization and should be rigorously checked for consistency on different cell types.

Another potentially interesting pair of proteins to study using two-color microscopy is clathrin and actin. Actin is a very common protein used in cellular force generation and is instrumental in allowing clathrin-coated pits to invaginate against elevated membrane tension (Boulant et al., 2011). We briefly explored the link between actin and tension in Chapter 3, but there are still many questions left to be answered. We do not know under what exact circumstances actin is required to overcome membrane tension, or where exactly the actin is recruited on the pit. It may also be interesting to observe the action of the actin cytoskeleton during spreading and migration, and how it

affects CME. If nothing else, this analysis would be interesting because fluorescence images of actin look beautiful (Fig. 6.1).

**Figure 6. 1: Fluorescence image of the actin cytoskeleton**



The question of actin localization in CME will require super-resolution techniques to answer because clathrin-coated pits are smaller than the diffraction limit. We did some work on super-resolved TIRF-SIM images in Chapter 5, but that was done outside our lab. Achieving super-resolution in our lab, although expensive, would open many possible research paths that are currently out of our reach. With super-resolution imaging, we could work on many open problems including the localization of actin in clathrin-coated structures and the possibility of parts of flat, clathrin-coated plaques budding into vesicles.

To achieve the best possible resolving power we would need to use an electron microscope (EM). Building such a system is certainly out of our financial reach, but there are facilities on the Ohio State campus that will soon be capable of cryoTEM imaging. The biggest difficulty with us using this technique is that sample preparation through freeze-etching is experimentally difficult and requires specialized equipment (Heuser, 2014). As our work concerns the dynamics of CME, and EM can only be done on fixed samples, this technique may not be directly applicable to our research. Still, having access to EM could prove invaluable as a way to visualize fine details of clathrin-coated structures.

Another useful, albeit more mundane, potential project would be to streamline our experimental data pipeline. We currently manually interface with several programs between the time of microscope use and the completion of our tracking software. The development of a combined user interface could save many hours of effort. This would also reduce the computational skill required of lab members, allowing for more specialization in experimental skills.

The techniques described in this thesis provide several different approaches to the analysis of clathrin-mediated endocytosis. While research in this field is still in the stage of trying to complete a basic understanding of the process, the ubiquity of CME in mammalian cells suggests that this knowledge will someday be useful for medical purposes. Specifically, the application of our knowledge of CME to Alzheimer's disease



seems promising. As was mentioned in chapter 5, abnormal CALM has been linked to Alzheimer's disease in multiple studies (Harold et al., 2010; Treusch et al., 2011). Additionally, a recent study suggests that the increased risk of Alzheimer's disease in the elderly stems from the fact that endocytosis is upregulated in that population (Alsaqati et al., 2017). Perhaps our knowledge of clathrin-mediated endocytosis will one day help us fight this terrible disease.

## Bibliography

Aegerter-Wilmsen, T., Heimlicher, M.B., Smith, A.C., de Reuille, P.B., Smith, R.S., Aegerter, C.M., and Basler, K. (2012). Integrating force-sensing and signaling pathways in a model for the regulation of wing imaginal disc size. *Development* 139, 3221–3231.

Aghamohammadzadeh, S., and Ayscough, K.R. (2009). Differential requirements for actin during yeast and mammalian endocytosis. *Nat. Cell Biol.* 11, 1039–1042.

Aguet, F., Antonescu, C.N., Mettlen, M., Schmid, S.L., and Danuser, G. (2013). Advances in analysis of low signal-to-noise images link dynamin and AP2 to the functions of an endocytic checkpoint. *Dev. Cell* 26, 279–291.

Aguet, F., Upadhyayula, S., Gaudin, R., Chou, Y., Cocucci, E., He, K., Chen, B.-C., Mosaliganti, K., Pasham, M., Skillern, W., et al. (2016). Membrane dynamics of dividing cells imaged by lattice light-sheet microscopy. *Mol. Biol. Cell* 27, 3418–3435.

Alsaqati, M., Thomas, R. S., & Kidd, E. J. (2017). Proteins Involved in Endocytosis Are Upregulated by Ageing in the Normal Human Brain: Implications for the Development of Alzheimer’s Disease. *The Journals of Gerontology: Series A*, 73(3), 289-298.

Apodaca, G. (2002). Modulation of membrane traffic by mechanical stimuli. *Am. J. Physiol. Renal Physiol.* 282, F179–F190.

Ashkin, A. (1970). Acceleration and Trapping of Particles by Radiation Pressure. *Physical Review Letters*, 24(4), 156-159.

Avinoam, O., Schorb, M., Beese, C.J., Briggs, J.A.G., and Kaksonen, M. (2015). Endocytic sites mature by continuous bending and remodeling of the clathrin coat. *Science* (80-. ). 348, 1369–1372.

Batchelder, E.M., and Yarar, D. (2010). Differential Requirements for Clathrin-dependent Endocytosis at Sites of Cell–Substrate Adhesion. *Mol. Biol. Cell* 21, 3070–3079.

Batchelder, E.L., Hollopeter, G., Campillo, C., Mezanges, X., Jorgensen, E.M., Nassoy, P., Sens, P., and Plastino, J. (2011). Membrane tension regulates motility by controlling lamellipodium organization. *Proc. Natl. Acad. Sci.* 108, 11429–11434.

Berg-Sørensen, K., and Flyvbjerg, H. (2004). Power spectrum analysis for optical tweezers. *Review of Scientific Instruments*, 75(3), 594-612.

Bo, L., and Waugh, R. (1989). Determination of bilayer membrane bending stiffness by tether formation from giant, thin-walled vesicles. *Biophysical Journal*, 55(3), 509-517.

Borner, G. H. H., Antrobus, R., Hirst, J., Bhumbra, G. S., Kozik, P., Jackson, L. P., ... Robinson, M. S. (2012). Multivariate proteomic profiling identifies novel accessory proteins of coated vesicles. *The Journal of Cell Biology*, 197(1), 141–160.

Boucrot, E., Saffarian, S., Zhang, R., and Kirchhausen, T. (2010). Roles of AP-2 in clathrin-mediated endocytosis. *PLoS One* 5.

Boulant, S., Kural, C., Zeeh, J.-C., Ubelmann, F., and Kirchhausen, T. (2011). Actin dynamics counteract membrane tension during clathrin-mediated endocytosis. *Nat. Cell Biol.* 13, 1124–1131.

Bretscher, M.S. (2014). Asymmetry of Single Cells and Where That Leads. *Annu. Rev. Biochem.* 83, 275–289.

Brodland, G.W., Veldhuis, J.H., Kim, S., Perrone, M., Mashburn, D., and Hutson, M.S. (2014). CellFIT: A cellular force-inference toolkit using curvilinear cell boundaries. *PLoS One* 9.

Bustamante, C., Chemla, Y.R., Moffitt, J.R., Bustamante, C., Chemla, Y.R., and Moffitt, J.R. (2014). High-Resolution Dual-Trap Optical Tweezers with Differential Detection : Instrument Design High-Resolution Dual-Trap Optical Tweezers with Differential Detection : Instrument Design. 4, 1–9.

Byfield, F. J., Aranda-Espinoza, H., Romanenko, V. G., Rothblat, G. H., and Levitan, I. (2004). Cholesterol Depletion Increases Membrane Stiffness of Aortic Endothelial Cells. *Biophysical Journal*, 87(5), 3336-3343.

- Chung, E., Kim, D., and So P. T. (2006). Extended resolution wide-field optical imaging: objective-launched standing-wave total internal reflection fluorescence microscopy. *Opt. Lett.* 31, 945-947
- Cocucci, E., Aguet, F., Boulant, S., and Kirchhausen, T. (2012). The first five seconds in the life of a clathrin-coated pit. *Cell* 150, 495–507.
- Cocucci, E., Gaudin, R., and Kirchhausen, T. (2014). Dynamin recruitment and membrane scission at the neck of a clathrin-coated pit. *Mol. Biol. Cell* 25, 3595–3609.
- Collins, A., Warrington, A., Taylor, K.A., and Svitkina, T. (2011). Structural organization of the actin cytoskeleton at sites of clathrin-mediated endocytosis. *Curr. Biol.* 21, 1167–1175.
- Colom, A., Derivery, E., Soleimanpour, S., Tomba, C., Molin, M. D., Sakai, N., . . . Roux, A. (2018). A fluorescent membrane tension probe. *Nature Chemistry*, 10(11), 1118-1125.
- Conner, S.D., and Schmid, S.L. (2003). Regulated portals of entry into the cell. *Nature* 422, 37–44.
- Crick, F., and Hughes, A. (1950). The physical properties of cytoplasm. *Experimental Cell Research*, 1(1), 37-80.
- Crowther, R.A., Pinch, J.T., Pearse B.M.F. (1976). On the structure of coated vesicles. *Journal of Molecular Biology* 103 (4), 785-798
- Cureton, D.K., Massol, R.H., Whelan, S.P.J., and Kirchhausen, T. (2010). The length of vesicular stomatitis virus particles dictates a need for actin assembly during clathrin-dependent endocytosis. *PLoS Pathog.* 6.
- Dai, J., and Sheetz, M.P. (1995). Regulation of endocytosis, exocytosis, and shape by membrane tension. *Cold Spring Harb. Symp. Quant. Biol.* 60, 567–571.
- Dai, J., and Sheetz, M. P. (1997). Chapter 9 Cell Membrane Mechanics. *Methods in Cell Biology*, 157-171
- Dai, J., Sheetz, M.P., Wan, X., and Morris, C.E. (1998). Membrane tension in swelling and shrinking molluscan neurons. *J. Neurosci.* 18, 6681–6692.

- Dai, J., Ting-Beall, H.P., and Sheetz, M.P. (1997). The Secretion-coupled Endocytosis Correlates with Membrane Tension Changes in RBL 2H3 Cells. *J. Gen. Physiol.*
- Dai, J., and Sheetz, M.P. (1999). Membrane tether formation from blebbing cells. *Biophys. J.* 77, 3363–3370.
- den Otter, W.K., and Briels, W.J. (2011). The Generation of Curved Clathrin Coats from Flat Plaques. *Traffic* 12, 1407–1416.
- Desprat, N., Supatto, W., Pouille, P.A., Beaupaire, E., and Farge, E. (2008). Tissue Deformation Modulates Twist Expression to Determine Anterior Midgut Differentiation in *Drosophila* Embryos. *Dev. Cell* 15, 470–477.
- Diz-Muñoz, A., Krieg, M., Bergert, M., Ibarlucea-Benitez, I., Muller, D. J., Paluch, E., & Heisenberg, C. (2010). Control of Directed Cell Migration In Vivo by Membrane-to-Cortex Attachment. *PLoS Biology*, 8(11).
- Diz-Muñoz, A., Fletcher, D.A., and Weiner, O.D. (2013). Use the force: membrane tension as an organizer of cell shape and motility.
- Diz-Muñoz, A., Thurley, K., Chintamen, S., Altschuler, S.J., Wu, L.F., Fletcher, D.A., and Weiner, O.D. (2016). Membrane Tension Acts Through PLD2 and mTORC2 to Limit Actin Network Assembly During Neutrophil Migration. *PLoS Biol.* 14, 1–30.
- Ducuing, A., and Vincent, S. (2016). The actin cable is dispensable in directing dorsal closure dynamics but neutralizes mechanical stress to prevent scarring in the *Drosophila* embryo. *Nat. Cell Biol.* 18, 1149–1160.
- Ehrlich, M., Boll, W., van Oijen, A., Hariharan, R., Chandran, K., Nibert, M.L., and Kirchhausen, T. (2004). Endocytosis by Random Initiation and Stabilization of Clathrin-Coated Pits. *Cell* 118, 591–605.
- Ferguson, J.P., Willy, N.M., Heidotting, S.P., Huber, S.D., Webber, M.J., and Kural, C. (2016). Deciphering dynamics of clathrin-mediated endocytosis in a living organism. *J. Cell Biol.* 214, 347–358.
- Ferguson, J.P., Huber, S.D., Willy, N.M., Aygün, E., Goker, S., Atabey, T., and Kural, C. (2017). Mechanoregulation of clathrin-mediated endocytosis. *J. Cell Sci.* 130, 3631–3636.

Ferguson, JP, Cakez, C, Hasan, F, Chang, H, Li, D, Betzig, E, Cocucci, E, and Kural, C. (2018). Chapter 5 Curvature Generation by Endocytic Clathrin Coats. (In preparation)

Fiolka, R., Shao, L., Rego, E.H., Davidson, M.W., and Gustafsson, M.G.L. (2012). Time-lapse two-color 3D imaging of live cells with doubled resolution using structured illumination. *Proc. Natl. Acad. Sci.* 109, 5311–5315.

Fogelson, B., and Mogilner, A. (2014). Computational estimates of membrane flow and tension gradient in motile cells. *PLoS One* 9.

Gadkari, R. and Srinivasan, N. (2012). Protein-Protein Interactions in Clathrin Vesicular Assembly: Radial Distribution of Evolutionary Constraints in Interfaces. *PloS one*. 7. e31445. 10.1371/journal.pone.0031445.

Gaidarov, I., Santini, F., Warren, R.A., and Keen, J.H. (1999). Spatial control of coated-pit dynamics in living cells. *Nat Cell Biol* 1, 1–7.

Gauthier, N.C., Rossier, O.M., Mathur, A., Hone, J.C., and Sheetz, M.P. (2009). Plasma Membrane Area Increases with Spread Area by Exocytosis of a GPI-anchored Protein Compartment. *Mol. Biol. Cell* 20, 3261–3272.

Gauthier, N.C., Fardin, M.A., Roca-Cusachs, P., and Sheetz, M.P. (2011). Temporary increase in plasma membrane tension coordinates the activation of exocytosis and contraction during cell spreading. *Proc. Natl. Acad. Sci.* 108, 14467–14472.

Gauthier, N.C., Masters, T.A., and Sheetz, M.P. (2012). Mechanical feedback between membrane tension and dynamics. *Trends Cell Biol.* 22, 527–535.

Harold, D., Abraham, R., Hollingworth, P., Sims, R., Gerrish, A., Hamshere, M., . . . Williams, J. (2009). Genome-wide association study identifies variants at *CLU* and *PICALM* associated with Alzheimer's disease. *Nature Genetics* 41, 1088–1093

Hassinger, J.E., Oster, G., Drubin, D.G., and Rangamani, P. (2017). Design principles for robust vesiculation in clathrin-mediated endocytosis. *Proc. Natl. Acad. Sci. U. S. A.* 114, E1118–E1127.

Heimstädt, O. Das Fluoreszenzmikroskop. *Z. Wiss. Mikrosk.* 28, 330–337 (1911)

- Helfrich, W. (1973). Elastic Properties of Lipid Bilayers: Theory and Possible Experiments. *Zeitschrift Für Naturforschung C*, 28(11-12), 693-703.
- Herant, M., Heinrich, V., and Dembo, M. (2005). Mechanics of neutrophil phagocytosis: behavior of the cortical tension. *J. Cell Sci.* 118, 1789–1797.
- Heuser, J.E., Keen, J.H., Amende, L.M., Lippoldt, R.E., and Prasad, K. (1987). Deep-etch visualization of 27S clathrin: A tetrahedral tetramer. *J. Cell Biol.* 105, 1999–2009.
- Heuser, J. (1989). Effects of cytoplasmic acidification on clathrin lattice morphology. *J. Cell Biol.* 108, 401–411.
- Heuser, J. E. (2014). Some personal and historical notes on the utility of “deep-etch” electron microscopy for making cell structure/function correlations. *Molecular Biology of the Cell*, 25(21), 3273-3276.
- Hochmuth, R.M., and Waugh, R.E. (1987). Erythrocyte Membrane Elasticity And Viscosity. *Annual Review of Physiology*, 49(1), 209-219.
- Hochmuth, R.M., Shao, J.Y., Dai, J., and Sheetz, M.P. (1996). Deformation and flow of membrane into tethers extracted from neuronal growth cones. *Biophys. J.* 70, 358–369.
- Hong, S.H., Cortesio, C.L., and Drubin, D.G. (2015). Machine-Learning-Based Analysis in Genome-Edited Cells Reveals the Efficiency of Clathrin-Mediated Endocytosis. *Cell Rep.* 12, 2121–2130.
- Houk, A.R., Jilkine, A., Mejean, C.O., Boltyanskiy, R., Dufresne, E.R., Angenent, S.B., Altschuler, S.J., Wu, L.F., and Weiner, O.D. (2012). Membrane tension maintains cell polarity by confining signals to the leading edge during neutrophil migration. *Cell* 148, 175–188.
- Irajizad, E., Walani, N., Veatch, S. L., Liu, A. P., and Agrawal, A. (2017). Clathrin polymerization exhibits high mechano-geometric sensitivity. *Soft Matter*, 13(7), 1455-1462.
- Jacinto, A., Woolner, S., and Martin, P. (2002). Dynamic analysis of dorsal closure in *Drosophila*: From genetics to cell biology. *Dev. Cell* 3, 9–19.

Kaur, S., Fielding, A.B., Gassner, G., Carter, N.J., and Royle, S.J. (2014). An unmet actin requirement explains the mitotic inhibition of clathrin-mediated endocytosis. *Elife* 2014, 1–17.

Khatibzadeh, N., Gupta, S., Farrell, B., Brownell, W.E., and Anvari, B. (2012). Effects of cholesterol on nano-mechanical properties of the living cell plasma membrane. *Soft Matter* 8, 8350.

Kiehart, D.P., Galbraith, C.G., Edwards, K.A., Rickoll, W.L., and Montague, R.A. (2000). Multiple forces contribute to cell sheet morphogenesis for dorsal closure in *Drosophila*. *J. Cell Biol.* 149, 471–490.

Kirchhausen, T. (2009). Imaging endocytic clathrin structures in living cells. *Trends in Cell Biology*, 19(11), 596-605.

Kural, C., and Kirchhausen, T. (2012). Live-cell imaging of clathrin coats (Elsevier Inc.).

Kural, C., Tacheva-Grigorova, S.K., Boulant, S., Cocucci, E., Baust, T., Duarte, D., and Kirchhausen, T. (2012). Dynamics of Intracellular Clathrin/AP1- and Clathrin/AP3-Containing Carriers. *Cell Rep.* 2, 1111–1119.

Kural, C., Akatay, A.A., Gaudin, R., Chen, B.-C., Legant, W.R., Betzig, E., and Kirchhausen, T. (2015). Asymmetric formation of coated pits on dorsal and ventral surfaces at the leading edges of motile cells and on protrusions of immobile cells. *Mol. Biol. Cell* 26, 2044–2053.

Lee, Y.-C., Block, G., Chen, H., Folch-Puy, E., Foronjy, R., Jalili, R., ... Lin, S.-H. (2008). One-step isolation of plasma membrane proteins using magnetic beads with immobilized concanavalin A. *Protein Expression and Purification*, 62(2), 223–229.

Legoff, L., Rouault, H., and Lecuit, T. (2013). A global pattern of mechanical stress polarizes cell divisions and cell shape in the growing *Drosophila* wing disc. *Development* 140, 4051–4059.

Li, D., Shao, L., Chen, B.C., Zhang, X., Zhang, M., Moses, B., Milkie, D.E., Beach, J.R., Hammer, J.A., Pasham, M., et al. (2015). Extended-resolution structured illumination imaging of endocytic and cytoskeletal dynamics. *Science* (80-. ). 349.

Lieber, A.D., Schweitzer, Y., Kozlov, M.M., and Keren, K. (2015). Front-to-rear membrane tension gradient in rapidly moving cells. *Biophys. J.* 108, 1599–1603.



- Ma, X., Lynch, H.E., Scully, P.C., and Hutson, M.S. (2009). Probing embryonic tissue mechanics with laser hole drilling. *Phys. Biol.* 6.
- Masters, T.A., Pontes, B., Viasnoff, V., Li, Y., and Gauthier, N.C. (2013). Plasma membrane tension orchestrates membrane trafficking, cytoskeletal remodeling, and biochemical signaling during phagocytosis. *Proc. Natl. Acad. Sci.* 110, 11875–11880.
- Merrifield, C.J., Feldman, M.E., Wan, L., and Almers, W. (2002). Imaging actin and dynamin recruitment during invagination of single clathrin-coated pits. *Nat. Cell Biol.* 4, 691–698.
- Mettlen, M., Stoeber, M., Loerke, D., Antonescu, C. N., Danuser, G., and Schmid, S. L. (2009). Endocytic Accessory Proteins Are Functionally Distinguished by Their Differential Effects on the Maturation of Clathrin-coated Pits. *Molecular Biology of the Cell*, 20(14), 3251-3260.
- Mettlen, M., Loerke, D., Yazar, D., Danuser, G., and Schmid, S.L. (2010). Cargo- and adaptor-specific mechanisms regulate clathrin-mediated endocytosis. *J. Cell Biol.* 188, 919–933.
- Mettlen, M., and Danuser, G. (2014). Imaging and Modeling the Dynamics of Clathrin-Mediated Endocytosis. *Cold Spring Harb. Perspect. Biol.* 6, a017038–a017038.
- Meyerholz, A., Hinrichsen, L., Groos, S., Brandes, G., and Ungewickell, E. J. (2005). Effect of Clathrin Assembly Lymphoid Myeloid Leukemia Protein Depletion on Clathrin Coat Formation. *Traffic* 6 (12), 1225-1234
- Miller, S.E., Mathiasen, S., Bright, N.A., Pierre, F., Kelly, B.T., Kladt, N., Schauss, A., Merrifield, C.J., Stamou, D., Höning, S., et al. (2015). CALM Regulates Clathrin-Coated Vesicle Size and Maturation by Directly Sensing and Driving Membrane Curvature. *Dev. Cell* 33, 163–175.
- Mooney, A.M. (2012). The Influence of DNA Sequence and Post Translational Modifications on Nucleosome Positioning and Stability (Unpublished doctoral dissertation). Ohio State University, Columbus, Ohio
- Neuman, K. C., and Block, S. M. (2004). Optical trapping. *Review of Scientific Instruments*, 75(9), 2787-2809.

- Nowak, S. A. and Chou, T. (2010). Models of dynamic extraction of lipid tethers from cell membranes. *Phys. Biol.* 7 026002
- Pasakarnis, L., Frei, E., Caussinus, E., Affolter, M., and Brunner, D. (2016). Amnioserosa cell constriction but not epidermal actin cable tension autonomously drives dorsal closure. *Nat. Cell Biol.* 18, 1161–1172.
- Phillips, R., Kondev, J., Theriot, J., & Garcia, H. G. (2013). *Physical biology of the cell*. New York: Taylor & Francis Group.
- Popova, N. V., Deyev, I. E., and Petrenko, A. G. (2013). Clathrin-Mediated Endocytosis and Adaptor Proteins. *Acta Naturae*, 5(3), 62–73.
- Pouille, P.A., Ahmadi, P., Brunet, A.C., and Farge, E. (2009). Mechanical signals trigger myosin II redistribution and mesoderm invagination in drosophila embryos. *Sci. Signal.* 2, 1–9.
- Raucher, D., and Sheetz, M.P. (1999). Membrane expansion increases endocytosis rate during mitosis. *J. Cell Biol.*
- Raucher, D., and Sheetz, M. P. (2000). Cell Spreading and Lamellipodial Extension Rate Is Regulated by Membrane Tension. *The Journal of Cell Biology*, 148(1), 127-136.
- Rauskolb, C., Sun, S., Sun, G., Pan, Y., and Irvine, K.D. (2014). Cytoskeletal tension inhibits Hippo signaling through an Ajuba-Warts complex. *Cell* 158, 143–156.
- Robertson, C., and George, S. C. (2012). Theory and practical recommendations for autocorrelation-based image correlation spectroscopy. *Journal of Biomedical Optics*, 17(8), 080801.
- Rodal, S. K., Skretting, G., Garred, Ø, Vilhardt, F., Deurs, B. V., and Sandvig, K. (1999). Extraction of Cholesterol with Methyl- $\beta$ -Cyclodextrin Perturbs Formation of Clathrin-coated Endocytic Vesicles. *Molecular Biology of the Cell*, 10(4), 961-974.
- Saffarian, S., and Kirchhausen, T. (2008). Differential evanescence nanometry: Live-cell fluorescence measurements with 10-nm axial resolution on the plasma membrane. *Biophys. J.* 94, 2333–2342.
- Saffarian, S., Cocucci, E., and Kirchhausen, T. (2009). Distinct dynamics of endocytic clathrin-coated pits and coated plaques. *PLoS Biol.* 7.

Saias, L., Swoger, J., D'Angelo, A., Hayes, P., Colombelli, J., Sharpe, J., Salbreux, G., and Solon, J. (2015). Decrease in Cell Volume Generates Contractile Forces Driving Dorsal Closure. *Dev. Cell* 33, 611–621.

Saleem, M., Morlot, S., Hohendahl, A., Manzi, J., Lenz, M., and Roux, A. (2015). A balance between membrane elasticity and polymerization energy sets the shape of spherical clathrin coats. *Nat. Commun.* 6, 6249.

Scott, B. L., Sochacki, K. A., Low-Nam, S. T., Bailey, E. M., Luu, Q., Hor A., Dickey, A. M., Smith, S., Kerkvliet, J. G. , Taraska, J. W., and Hoppe, A. D. (2018). Membrane bending occurs at all stages of clathrin-coat assembly and defines endocytic dynamics. *Nature Communications* 9, 419

Sheetz, M.P. (2001). Cell control by membrane – cytoskeleton adhesion. *Nature* 2, 366–369.

Shi, Z., Graber, Z. T., Baumgart, T., Stone, H. A., & Cohen, A. E. (2018). Cell membranes resist flow. *Cell*. doi:10.1101/290643

Simon, M. (2012). Chromatin Modified! Dynamics, Mechanics, Structure, and HIV Integration (Unpublished doctoral dissertation). Ohio State University, Columbus, Ohio

Simon, M., North, J. A., Shimko, J. C., Forties, R. A., Ferdinand, M. B., Manohar, M., . . . Poirier, M. G. (2011). Histone fold modifications control nucleosome unwrapping and disassembly. *Proceedings of the National Academy of Sciences*, 108(31), 12711-12716.

Snijder, B., Sacher, R., Rämö, P., Damm, E.M., Liberali, P., and Pelkmans, L. (2009). Population context determines cell-to-cell variability in endocytosis and virus infection. *Nature* 461, 520–523.

Sochacki, K.A., Dickey, A.M., Strub, M.P., and Taraska, J.W. (2017). Endocytic proteins are partitioned at the edge of the clathrin lattice in mammalian cells. *Nat. Cell Biol.* 19, 352–361.

Solon, J., Kaya-Çopur, A., Colombelli, J., and Brunner, D. (2009). Pulsed Forces Timed by a Ratchet-like Mechanism Drive Directed Tissue Movement during Dorsal Closure. *Cell* 137, 1331–1342.

- Stuart, L. and Ezekowitz R. A. (2008). Phagocytosis and comparative innate immunity: learning on the fly. *Nature Reviews Immunology* 8, 131–141
- Subtil, A., Gaidarov, I., Kobylarz, K., Lampson, M.A., Keen, J.H., and McGraw, T.E. (1999). Acute cholesterol depletion inhibits clathrin-coated pit budding. *Proc. Natl. Acad. Sci.* 96, 6775–6780.
- Sukharev, S. (1999). Mechanosensitive channels in bacteria as membrane tension reporters. *The FASEB Journal*, 13(9001).
- Sun, M., Northup, N., Marga, F., Huber, T., Byfield, F.J., Levitan, I., and Forgacs, G. (2007). The effect of cellular cholesterol on membrane-cytoskeleton adhesion. *J. Cell Sci.* 120, 2223–2231.
- Suzuki, M., Tanaka, H., Tanimura, A., Tanabe, K., Oe, N., Rai, S., . . . Watanabe, T. (2012). The Clathrin Assembly Protein PICALM Is Required for Erythroid Maturation and Transferrin Internalization in Mice. *PLoS ONE*, 7(2).  
doi:10.1371/journal.pone.0031854
- Tan, X., Heureaux, J., and Liu, A.P. (2015). Cell spreading area regulates clathrin-coated pit dynamics on micropatterned substrate. *Integr. Biol.* 7, 1033–1043.
- Taylor, M.J., Perrais, D., and Merrifield, C.J. (2011). A high precision survey of the molecular dynamics of mammalian clathrin-mediated endocytosis. *PLoS Biol.* 9.
- Tebar, F., Bohlander, S. K., and Sorkin, A. (1999). Clathrin Assembly Lymphoid Myeloid Leukemia (CALM) Protein: Localization in Endocytic-coated Pits, Interactions with Clathrin, and the Impact of Overexpression on Clathrin-mediated Traffic. *Molecular Biology of the Cell*, 10(8), 2687–2702.
- Treusch S, Hamamichi S, Goodman JL, Matlack KE, Chung CY, . . . , Lindquist S. (2011). Functional links between A $\beta$  toxicity, endocytic trafficking, and Alzheimer's disease risk factors in yeast. *Science*, 334(6060), 1241-1245.
- Tsujita, K., Takenawa, T., and Itoh, T. (2015). Feedback regulation between plasma membrane tension and membrane-bending proteins organizes cell polarity during leading edge formation. *Nat. Cell Biol.* 17, 749–758.
- Tucker, P.K.P., Evans, I.I.R., and Wood, W. (2011). Ena drives invasive macrophage migration in *Drosophila* embryos. *Dis. Model. Mech.* 4, 126–134.

Wang, Y., Liu, Y., Deberg, H. A., Nomura, T., Hoffman, M. T., Rohde, P. R., . . . Selvin, P. R. (2014). Single molecule FRET reveals pore size and opening mechanism of a mechano-sensitive ion channel. *ELife*, 3.

Willy, N.M., Ferguson, J.P., Huber, S.D., Heidotting, S.P., Aygün, E., Wurm, S.A., Johnston-Halperin, E., Poirier, M.G., and Kural, C. (2017). Membrane mechanics govern spatiotemporal heterogeneity of endocytic clathrin coat dynamics. *Mol. Biol. Cell* 28, 3480–34

Wu, X., Zhao, X., Puertollano, R., Bonifacino, J. S., Eisenberg, E., and Greene, L. E. (2003). Adaptor and Clathrin Exchange at the Plasma Membrane and trans-Golgi Network. *Molecular Biology of the Cell*, 14(2), 516–528.

Zidovetzki, R., and Levitan, I. (2007). Use of cyclodextrins to manipulate plasma membrane cholesterol content: Evidence, misconceptions and control strategies. *Biochimica Et Biophysica Acta (BBA) - Biomembranes*, 1768(6), 1311-1324